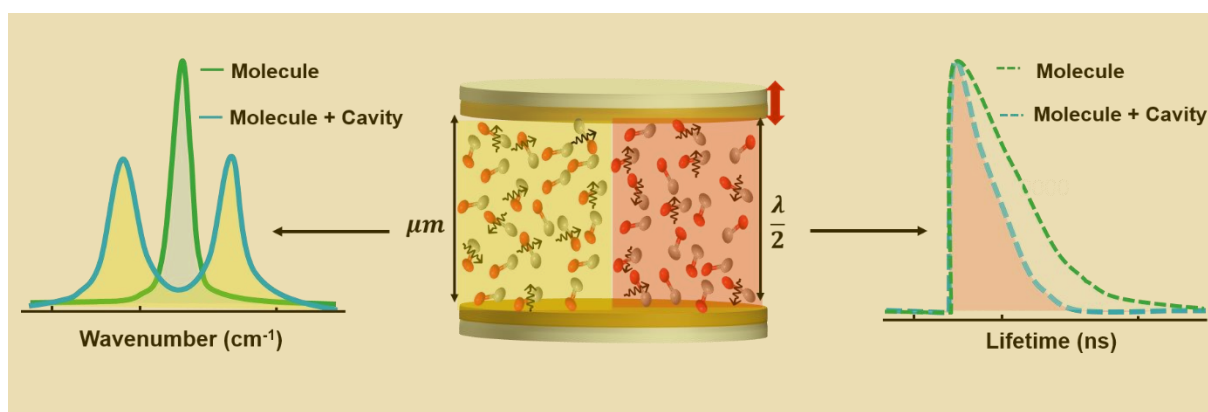




Molecular Properties in an Optical Microcavity: From Ensembles to Single Molecules



Doctoral Thesis

by

Wassie Mersha Takele

Supervisors: Prof. Jacek Waluk and Prof. Alfred J. Meixner

January 2021



EBERHARD KARLS
UNIVERSITÄT
TÜBINGEN



Molecular Properties in an Optical Microcavity: From Ensembles to Single Molecules

Author: Wassie Mersha Takele

Supervisors: Prof. Dr. hab. Jacek Waluk (Institute of Physical Chemistry of the Polish Academy of Sciences, Warsaw, Poland) and Prof. Alfred J. Meixner (Institute of Physical and Theoretical Chemistry, University of Tuebingen, Germany)

This thesis was prepared within the International Doctoral Studies of the Institute of Physical Chemistry of the Polish Academy of Sciences in Warsaw, Kasprzaka 44/52, 01-224 Warsaw in collaboration with the Institute of Physical and Theoretical Chemistry, University of Tuebingen, Auf der Morgenstelle 18, 72076 Tuebingen, Germany.

Warsaw, January 2021

Acknowledgments

First of all, I would like to express my sincere gratitude to my supervisors Prof. Jacek Waluk and Prof. Alfred J. Meixner, for their invaluable guidance, feedback, support throughout my research and for allowing me to work in their world-class laboratories. It was a privilege to work under the supervision of you both and to share your scientific knowledge and experiences accumulated over many decades. The discussions we had about experimental progress and the comments you gave me during writing the scientific papers and the thesis have helped immensely to finish this work as planned. Thank you so much for everything!

I also have special gratitude to Dr. Łukasz Piątkowski (now at Poznań University of Technology) and Dr. Frank Wackenhut (University of Tuebingen) for their tremendous technical support and guidance throughout this work. The continuous guidance from both of you during the experimental works and writing were also significant determinants to finish this work as scheduled. It was a great honour to work and gain a lot of experiences from both of you. I would also like to acknowledge Dr. Frank Wackenhut for performing the theoretical calculations.

I would like to thank Dr. Sylwester Gawinkowski, Dr. Thomas Custer, and Dr. Agnieszka Jamrozik from the Institute of Physical Chemistry of the Polish Academy of Sciences for their support and discussions during experimental works. My gratitude extends to Quan Liu, Achim Junginger, and Saeed Nosrati from the Institute of Physical and Theoretical Chemistry (University of Tuebingen) for sharing their experiences on single-molecule optics and an electron-beam evaporation technique with me.

I would also like to express my acknowledgment to all the staff at the NaMeS project office (the Institute of Physical Chemistry of the Polish Academy of Sciences) and the University of Tuebingen Welcome Center for facilitating administration issues.

Finally, I would like to appreciate and thank my wife, Tizibt Amide, for her patience, love, and encouragement during my study. I also thank my little daughter Blen for the happiness she brings into our daily life. My gratitude to all my families for their support throughout my studies.

This research is part of a project that has received funding from the European Union's Horizon 2020 research and innovation programme under the Marie Skłodowska-Curie grant agreement No. 711859.

Scientific work funded from the financial resources for science in the years 2017-2022 awarded by the Polish Ministry of Science and Higher Education for the implementation of an international co-financed project.



Abstract

The resonance interaction between a confined optical mode within a microcavity and a molecular transition result in either enhancement of spontaneous emission rate in the weak coupling light-matter regime (the so-called Purcell effect) or alteration of energy levels of molecules through the formation of polaritonic states in the strong coupling regime. Due to these effects, light-matter interaction phenomena inside a microcavity can be used as a “physical” method to control the physical and chemical properties of molecules. Thus, this work aims to tailor the spectral, photophysical, and tautomeric properties of molecules by the confined optical fields of the microcavity.

A voltage tunable open IR-microcavity was prepared and characterized to study the influence of the confined field of the microcavity on the IR-absorption properties of molecules in a liquid phase. This cavity is a versatile tool to hybridize essentially any vibrational transition in the mid-IR regime with a cavity mode. Multimode vibrational strong coupling was demonstrated in methyl salicylate using this cavity. A coupled damped harmonic oscillator model was employed as a theoretical tool to describe the multimode vibrational strong coupling. The theoretical results revealed that absorption of uncoupled molecules and spectrally close off-resonance molecular vibrations, in addition to the resonance vibrations, must be simultaneously considered to describe the behaviour of the multimode vibrational strong coupling adequately. The same cavity was used to investigate the effect of vibrational strong coupling on the Raman scattering properties of selected systems. It has been found that vibrational polaritonic states are insensitive to Raman detection. Further investigations employing various configurations of polymer spaced microcavities confirmed that the previously reported Raman study contains artefacts from surface-enhanced Raman scattering.

The photophysical properties of individual phthalocyanine molecules embedded in PVA film were studied under the Purcell effect, using $\lambda/2$ -microcavity, confocal laser scanning microscopy, and a time-resolved fluorescence technique. The photophysical studies show that the occurrence of blinking and photobleaching of individual molecules inside a resonant cavity becomes less probable than for molecules embedded in PVA in free space. The change in transition dipole moment orientation due to tautomerization in single phthalocyanine molecules embedded in PVA in free space and inside a $\lambda/2$ -microcavity were probed employing confocal microscopy coupled with higher-order laser beams. The rate of tautomerization was slowed down in the case of the cavity samples. The reason for the modifications in photophysical and photoinduced tautomerization properties of single molecules inside a resonant cavity is

identified as the reduction of the transfer of molecules into the triplet state due to the Purcell effect. Interestingly, these findings show that the weak light-matter coupling phenomenon can be used to steer photophysical and photochemical processes that occur in the triplet states to the desired direction.

Abstrakt

Oddziaływanie rezonansowe pomiędzy modem optycznym w mikrownęce prowadzić może do zwiększenia stałej szybkości emisji w reżimie słabego sprzężenia (tzw. efekt Purcella) bądź też – w reżimie silnego sprzężenia - do przesunięcia poziomów energetycznych poprzez tworzenie polarytonów. Dzięki tym efektom, oddziaływanie światło-materia wewnątrz mikrownęki może być zastosowane jako „fizyczna” metoda kontroli fizycznych i chemicznych właściwości cząsteczek. Niniejsza praca ma na celu modyfikację spektralnych, fotofizycznych i tautomerycznych parametrów cząsteczek przez pola optyczne mikrownęki.

Zbudowano i scharakteryzowano otwartą, sterowaną napięciem mikrownękę działającą w podczerwieni, w celu zbadania wpływu pola wnęki na właściwości absorpcyjne cząsteczek w roztworze. Wnęka stanowi uniwersalne narzędzie pozwalające na dostrojenie się do dowolnego przejścia oscylacyjnego w obszarze średniej podczerwieni. Pokazano silne sprzężenie angażujące kilka oscylacji w cząsteczce salicylanu metylu. Do teoretycznego opisu tego zjawiska użyto modelu sprzężonych tłumionych drgań harmonicznym. Wykazano, że poprawna symulacja widm wymaga, oprócz uwzględnienia drgania będącego w rezonansie, także przejść bliskoleżących oraz absorpcji pochodzącej od niesprzężonych cząsteczek. Następnie użyto tej samej mikrownęki do badania wpływu silnego sprzężenia na widma ramanowskie wybranych układów. Nie wykryto wpływu tworzenia oscylacyjnych polarytonów na widmo Ramana. Dalsze badania, z użyciem rozmaitych konfiguracji wnęki polimerowej wykazały, że opisany wcześniej literaturze efekt był spowodowany przez powierzchniowe wzmocnienie widma Ramana (SERS).

Zbadano fotofizykę pojedynczych cząsteczek ftalocyjaniny w warstwie alkoholu poliwinylowego (PVA) w $\lambda/2$ -mikrownęce w reżimie efektu Purcella. Zastosowano w tym celu konfokalną mikroskopię fluorescencyjną oraz techniki czasowo-rozdzielcze. Badania fotofizyczne wykazały spadek częstości migotania i fotowybielania pojedynczych cząsteczek we wnęcie w porównaniu z cząsteczkami w PVA umieszczonymi poza wnęką. Następnie, używając modów laserowych wyższego rzędu, dla obu tych konfiguracji przebadano zmiany orientacji momentu przejścia w pojedynczych cząsteczkach, będące konsekwencją tautomeryzacji. Zaobserwowano spowolnienie tautomeryzacji dla cząsteczek we wnęcie. Wytlumaczono powyższe efekty zmniejszeniem prawdopodobieństwa przejścia do stanu trypletowego w konsekwencji efektu Purcella. Istotne jest, że uzyskane wyniki pokazują możliwość wykorzystania słabego sprzężenia do kontroli wydajności fotofizycznych i fotochemicznych procesów zachodzących w stanie trypletowym.

List of Publications

1. **Wassie Mersha Takele**, Frank Wackenhut, Lukasz Piatkowski, Alfred J. Meixner, and Jacek Waluk; Multimode Vibrational Strong Coupling of Methyl Salicylate to a Fabry–Pérot Microcavity, *J. Phys. Chem. B* **2020**, *124*, 5709–5716.
2. **Wassie Mersha Takele**, Frank Wackenhut, Quan Liu, Lukasz Piatkowski, Jacek Waluk, and Alfred J. Meixner; Tailoring Tautomerization of Single Phthalocyanine Molecules Through Modification of Chromophore Photophysics by the Purcell Effect of an Optical Microcavity, (December 2020), Submitted.
3. **Wassie Mersha Takele**, Lukasz Piatkowski, Frank Wackenhut, Sylwester Gawinkowski, Alfred J. Meixner, and Jacek Waluk; Scouting for Strong Light-Matter Coupling Signatures in Raman Spectra (December 2020), Ready for Submission.

Posters and Oral Presentation

Oral Presentation:

1. **Wassie Mersha Takele**, Frank Wackenhut, Lukasz Piatkowski, Alfred J. Meixner, and Jacek Waluk; Controlling the Optical Properties of Molecules by the Vacuum Electromagnetic Fields of a Microcavity (Contributed Talk), *Single-Molecule Sensors and NanoSystems International Conference – S3IC 2020*, November 09-11, 2020.

Poster Presentations:

1. **Wassie Mersha Takele**, Lukasz Piatkowski, and Jacek Waluk; Controlling the optical properties of methyl salicylate by strong light-matter coupling, *Polish Photoscience Seminar 2018*, Krutyń, June 11-14, 2018.
2. Lukasz Piatkowski, **Wassie Mersha Takele**, and Jacek Waluk; Optical Properties of Methyl Salicylate in the regime of the Strong Light-Matter Coupling, *Strong Coupling with Organic Molecules SCOM 2018*, Eindhoven, April 16-18, 2018.
3. **Wassie Mersha Takele**, Lukasz Piatkowski, and Jacek Waluk; Optical properties of Porphycenes in the Regime of Strong Light-Matter Coupling, *Nanophotonics and Micro/Nano Optics International Conference*, Barcelona, March 13-15, 2017.

Table of Contents

Acknowledgments	i
Abstract	iii
Abstrakt	v
List of Publications	vi
Posters and Oral Presentation	vii
1. Introduction	1
1.1. Background and Motivation.....	1
1.2. Thesis Outline	7
2. Theoretical Foundation	8
2.1. The Nature of Electromagnetic Radiation and its Interaction with Molecules	8
2.1.1. The Nature of Electromagnetic Radiation	8
2.1.2. Energy Levels of Molecules	9
2.1.3. The Basic Ideas of Molecular Spectroscopy.....	10
2.2. Molecular Vibrations.....	11
2.2.1. Vibrational Energy Levels and IR Absorption of Molecules	12
2.2.2. Raman Scattering	16
2.3. Molecular Electronic Transitions	18
2.3.1. The Franck-Condon principle	18
2.3.2. The Fates of the Excited States.....	19
2.4. Weak Light-Matter Coupling	21
2.4.1. Fermi's Golden Rule.....	21
2.4.2. The Purcell Effect	22
2.5. Theory of Strong Light-Matter Coupling.....	24
2.5.1. Classical Description of Strong Light-Matter Coupling	24
2.5.2. Quantum Description of Strong Coupling	26
3. Materials and Methods	31
3.1. Chemicals and Materials	31
3.2. Sample Preparations	31
3.2.1. Optical Microcavity Mirrors Preparation.....	31
3.2.2. Spin Coating.....	33
3.3. Optical Setups and Measurements	34
3.3.1. FTIR Spectrometer.....	34
3.3.2. Raman Scattering Measurements.....	35
3.3.3. Single-Molecule Imaging and Time Trace Measurements	36

3.3.4.	Photon Antibunching Measurements	38
3.3.5.	Fluorescence Decay Measurements	39
3.3.6.	Imaging Single-Molecule Tautomerization Reactions	39
4.	Multimode Vibrational Strong Coupling Using a Tunable Microcavity.....	41
4.1.	Introduction	41
4.2.	Open Microcavity Design and Characterization	42
4.3.	Vibrational Strong Coupling in Methyl Salicylate.....	44
4.4.	Theoretical Description of Multimode VSC	48
4.5.	Conclusions	53
5.	Raman Scattering Under Vibrational Strong Coupling	54
5.1.	Introduction	54
5.2.	Microcavity Preparations	55
5.3.	Raman Scattering Properties of Liquid Phase Samples Under Vibrational Strong Coupling	57
5.4.	Raman Scattering Characteristics of a Polymer Film Under Vibrational Strong Coupling	58
5.5.	Conclusions	63
6.	Controlling the Photophysical Properties of Single Molecules by the Purcell Effect of an Optical Microcavity.....	64
6.1.	Introduction	64
6.2.	$\lambda/2$ -Microcavity Preparation and Characterization	66
6.3.	Single-Molecule Detection in the Free Space and Inside a $\lambda/2$ -Microcavity.....	68
6.4.	Photophysical Properties Under the Purcell Effect	69
6.5.	Conclusions	73
7.	Tailoring the Tautomerization Properties of Single Phthalocyanine Molecules by the Vacuum Electromagnetic Field of an Optical Microcavity	74
7.1.	Introduction	74
7.2.	Methods of Probing and Controlling NH Tautomerization	75
7.3.	Modulating Tautomerization by the Purcell Effect.....	78
7.4.	Conclusions	82
8.	Summary and Outlook.....	84
	References.....	88

1. Introduction

1.1. Background and Motivation

At the beginning of the last century, one of the central concepts of quantum mechanics, i.e., the statement that electromagnetic radiation can only be absorbed or emitted in quantized amounts has been formulated,¹ and commercial spectrometers began to be widely available.² Since then, enormous theoretical and practical advances have occurred in the study of molecules through their interaction with photons.³ Indeed, much of what we know about the structure and dynamics of molecules comes from this interaction. The main optical effects that arise due to light-matter interaction are absorption, emission, and scattering of photons. Spectroscopic techniques based on these optical processes have been widely employed to characterize materials and detect an analyte of interest. Nowadays, photons are not only used to probe molecular properties, but also they can be employed to modify the optical and chemical properties of molecules.⁴ Especially, advances in laser technology⁵ and microcavity photonics⁶⁻⁹ have dramatically revolutionized our ability to probe and manipulate molecular phenomena with quantum light.

Lasers have many striking characteristics, such as monochromatic and coherent nature, collimated beams, and an ability to produce pulses. Each of these features (sometimes in combination with the others) opens up novel opportunities to study and manipulate molecular properties with photons.⁵ For instance, the stable and coherent nature of lasers has opened the door for the development of high-resolution spectroscopy,¹⁰ whereas the ability to produce laser pulses of very short duration is useful in the investigation of photophysical phenomena and chemical dynamics on extremely short time scales (attoseconds to nanoseconds).¹¹ The combination of lasers with highly sensitive detectors and microscopy tools allows us to visualize and study individual molecules at a time.¹²⁻¹⁴ The coherent nature of lasers has been widely used for optical control over molecular dynamics by steering a quantum system from an initial state to the desired target state by an external field.^{15,16} On the other hand, the resonance interaction between a microcavity mode and a molecular transition – the topic of this thesis – focuses on harnessing the vacuum electromagnetic fields of a microcavity to modify molecular properties.

Fabry–Pérot type optical microcavities confine and store light to small volumes by bouncing light back and forth between two parallel mirrors (Figure 1.1a). They are widely used to control the properties of quantum emitters placed inside them.¹⁷ Microcavities have also been used in optical sensing and quantum information technologies.¹⁸ The prominent optical

effects in microcavity photonics are reflection and interference. Generally, optical microcavities confine light in-between two mirrors either by single or multiple interface reflections. The former can be achieved from the reflection of metallic mirrors, whereas the latter can be realized using a distributed Bragg reflector (DBR) mirrors consisting of periodically stacked layers of dielectric material.¹⁹ The choice of a microcavity for a particular experiment depends on several requirements, such as ease of fabrication, less optical losses, minimum mode volume, and tunability.²⁰ A structure that fulfils most of these factors is a Fabry–Pérot microcavity that consists of two metallic mirrors of thickness M_1 and M_2 separated by an optical pathlength L_{op} (Figure 1.1a). The mirrors are aligned parallel to each other so that light is reflected multiple times between the mirrors, and the optical pathlength determines the cavity modes, which can be formed as a standing wave inside the cavity (Figure 1.1b). The resulting cavity modes are equally spaced in frequency; the separation between successive cavity modes is termed the free spectral range of the cavity. The cavity modes have a maximum transmission for wavelengths satisfying the condition:^{21,22}

$$L_{op} = m \left(\frac{\lambda}{2n} \right), \quad (1.1)$$

where L_{op} , m , λ , and n are the optical path length of the cavity, an integer, the wavelength of light, and the refractive index of the medium within the cavity, respectively.

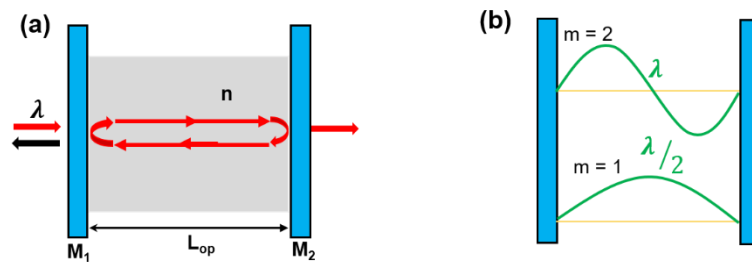


Figure 1.1. (a) Schematic illustration of a Fabry–Pérot microcavity of optical path length L_{op} having two parallel mirrors M_1 and M_2 ; λ is the wavelength of light introduced into the cavity, and n is the refractive index of the material. (b) First ($m = 1$), and second ($m = 2$) longitudinal mode of a Fabry–Pérot microcavity.

An important parameter used to specify the cavity mode is the quality factor (Q-factor), which is given by:

$$Q = \frac{\omega_c}{\Delta\omega}, \quad (1.2)$$

where ω_c and $\Delta\omega$ are the resonance frequency and the linewidth of the cavity mode, respectively. The Q-factor indicates the stored energy/energy loss per cycle, and it characterizes the energy loss from the cavity due to absorption, scattering, or leakage through the imperfect mirrors.²³ The reflectivity of the mirrors mainly governs the Q-factor of the cavity, and a large Q-factor means low-loss microcavity. The typical Q-factor obtained from Fabry–Pérot type microcavities made from metallic mirrors is from $\sim 10 - 100$, depending on the mirrors thickness and their surface roughness. As the molecular transitions in organic molecules have relatively high rate of energy dissipation (broader spectral peaks), the small Q-factor due to the inherent reflectivity of metallic mirrors does not impose a limitation in studying the optical properties of organic molecules using Fabry–Pérot type microcavities.²⁴

The photon decay rate of the cavity (κ) is given by

$$\kappa = \frac{\omega_c}{Q}. \quad (1.3)$$

Thus, the higher the Q-factor, the longer time the photon is stored in a microcavity, which gives sufficient time for light-matter coupling inside a microcavity. The effective mode volume (V) describes the ability of the cavity to confine photons spatially. It is related to the vacuum electric field of the cavity (ε_{vac}) by:²¹

$$\varepsilon_{vac} = \sqrt{\frac{\hbar\omega_c}{2\varepsilon_0 V}}, \quad (1.4)$$

where ω_c is the cavity mode frequency and ε_0 the permittivity of the free space. The smaller the mode volume, the better the field confinement.

When the resonant mode of an optical microcavity coincides with the quantized transition frequency of a molecule, there will be energy exchange between the cavity mode and the molecular transition. The transition frequency of a molecule is governed by its internal structure, and it is natural to take it as fixed. Hence, the resonance condition is attained by tuning the cavity mode towards the molecular transition frequency. At resonance, the energy

exchange between molecules and a cavity mode is determined by three parameters: the rate of photons escaping from the cavity or the damping of the cavity (κ), the dephasing rate of the emitter (γ), and the coupling strength (g).²¹

If the damping rates of the cavity and the molecule are larger than the coupling strength, i.e., $(\kappa, \gamma) \gg g$, the interaction is said to be in the weak coupling regime. In this regime, the energy levels of the molecules are not significantly altered, and only the spontaneous emission rate is modified (Figure 1.2a). Altering a radiative decay rate by weak light-matter coupling was first demonstrated by Purcell (at radio frequency) in 1946.²⁵ By the end of the 1960s, Drexhage demonstrated that the fluorescence decay time of optically excited molecules could be tailored when they were placed in front of a mirror.²⁶ Since then, enhancing the radiative decay rate by placing quantum emitters near metallic surfaces, in microcavities or photonic crystals, generally known as the Purcell effect, has been widely employed for various applications. Among others, the Purcell effect has been used to improve the performance of light-emitting devices,^{27,28} control the photophysical properties of single emitters,²⁹ and influence Förster energy transfer.³⁰

On the other hand, if the rate of energy exchange between the cavity mode and the molecular transitions dominates the decay rates, i.e., when $g \gg (\kappa, \gamma)$, the system enters the strong coupling (SC) regime. In this case, molecules and the cavity can be considered as a single quantum object with energy shared coherently and reversibly between them. SC leads to the formation of new spectroscopically accessible half-light, half-matter quasiparticles termed polaritons.³¹ The separation between the upper and lower polaritonic states is known as Rabi splitting energy ($\hbar\Omega_R$). SC phenomenon was first observed in a microwave cavity containing a single Rydberg atom in 1987³² and later, after five years, in semiconductor quantum wells.³³ These experiments were realized at low temperature and using very high Q-factor DBR cavities due to the low binding energy of inorganic materials (Wannier–Mott excitons). In addition, as most inorganic materials have small oscillator strength, strong coupling in these materials gives very small Rabi splitting energy (of the order of 10 meV).³⁴

Due to the large transition dipole moment and strong binding energy, organic molecules (Frenkel excitons) have been expected to provide a larger coupling strength at room temperature.³⁴ In 1998, Lidzey et al. first reported electronic strong coupling (ESC) – the hybridization of the first excited electronic state with the cavity mode - in organic molecules by coupling the Soret band of Zn porphyrin dye blended with polystyrene film with the cavity mode. A Rabi splitting of 160 meV was observed, and the value of the splitting was varied by

changing the concentration of the dye in the polymer film.³⁵ After a year, Lidzey et al. have demonstrated ESC from J-aggregates. Moreover, they have observed for the first time the signature of cavity-polariton emission from the lower polariton branch.³⁶ Since then, J-aggregates have been widely studied under ESC, as they have large oscillator strength, small Stokes shift, and small linewidth. These experiments were realized by placing dye molecules embedded in a polymer film between the bottom DBR mirror and the top metallic mirror. Recently, Bahsoun et al. reported liquid phase ESC using nanofluidic Fabry–Pérot cavity.³⁷ Strong coupling between a single emitter and a plasmonic structure mode has also been reported.³⁸ Plasmonic cavities are promising for studying properties of few emitters under ESC due to their ability to confine light in subdiffraction-limited volumes with the drawback of huge damping.³⁹ However, achieving strong coupling with a single-molecule is not yet a trivial task, as the coupling becomes more efficient when the number of molecules in the cavity mode increases.

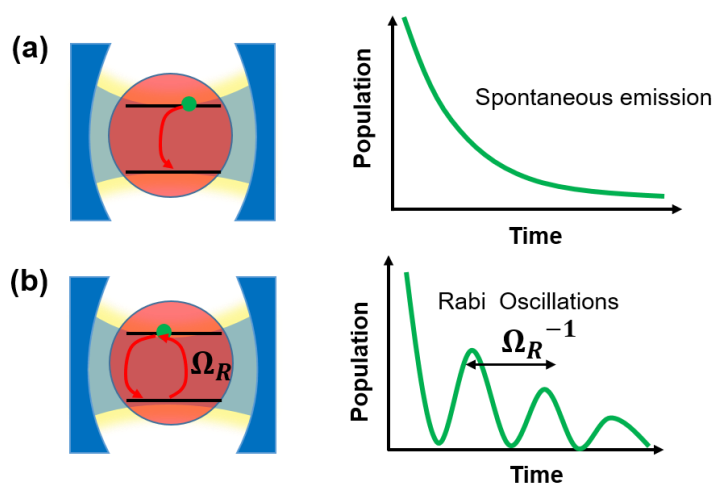


Figure 1.2. Schematic illustration of an optical microcavity effect on a two-level emitter: In the case of weak coupling, the cavity alters the spontaneous emission rate (a). Strong coupling occurs when there is a reversible energy exchange between the cavity mode and the molecular transitions with a Rabi frequency Ω_R (b). The right upper panel shows the excited state population time evolution, whereas the lower right panel shows Rabi oscillations in the case of strong coupling.⁴⁰

In 2015, Shalabney et al.⁴¹ and Long and Simpkins⁴² independently demonstrated vibrational strong coupling by hybridizing the C=O stretching modes of polyvinyl acetate and polymethyl methacrylate films with microcavity modes, respectively. Later in the same year, George et al.⁴³ demonstrated vibrational strong coupling in a liquid phase. Ultrastrong

vibrational coupling – the regime where Rabi splitting becomes about 20% of the molecular frequency - was also observed from pure Fe(CO)₅ liquid.⁴⁴ So far, vibrational strong coupling has been reported from many systems, such as polymer films,^{45,46} different organometallic complexes simultaneously dissolved in solution,⁴⁷ pure solvents,⁴⁸ and liquid crystal molecules.⁴⁹ Pino et al. have developed a quantum mechanical model to describe the hybridization between a cavity mode and an ensemble of molecular vibrations.⁵⁰

Over the years, ensemble strong coupling has obtained significant research attention due to the intriguing properties of polaritonic states. For instance, exciton-polaritons have very light mass (about three orders of magnitude lighter than an electron),⁵¹ they obey bosonic statistics, and they are stable at room temperature. Because of these properties, polaritonic states have been widely studied in condensate physics.⁵² Strong light-matter coupling is also being researched with the aim of improving the performance of organic photovoltaics⁵³ and organic photodiodes.⁵⁴ The ability to tune the energy levels of molecules through the formation of polaritonic states has recently received significant attention in chemical and molecular sciences since it allows to modulate the chemical reactivity, materials properties, and photophysical processes without altering the structure or constitution of molecules.

Electronic strong coupling has been employed to control the rates of photoisomerization reaction,⁵⁵ work function,⁵⁶ conductivity,⁵⁷ and quantum yield of emission.⁵⁸ Another possibility is modifying the energy difference between the excited singlet and excited triplet states. The rate of intersystem crossing in Erythrosine B was increased by a factor of four because of the decreased energy difference between the triplet state and the lower polariton.⁵⁹ Similarly, the effect of vibrational strong coupling on the ground state energy landscape of molecules provides a novel way to control chemical reactions remotely. Hence, in the previous five years, there have been significant experimental^{60,61} and theoretical efforts⁶²⁻⁶⁴ to exploit the possible applications of vibrational strong coupling in chemistry.

This thesis thus addresses the influence of the confined optical fields of an optical microcavity on the spectral, photophysical, and tautomeric properties of molecules. A voltage tunable infrared open microcavity has been designed and used to study the influence of the strong coupling on the vibrational energy levels of molecules in the liquid phase. A classical model based on coupled harmonic oscillators has been used to explain the dynamics of vibrational strong coupling. The influence of strong coupling on Raman scattering properties of liquid samples has also been studied using the IR-open microcavity. The Raman scattering properties of solid-state samples were investigated by preparing various polymer-spaced fixed microcavities. On the other hand, the photophysical and tautomerization properties of single

molecules were studied under weak light-matter coupling conditions. For this purpose, a voltage tunable $\lambda/2$ -microcavity was employed.

1.2. Thesis Outline

The structure of this thesis is as follows: Chapter 2 starts by describing the basics of electromagnetic radiation, molecular energy levels, IR absorption, Raman scattering, and molecular electronic transitions. Then the main theories of weak and strong light-matter coupling are discussed in detail. Chapter 3 aims to explain the techniques used to prepare the microcavity mirrors and the optical instruments employed to collect the experimental data. Chapters 4, 5, 6, and 7 describe the results collected throughout this work. Each chapter contains a brief introduction, methods, results, discussion, and conclusions. Chapter 4 discusses the influence of strong coupling on the spectral and vibrational energy levels of molecules. The effect of strong coupling on the Raman scattering properties of molecules is discussed in Chapter 5. Chapters 6 and 7 describe how the Purcell effect can be used to modulate the photophysical and tautomeric properties of single molecules, respectively. Finally, Chapter 8 gives a summary of the main results and provides a brief outlook.

2. Theoretical Foundation

This chapter describes the basic principles and laws that govern various optical processes covered in this work. Section 2.1 discusses the nature of electromagnetic radiation, the quantum description of molecular energy levels, and the basic concepts of light-matter interaction in ‘free space’. In the whole thesis, the term ‘free space’ is used to describe optical processes that occur without photonics boundary conditions, such as a microcavity. Section 2.2 presents the theories of molecular vibrations and the Raman scattering. Section 2.3 explains the basic principles of molecular electronic transitions and fluorescence lifetime. Finally, in sections 2.4 and 2.5, the theories of weak and strong light-matter coupling phenomena are discussed.

2.1. The Nature of Electromagnetic Radiation and its Interaction with Molecules

2.1.1. The Nature of Electromagnetic Radiation

In the 1860s, James Clerk Maxwell formulated the classical theory of light by unifying optics, electricity, and magnetism. Maxwell predicted the existence of electromagnetic radiation - coupled electric and magnetic fields traveling as waves at a constant speed. In 1888, Hertz showed the existence of long-wavelength electromagnetic waves (radio waves) experimentally and confirmed that their properties are consistent with Maxwell’s theoretical predictions.⁶⁵ Within a few decades, the whole electromagnetic spectrum from gamma radiation to the microwaves was discovered. The electric (\mathbf{E}) and magnetic (\mathbf{B}) fields oscillate in phase perpendicular to each other and perpendicular to the direction of propagation as well. It is the oscillating field that interacts with the charged nuclei and electrons of a molecule and results in energy transfer to the molecule. Assuming an electromagnetic wave traveling along the x -direction with frequency ν , the equations that describe the oscillating electric field, $\mathbf{E}(x,t)$, and magnetic field, $\mathbf{B}(x,t)$ vectors are given by²¹

$$\mathbf{E}(x, t) = \mathbf{E}_0 \cos(2\pi\nu t - kx) \quad (2.1)$$

$$\mathbf{B}(x, t) = \mathbf{B}_0 \cos(2\pi\nu t - kx), \quad (2.2)$$

where \mathbf{E}_0 and \mathbf{B}_0 are the amplitudes of the electric and magnetic fields, respectively, and the parameter k is the wavenumber given by:

$$k = \frac{2\pi}{\lambda}. \quad (2.3)$$

The way we think about electromagnetic radiation radically changed when Max Planck suggested in 1900 that black-body radiation is emitted in discrete energy packets called *quanta*.²¹ Planck believed that once the light energy was emitted, it behaved like a classical wave. However, after five years, Einstein proposed instead that the radiation itself existed as small packets of energy, $E = h\nu$. These packets of energy were later named *photons* by the physical chemist Gilbert N. Lewis.⁶⁶ Nowadays, it has been established that light has a *wave-particle* dual nature. Some processes, such as diffraction and interference, exhibit the wave nature of light, whereas other phenomena, for example, the photoelectric effect, display the particle aspects of light.

2.1.2. Energy Levels of Molecules

The interaction of photons with molecules is primarily determined by the energy levels of the molecule. Molecules only exist in specific quantum states (characterized by quantum numbers), with each quantum state having a discrete amount of energy and angular momentum. Thus, energy levels in molecules are quantized. The Schrödinger equation is a starting point for obtaining information about the allowed quantized energy levels of molecules. Molecules are a collection of positively charged atomic nuclei surrounded by a cloud of negatively charged electrons. The distance between each nucleus and electron is a variable in the Schrödinger equation. Thus, the number of terms in the Schrödinger equation significantly increases as the size of the molecule increases. Hence, we solve the Schrödinger equation of molecules based on the *Born–Oppenheimer* approximation. This approximation assumes that the nuclei (being thousands of times heavier than an electron) remain motionless while electrons move around them; i.e., there is an approximate wavefunction defining the motions of the electrons that is independent of the nuclei wavefunction.⁶⁷ The nuclear motion can be separated into translational, rotational, and vibrational modes. Accordingly, the wavefunction for the molecule as a whole is given as a product of a wavefunction for the electronic motions (ψ_{el}), a wavefunction for the vibrational motions (ψ_{vib}), a wavefunction for the rotational motions (ψ_{rot}), and a wavefunction for the translational motion (ψ_{tr}):⁶⁸

$$\psi_{molecule} = \psi_{el}\psi_{vib}\psi_{rot}\psi_{tr} \quad (2.4)$$

The Hamiltonian for the molecule is written as a sum of each mode:

$$\hat{H}_{molecule} = \hat{H}_{el} + \hat{H}_{vib} + \hat{H}_{rot} + \hat{H}_{tr} \quad (2.5)$$

The Schrödinger's equation for the molecule becomes:

$$\hat{H}_{molecule}\psi_{molecule} = (\hat{H}_{el} + \hat{H}_{vib} + \hat{H}_{rot} + \hat{H}_{tr})\psi_{el}\psi_{vib}\psi_{rot}\psi_{tr} \quad (2.6)$$

$$= \psi_{vib}\psi_{rot}\psi_{tr}\hat{H}_{el}\psi_{el} + \psi_{el}\psi_{rot}\psi_{tr}\hat{H}_{vib}\psi_{vib} + \psi_{el}\psi_{vib}\psi_{tr}\hat{H}_{rot}\psi_{rot} \\ + \psi_{el}\psi_{vib}\psi_{rot}\hat{H}_{tr}\psi_{tr} \quad (2.7)$$

$$= \psi_{vib}\psi_{rot}\psi_{tr}E_{el}\psi_{el} + \psi_{el}\psi_{rot}\psi_{tr}E_{vib}\psi_{vib} + \psi_{el}\psi_{vib}\psi_{tr}E_{rot}\psi_{rot} \\ + \psi_{el}\psi_{vib}\psi_{rot}E_{tr}\psi_{tr} \quad (2.8)$$

$$\hat{H}_{molecule}\psi_{molecule} = (E_{el} + E_{vib} + E_{rot} + E_{tr})\psi_{el}\psi_{vib}\psi_{rot}\psi_{tr}. \quad (2.9)$$

Therefore, the energy possessed by a molecule separates into different contributions:

$$E_{tot} = E_{el} + E_{vib} + E_{rot} + E_{tr}. \quad (2.10)$$

The energy levels of molecules can be probed experimentally by measuring the wavelengths of the light that is emitted, absorbed, or scattered in transitions between energy levels. Translational eigenvalues are very closely spaced and too small to probe spectroscopically. Thus, the spectra of molecules arise only from rotational, vibrational, and electronic transitions. These transitions are not independent of each other, and molecular spectra are more complex than atomic spectra due to their interaction.⁶⁹

2.1.3. The Basic Ideas of Molecular Spectroscopy

The basic idea of molecular spectroscopy is that if a photon is absorbed or emitted by a molecule, the molecule makes a transition between energy levels whose difference in energy is equal to the energy of the photon. Conservation of energy requires that the energy of the photon satisfies:

$$E_{\text{photon}} = h\nu = \frac{hc}{\lambda} = E_{\text{upper}} - E_{\text{lower}}, \quad (2.11)$$

where E_{upper} and E_{lower} are the energy eigenvalues for the upper and lower energy levels of the molecule.

If a photon is absorbed, the molecule jumps from a lower to a higher energy level. If a photon is emitted, the molecule makes a transition from a higher to a lower energy level. The rates of spectroscopic transitions determine the intensity of the spectral response. The most intense transitions are induced by the interaction of the electric dipole of molecules with the electric component of the electromagnetic field. The transition probability between initial state ψ_i and final state ψ_f is proportional to the square of the transition dipole moment (μ_{fi}). Mathematically μ_{fi} is defined as⁷⁰

$$\mu_{fi} = \int \psi_f^* \hat{\mu} \psi_i d\tau, \quad (2.12)$$

where $\hat{\mu}$ is the electric dipole moment operator for the molecule and the subscripts i and f stand for the initial and final state.

$$\hat{\mu} = \sum_i q_i r_i, \quad (2.13)$$

q_i is the charge and the sum is over all the electrons and nuclei of the molecule, and r_i is the position of the i th charged particle. From Eqn. 2.12, we see that if the transition dipole moment vanishes (usually because of symmetry), the spectral line has no intensity. The rules governing the nonvanishing of μ_{fi} are called selection rules, and these allow us to make sense out of observed molecular spectra.⁷⁰

2.2. Molecular Vibrations

Since each atom can move in 3-dimensional space (the x-, y-, and z- directions), a molecule of N atoms has in total $3N$ degrees of freedom. However, the $3N$ displacements contain six degrees of freedom originating from translational motions of the molecule in the three directions and rotational motions of the whole molecule about the three principal axes of rotation. When we subtract the translational and rotational degrees of freedom from the total degrees of freedom of the molecule, the number of normal modes of vibration becomes $3N - 6$. Rotation about the molecular axis does not exist in linear molecules; thus, the number of its

vibrational degrees of freedom is $3N - 5$.⁷¹ Molecular vibration that causes changes in bond distance between two atoms is known as *stretching*, while vibration involving a change in bond angle is called *bending*. In the following, we shall briefly discuss the theoretical principles of the spectroscopic methods that have been used to probe molecular vibrations: IR absorption spectroscopy and Raman scattering.

2.2.1. Vibrational Energy Levels and IR Absorption of Molecules

A harmonic oscillator is a good model to theoretically describe the vibration of a diatomic molecule. Suppose two nuclei having masses m_1 and m_2 are connected by an elastic bond and are separated by a distance r (Figure 2.1).^{72,73} When the two nuclei move away from the equilibrium position, they will experience a restoring force (F). The restoring force constant k is assumed to obey Hook's law:

$$F = -kq, \quad (2.14)$$

where $q = r - r_{eq}$ is the displacement away from the equilibrium position and r_{eq} is the equilibrium bond length. k is the force constant. The potential energy of an ideal harmonic oscillator is given by

$$V = - \int F dq = \frac{1}{2} kq^2. \quad (2.15)$$

Therefore, the quantum mechanical Hamiltonian operator for the system is given by:

$$\hat{H} = \frac{-\hbar^2}{8\pi^2\mu} \nabla^2 + \frac{1}{2} kq^2. \quad (2.16)$$

where the first term in Eqn. 2.16 is a kinetic energy term; μ is the reduced mass equal to:

$$\mu = \frac{m_1 m_2}{(m_1 + m_2)}. \quad (2.17)$$

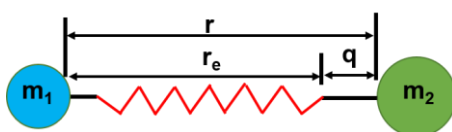


Figure 2.1. Simple harmonic oscillator model with two masses.⁷²

From the quantum mechanical treatment of the harmonic oscillator, we know that the allowed vibrational energies for the molecule is given by⁷²

$$E_{vib} = \left(v + \frac{1}{2}\right)\hbar\omega \quad \omega = \sqrt{\frac{k}{\mu}}, \quad (2.18)$$

where the vibrational quantum number $v = 0, 1, 2, \dots, \infty$.

In the lowest vibrational state ($v = 0$), the molecule still has the *zero-point energy*, $E_0 = \frac{1}{2}\hbar\omega$. It means the atoms can never be at rest relative to each other. For each vibrational quantum number, there is a corresponding energy level and wavefunction. In spectroscopy, it is common to give the energy in wavenumbers. Hence, we divide E_{vib} , Eqn. 2.18, by hc :⁷⁰

$$\tilde{G}(v) = \frac{E_{vib}}{hc} = \tilde{\nu} \left(v + \frac{1}{2}\right), \quad (2.19)$$

where $\tilde{G}(v)$ is referred to as the vibrational term value for the v th vibrational level in cm^{-1} and $\tilde{\nu}$ is the fundamental frequency of vibration. The fundamental vibrational frequency $\tilde{\nu}$ is given by:

$$\tilde{\nu} = \frac{1}{2\pi c} \sqrt{\frac{k}{\mu}}. \quad (2.20)$$

The force constant is the measure of the strength of the chemical bond. Eqn. 2.20 shows that the larger the value of k and the smaller the reduced mass, the higher the molecular vibration frequency.

According to the quantum harmonic approximation, the energy levels are equally spaced (Figure 2.2a). This is a good approximation only for the lowest vibrational states of a diatomic molecule. As molecules are not real harmonic oscillators, the spacing between adjacent energy levels decreases as the vibrational quantum number increases (Figure 2.2b). For a real molecule, when $r \gg r_e$, q gets bigger, and the restoring force eventually levels off, and the molecule dissociates. On the other hand, as q decreases, the nuclei approach together and repel each other. Hence, the potential energy surface is steeper at a small internuclear distance and shallower at a large internuclear distance to reflect the approach of dissociation (Figure 2.2b). An analytical function that has this shape in the region of interest for real molecules is the Morse potential. This potential is purely empirical and has the form⁷²:

$$V(r) = D_e [1 - e^{-\alpha(r-r_e)}]^2, \quad (2.21)$$

where D_e is the *dissociation energy*, which is equal to the energy required to dissociate the molecule from the state of minimum $V(r_e)$. The parameter α determines the curvature of the function and is equal to $k/2D_e$. The values of these parameters must be determined for each molecule. This function has the following characteristic features: $V(r)$ goes to zero at r_e , approaches the dissociation energy D_e at large r and takes on a large value as r goes to zero. The Schrödinger equation can be solved for the Morse potential, and the allowed energy levels are⁷⁴

$$\tilde{G}(v) = \tilde{\nu} \left(v + \frac{1}{2} \right) - \left(v + \frac{1}{2} \right)^2 x_e \tilde{\nu} \quad (2.22)$$

The anharmonicity constant x_e is given by:

$$x_e = \frac{\tilde{\nu}}{4D_e}. \quad (2.23)$$

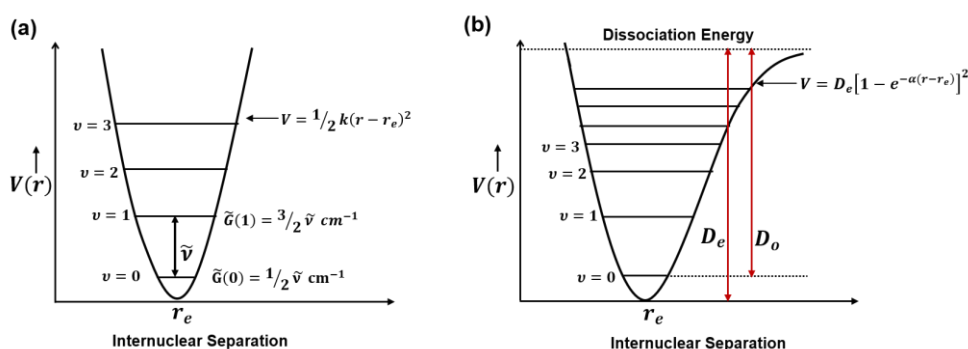


Figure 2.2. (a) Harmonic potential well and energy levels. (b) The Morse potential for a diatomic molecule, where D_0 is the spectroscopic dissociation energy and it can be measured from the zeroth vibrational level.⁷²

The direct absorption or emission of IR radiation can cause changes in vibrational energy levels and can be accompanied by the transition between rotational energy levels of molecules. The fundamental vibrations of molecules are observed in the mid-infrared regime of the spectrum ($4000\text{--}400 \text{ cm}^{-1}$), which has been widely employed to investigate the structure of molecules. For a molecule to absorb infrared radiation, its electric dipole moment must change during vibration. This is known as the gross selection rule. For instance, homonuclear

diatomic molecules are ‘‘IR-inactive’’, as their dipole moment remains zero no matter how long is the bond. The selection rule for changes between vibrational energy levels is⁷⁴

$$\Delta\nu = \pm 1. \quad (2.24)$$

Transitions for which $\Delta\nu = +1$ correspond to absorption and those with $\Delta\nu = -1$ correspond to emission. As most of the molecules predominantly reside in the ground vibrational state, the allowed infrared absorption occurs between the $\nu = 0$ and $\nu = 1$ energy levels. This transition is known as the *fundamental vibration* (Figure 2.3a). The $\nu = 0$ to $\nu = 2$, etc. transitions are called *overtones* (Figure 2.3b and c). They are forbidden, thus having smaller intensity. The $\nu = 1$ to $\nu = 2$ transition is called a *hot band* (Figure 2.3d). It occurs because thermal energy populates $\nu = 1$ to a small extent.⁷⁵ Infrared bands are broadened a couple of hundred cm^{-1} by the thermal population of rotational levels.⁷⁶

Experimentally, IR-active vibrational transitions can be detected by measuring the absorption of IR radiation by the sample as a function of frequency. The Beer-Lambert law governs the intensity of the IR absorption:

$$I = I_0 e^{-\epsilon c l}, \quad (2.25)$$

where I and I_0 are the intensities of the incident and the transmitted beam, respectively. ϵ , c , and l denote the molecular absorption coefficient, the concentration of the sample, and the length of the measurement cell. The absorbance (A) is related to the concentration of the molecule, and it can be used for the quantitative purpose:

$$A = \epsilon c l. \quad (2.26)$$

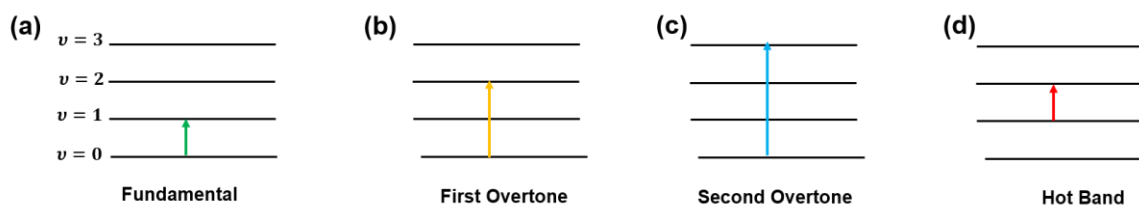


Figure 2.3. Energy levels for fundamental, overtones, and hot band infrared transitions.⁷⁵

2.2.2. Raman Scattering

When a molecule is irradiated with monochromatic light, the incident radiation can be scattered either elastically or inelastically. Mostly, light is elastically scattered; that is, the frequency of the incident photon is equal to that of the scattered photon, and the direction changes. This phenomenon is known as Rayleigh scattering. The effect that gives rise to Raman spectra is the inelastic scattering of photons by molecules, where the scattered photon is at different energy from that of the incident photon. The interaction of radiation with a molecule distorts the electron cloud around the molecule. This distortion leads to polarization of the molecule and gives a short-lived state known as “virtual state”. Thus, the “virtual state” is not a real quantum state of the molecule; instead, it can be considered as a very short-lived state caused by the distortion of the electron cloud through the oscillating electric field of the light.⁷⁷ Raman scattering is an *instantaneous* process that occurs without any electronic transition, whereas fluorescence involves an intermediate step (electronic excitation followed by emission with a finite lifetime).⁷⁸

During the inelastic Raman scattering process, the scattered photon may lose some of its energy to the molecule or gain some from it (Figure 2.4). The energy part of the scattered radiation lying lower than the excitation energy is called the Stokes region, and the higher energy components correspond to the anti-Stokes region. In order for an anti-Stokes process to take place, the molecule must be in an excited vibrational state. This may be caused by thermal excitation, governed by Boltzmann distribution. Hence, the anti-Stokes Raman scattering is weaker than the Stokes Raman scattering. Vibrational and rotational energy levels can be studied by examining the frequencies present in the radiation scattered by molecules in Raman spectroscopy.⁷⁷

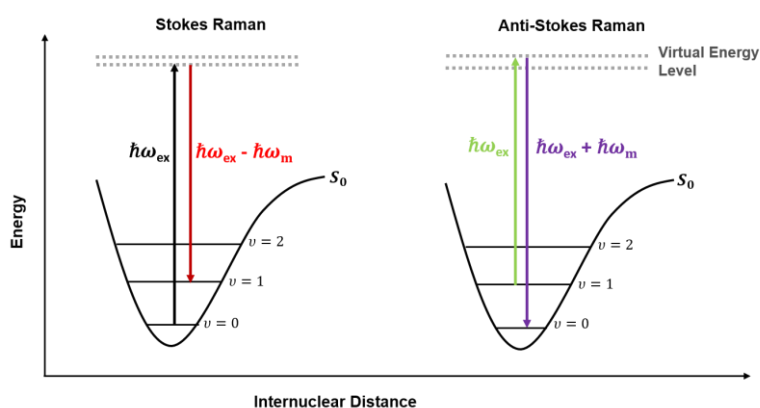


Figure 2.4. Spectroscopic transitions that show Stokes and anti-Stokes Raman processes. In contrast to the Stokes process, the excitation of anti-Stokes scattering begins with the molecule

already in the $\nu = 1$ state of S_0 which relaxes back down to $\nu = 0$, giving a scattered photon with an energy larger than the incoming one.⁷⁷

Classically, the Raman scattering process can be explained by the polarizability of the molecule. The induced dipole moment ($\boldsymbol{\mu}_{\text{ind}}$) formed when a molecule is positioned in an electric field can be expressed as⁷⁰

$$\boldsymbol{\mu}_{\text{ind}} = \alpha \mathbf{E}, \quad (2.27)$$

where α is the polarizability and \mathbf{E} the electric field vector. The polarizability of a molecule that is rotating or vibrating is not constant but varies with some frequency ν_k according to

$$\alpha = \alpha_0 + (\Delta\alpha)\cos(2\pi\nu_k t), \quad (2.28)$$

where α_0 is the equilibrium polarizability, and $\Delta\alpha$ is the maximum variation (the change in polarizability). Consider the electric field that oscillates at a certain point in space according to the equation

$$\mathbf{E} = \mathbf{E}_0 \cos(2\pi\nu t). \quad (2.29)$$

Thus, the $\boldsymbol{\mu}_{\text{ind}}$ is given by

$$\boldsymbol{\mu}_{\text{ind}} = [\alpha_0 + (\Delta\alpha)\cos(2\pi\nu_k t)] \mathbf{E}_0 \cos(2\pi\nu t) \quad (2.30)$$

$$= \alpha_0 \mathbf{E}_0 \cos(2\pi\nu t) + \frac{1}{2}(\Delta\alpha)\mathbf{E}_0 [\cos 2\pi(\nu + \nu_k)t + \cos 2\pi(\nu - \nu_k)t] \quad (2.31)$$

The transformation of Eqn. 2.30 to 2.31 used the following trigonometric identity:

$$\cos a \cos b = \frac{1}{2}[\cos(a + b) + \cos(a - b)]. \quad (2.32)$$

According to Eqn. 2.31, $\boldsymbol{\mu}_{\text{ind}}$ contains three components. The first term shows that the frequency of the induced dipole moment is the same as the frequency of excitation, which is the Rayleigh line. The other two terms, i.e. $(\nu + \nu_k)$ and $(\nu - \nu_k)$ are anti-Stokes and Stokes lines. Moreover, Eqn. 2.31 shows that in order for a molecular vibration to be Raman-active, the polarizability α must change ($\Delta\alpha \neq 0$) during the vibration. The different selection rules

for Raman and infrared spectroscopy imply that both methods give complementary information: Strong infrared absorbing vibrations are often weak Raman scatterers and vice versa.

2.3. Molecular Electronic Transitions

Electronic states of molecules are classified based on their multiplicity. According to the Pauli exclusion principle, two electrons in an atom cannot have the same four quantum numbers (n, l, m_l, m_s), and pairs of electrons that are placed in an orbital must have opposite spins, i.e., if one is spin up, the other must be spin down. Thus, the total spin quantum number ($S = \sum s_i$, with $s_i = +1/2$ or $s_i = -1/2$) is zero, and the total multiplicity ($M = 2S + 1$) is equal to one. Thus, the molecule is said to be in the singlet ground state. When a molecule is excited by a photon, one of the two electrons of opposite spins is transferred to an empty molecular orbital of higher energy. During the excitation process, the spin of the electron is not changed; thus, the molecule is still in the singlet excited electronic state. However, it may happen that an electron's spin will change when it is excited, and the two unpaired electrons now have parallel spins. In this case, the molecule is in the triplet state (T_1). According to Hund's rule, states that have maximum M lie at the lowest energy, thus the lowest triplet state (T_1) is placed below the lowest excited singlet state (S_1), Figure 2.5. The spacing between electronic energy levels matches the photon energies in the visible and ultraviolet regions.⁷⁹

2.3.1. The Franck-Condon principle

Figure 2.5 demonstrates the principle of various electronic and vibrational transitions in a molecule, both in the ground and excited electronic states. The curves represent the relative energy of the diatomic system as a function of nuclear separation. The energy minima in each curve correspond to the equilibrium interatomic distance for each state. Horizontal lines show the vibrational states associated with each electronic state. Since molecular excitation by light absorption is very fast (about 10^{-15} s), the time is too short for the atoms in the molecule to change their position (i.e., no nuclei displacement) during the transition. In other words, the molecule in the ground and excited states will have the same electron configuration and kinetic energy. As a result, the transitions appear as vertical lines with no change in internuclear distance (Figure 2.5). This statement is known as the Franck-Condon principle. Generally, transitions occur from the ground vibrational level of the ground electronic states to various vibrational levels of a particular excited electronic state. Such optical transitions are the cause of vibrational structure in the electronic absorption spectra of molecules.^{70,74}

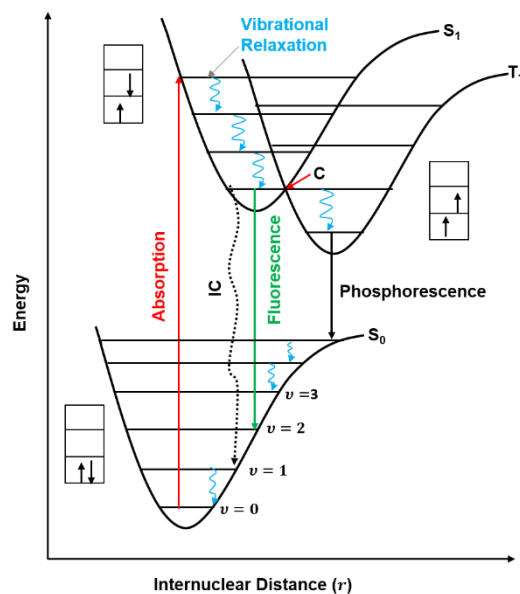


Figure 2.5. Visualizing of common electronic transitions with a Morse potential of a diatomic molecule and Franck-Condon transitions. The position and the spin of the excited singlet and triplet states relative to the ground state are shown in the boxes. The intersystem crossing has maximum probability at point C, where the energy and the geometry of S_1 and T_1 states are equal.⁷⁰

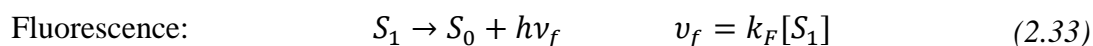
2.3.2. The Fates of the Excited States

An excited molecule can decay to the ground state by deexcitation accompanied by photon emission (radiative process) or nonradiative ways.^{80,81} The major nonradiative processes are vibrational relaxation, internal conversion, and intersystem crossing. Upon photon excitation, the molecule may be promoted to various vibrational levels of S_1 , S_2 , etc. The probability of finding an electron in one of the possible S_n excited states depends on the excitation wavelength and the transition probability. The excited molecule quickly relaxes to the lowest vibrational level of a respective excited electronic state through the process known as vibrational relaxation, Figure 2.5.

On the other hand, internal conversion (IC) is a nonradiative transition between different electronic states of the same multiplicity: singlet-to-singlet or triplet-to-triplet. Internal conversion from the first singlet excited state (S_1) to ground state (S_0) is possible but is less probable than conversion from S_2 to S_1 , due to the much larger energy gap between S_1 and S_0 . The singlet and triplet excited states share a common geometry at the point where their potential energy curves intersect (point C in Figure 2.5). At this point, the probability of crossover between electronic states of different multiplicity, as shown in the case of S_1 to T_1

states, is relatively higher. This nonradiative transition between states of different multiplicity is known as intersystem crossing (ISC).⁸²

Fluorescence and phosphorescence are common radiative processes. In fluorescence, a photon is emitted during the transition between electronic states of the same multiplicity, while in phosphorescence, a photon is emitted in a transition between electronic states of different multiplicities (Figure 2.5). The transition from T_1 to the singlet ground state is not spin allowed, and as a result, the rate of phosphorescence is several orders of magnitude lower than that of fluorescence. Phosphorescence is easily observed with molecules that contain heavy atoms such as iodine or bromine. The spin and orbital interaction increase, and the spin-flipping become more favourable.⁸⁰ For singlet excited state, the rates (ν) of the radiative and nonradiative process are given by^{70,74}



where S_0 corresponds to the ground state absorbing species, S_1 to an excited state and T_1 to an excited triplet state, $h\nu_f$ is the energy of fluorescence photons. k_F , k_{IC} , and k_{ISC} are the rate constants of fluorescence, internal conversion, and intersystem crossing, respectively. The excited state decays by a first-order process, and the decay rate of S_1 is given by

$$\frac{-d[S_1]}{dt} = (k_F + k_{IC} + k_{ISC})[S_1] \quad (2.36)$$

Thus, the concentration of S_1 varies with time as:

$$[S_1]_t = [S_1]_0 e^{-t/\tau_F}. \quad (2.37)$$

The fluorescence lifetime (τ_F) - the average time the molecule spends in the S_1 state before the spontaneous emission occurs is given by

$$\tau_F = \frac{1}{k_F + k_{IC} + k_{ISC}}. \quad (2.38)$$

Another characteristic of a fluorophore is the quantum yield (ϕ_F), which is given by

$$\phi_F = \frac{k_F}{k_F + k_{IC} + k_{ISC}} \quad (2.39)$$

Lifetime and the quantum yield of an emitter are affected by the interaction of the excited molecule with its environment; these can then provide information about such microenvironment, which opens a way to control the emission properties of molecules.

2.4. Weak Light-Matter Coupling

As briefly described in Chapter 1, weak light-matter coupling occurs when the coupling constant is smaller than the loss rate because of either leakage of photons from the cavity or decay to non-resonant modes. The main effect of the cavity in this regime is to enhance or suppress the spontaneous emission rate.

2.4.1. Fermi's Golden Rule

Quantum emitters in the excited states can return to their equilibrium (ground) state by emitting photons. This fundamental phenomenon is known as spontaneous emission. Spontaneous emission is mediated by the interaction of emitters with the vacuum field. The role of the vacuum field is to drive every excited state to its ground state.⁸³ Thus, spontaneous emission is a typical quantum mechanical process; we cannot tell when a given excited state will decay; instead, we can say that, on average, a given excited state has a certain lifetime, or one can only predict the probability of spontaneous emission. The probability of spontaneous emission, for instance, between the S_1 and S_0 states is given by Fermi's golden rule:^{21,84}

$$\Gamma_{S_1 \rightarrow S_0} = \frac{2\pi}{\hbar^2} |M_{12}|^2 \rho(\omega), \quad (2.40)$$

$\Gamma_{S_1 \rightarrow S_0}$ is a radiative rate for the transition between the excited state S_1 and ground state S_0 ; M_{12} is a transition matrix element that connects the excited and lower energy levels and is determined by the integral over the initial and final wavefunctions and the dipole moment

operator; $\rho(\omega)$ is a wavelength-dependent local density of states (LDOS).^{84,85} The LDOS quantifies the availability of photonic states at a specific position and frequency. For a large cavity volume (V_0), which has a negligible effect on the properties of a quantum emitter and is only included to simplify the calculation, the LDOS in free space is given by:

$$\rho(\omega) = \frac{\omega^2 V_0}{\pi^2 c^3}, \quad (2.41)$$

Similarly, for a large V_0 , the transition matrix element, averaged over all the possible direction, is given by:²¹

$$M_{12}^2 = \frac{1}{3} \boldsymbol{\mu}^2 \varepsilon_{vac}^2 = \frac{\mu^2 \hbar \omega}{6 \epsilon_0 V_0}, \quad (2.42)$$

where $\boldsymbol{\mu}$ is the transition dipole moment and ε_{vac} is the vacuum electric field, equal to $\sqrt{\frac{\hbar \omega}{2 \epsilon_0 V_0}}$.

After substituting Eqn. 2.41 and Eqn. 2.42 in Eqn. 2.40, we find the spontaneous emission rate in free-space:

$$\Gamma_{S_1 \rightarrow S_0} \equiv \frac{1}{\tau_{S_1 \rightarrow S_0}} = \frac{1}{3} \frac{\mu^2 \omega^3}{\hbar \pi \epsilon_0 c^3}, \quad (2.43)$$

where $\tau_{S_1 \rightarrow S_0}$ is the spontaneous emission lifetime. Hence, the spontaneous emission rate is proportional to the cube of the frequency and the square of the transition dipole moment.

2.4.2. The Purcell Effect

To derive the rate of spontaneous emission for a quantum emitter placed inside a cavity, let us consider a cavity with a single frequency (ω_c). The following derivations are based on Fox, M.²¹ The local density of states function $\rho(\omega)$ for the cavity, is described by the Lorentz equation:

$$\rho(\omega) = \frac{2}{\pi \Delta \omega_c} \frac{\Delta \omega_c^2}{4(\omega - \omega_c)^2 + \Delta \omega_c^2}, \quad (2.44)$$

where $\Delta \omega$ is the linewidth of the cavity mode. If the frequency of quantum emitter is ω_m , then we should evaluate Eqn. 2.44 at ω_m :

$$\rho(\omega_m) = \frac{2}{\pi\Delta\omega_c} \frac{\Delta\omega_c^2}{4(\omega_m - \omega_c)^2 + \Delta\omega_c^2}. \quad (2.45)$$

At the resonance between the quantum emitter and the cavity (i.e., $\omega_m = \omega_c$), Eqn. 2.45 reduces to:

$$\rho(\omega_m) = \frac{2}{\pi\Delta\omega_c} = \frac{2Q}{\omega_m\pi}. \quad (2.46)$$

As in the case of free-space, the electric dipole matrix element is given by

$$M_{12}^2 = \xi^2 \mu^2 \epsilon_{vac}^2 = \xi^2 \frac{\mu^2 \hbar \omega}{2\epsilon_0 V_0}, \quad (2.47)$$

here ξ^2 is the normalization factor, and it is averaged to $1/3$ for a randomly oriented dipole in free-space. Using Eqns. 2.40, 2.45, and 2.47, we can obtain the spontaneous emission of an emitter placed within a microcavity,

$$\Gamma_{S_1 \rightarrow S_0}^{cav} = \frac{2\mu^2 Q}{\epsilon_0 \hbar V_0} \xi^2 \frac{\Delta\omega_c^2}{4(\omega_m - \omega_c)^2 + \Delta\omega_c^2}, \quad (2.48)$$

The **Purcell factor** (F_P) is defined by:

$$F_P = \frac{\Gamma_{S_1 \rightarrow S_0}^{cav}}{\Gamma_{S_1 \rightarrow S_0}}. \quad (2.49)$$

Through substituting Eqn. 2.43 and Eqn. 2.48 to Eqn. 2.49, and replacing $\frac{c}{\omega}$ by $\frac{(\lambda/n)}{2\pi}$ we can then find:

$$F_P = \frac{3Q(\lambda/n)^3}{4\pi^2 V} \xi^2 \frac{\Delta\omega_c^2}{4(\omega_m - \omega_c)^2 + \Delta\omega_c^2}, \quad (2.50)$$

where n is the refractive index, and λ is the free-space wavelength. When $\omega_c = \omega_m$, $n = 1$, and with the dipoles oriented along the field direction, Eqn. 2.50 reduced to the well-known Purcell factor:

$$F_p = \frac{3Q\lambda^3}{4\pi^2V}. \quad (2.51)$$

Eqn. 2.51 shows that large Purcell factor requires high Q cavities with small modal volumes. Emission rate enhancement in the case of on-resonance samples is due to large values of the density of states function at the cavity mode frequency. In contrast, the inhibition of emission, when the atom is off-resonance, is caused by the absence of photon modes into which the atom can emit. $F_p > 1$ means that the spontaneous emission rate is enhanced by the cavity, while $F_p < 1$ implies that the cavity reduces spontaneous emission.⁸⁶

2.5. Theory of Strong Light-Matter Coupling

In the strong coupling regime, the matter and the light degrees of freedom are mixed into dressed states, which results in new eigenstates. To explain this phenomenon theoretically, one must find an expression for the polaritonic eigenstates and their energy eigenvalues. The strong coupling phenomenon can be described by using classical, semiclassical, or quantum mechanical models. After explaining the basic features of strong coupling based on a classical approach, we shall finally discuss the quantum mechanical models, which are general enough to be applied in the regimes where the classical models are inaccurate.

2.5.1. Classical Description of Strong Light-Matter Coupling

Coupled harmonic oscillators are an intuitive model to describe the key features of strong light-matter coupling, such as energy splitting and anticrossing behavior. Let us consider two coupled harmonic oscillators with frequencies of ω_1 and ω_2 and the exchange of energy between them by a coupling spring (Figure 2.6). Each oscillator can dissipate energy into the environment by friction. Without the coupling ($\kappa = 0$), the two harmonic oscillators behave independently, and they display their characteristic measurement parameters, for instance, their natural frequencies. However, in the coupling, the two oscillators start to exchange energy periodically, and when the coupling dominates dissipation rates, the energy spectrum of the system can be modified and show up two split modes. Without damping, the equations of motion for the coupled harmonic oscillators can be written as follows:⁸⁷

$$\begin{aligned}
m_1 \ddot{x}_1 + k_1 x_1 + \kappa(x_1 - x_2) &= 0 \\
m_2 \ddot{x}_2 + k_2 x_2 - \kappa(x_1 - x_2) &= 0.
\end{aligned}
\tag{2.52}$$

Solving these differential equations give two normal modes:

$$\omega_{\pm}^2 = \frac{1}{2} [\omega_1^2 + \omega_2^2 \pm \sqrt{(\omega_1^2 - \omega_2^2)^2 + 4\Gamma^2 \omega_1 \omega_2}],
\tag{2.53}$$

where $\omega_1 = \sqrt{k_1 + \kappa/m_1}$, $\omega_2 = \sqrt{k_2 + \kappa/m_2}$, and $\Gamma = \frac{\sqrt{\kappa/m_1} \sqrt{\kappa/m_2}}{\sqrt{\omega_1 \omega_2}}$

Eqn. 2.53 shows that the eigenfrequencies of the coupled harmonic oscillators, ω_{\pm} , are hybrid modes of the original oscillator frequencies. These modes can be considered analogies to the hybrid light-matter states formed during the strong light-matter coupling phenomenon. Novotny⁸⁷ illustrated the solutions of Eqn. 2.53 by setting $k_1 = k_0$, $k_2 = k_0 + \Delta k$, and $m_1 = m_2 = m_0$. In absence of coupling, when Δk increases from $-k_0$ to k_0 the frequency of the second oscillator changes from 0 to $\sqrt{2}\omega_0$, whereas the frequency of the first oscillator remains constant. At $\Delta k = 0$, the two curves intersect (Figure 2.7a), while in the presence of strong coupling, the two modes no longer intersect; they showed anticrossing behavior with a frequency of splitting: $\omega_+ - \omega_- = \Gamma$ (Figure 2.7b).

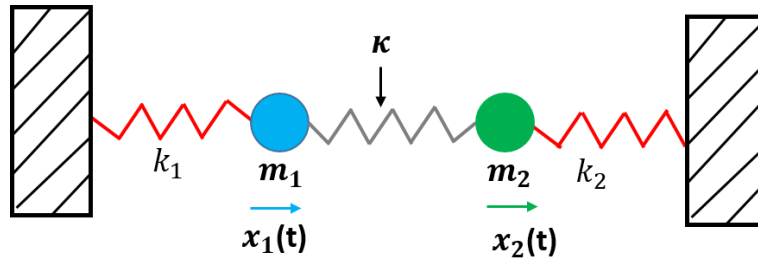


Figure 2.6. Coupled oscillators with mass m_i and spring constant k_i . The coupling results in a characteristic frequency splitting. κ is the coupling strength.⁸⁷

Anticrossing is a typical characteristic feature of a strong coupling effect. The exciton and photon can be considered as coupled oscillators and described by a two-level coupled oscillator model. The energy of the upper (UP) and lower (LP) polaritonic modes ($E_{UP/LP}$) are given by:⁸⁸

$$E_{UP/LP} = \frac{E_c^2 + E_m^2}{2} \pm \frac{1}{2} \sqrt{(E_c - E_m)^2 + (\hbar\Omega_R)^2}, \quad (2.54)$$

where E_c , E_m , and Ω_R are cavity energy, the energy of exciton, and the Rabi frequency, respectively. Lidzey and Coles plotted the solutions of Eqn. 2.54 (Figure 2.7c) by substituting the values of E_c calculated at different incident angles (θ_{ext}) using the following formula:

$$E_c = \frac{\hbar c}{2nL} \left(1 - \frac{\sin^2 \theta_{ext}}{n} \right), \quad (2.55)$$

where L and n are the cavity length and the refractive index of the cavity, respectively.

As shown in Figure 2.7c, when E_c and E_m become isoenergetic, the UP and LP modes undergo an anticrossing. At this point, both the UP and LP states are 50 % photon and 50 % exciton. At large angles, the UP will become more photonic, and the LP will show more excitonic character. The situation is reversed for smaller angles.⁸⁸

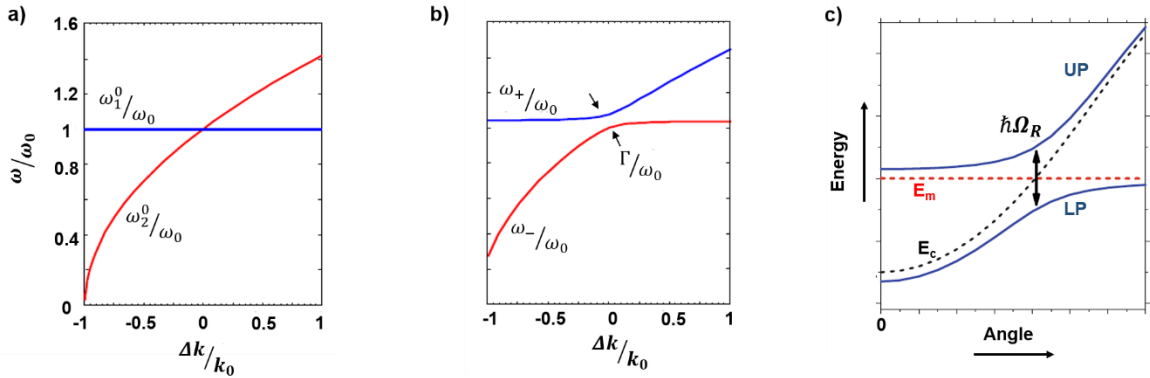


Figure 2.7. (a) In the absence of the coupling ($\kappa = 0$), the frequencies of the two uncoupled oscillators, having equal mass and spring constants k_0 and $k_0 + \Delta k$, intersect at $\Delta k = 0$. (b) When two oscillators are coupled, the new eigenfrequencies show anticrossing behavior, from Novotny⁸⁷ (c) Anticrossing behavior of polariton peaks. Red and black dash lines show the cavity photon and exciton energy dispersion. The upper (UP) and lower (LP) polariton modes dispersion are shown in blue, and $\hbar\Omega_R$ is the Rabi splitting.⁸⁸

2.5.2. Quantum Description of Strong Coupling

A fully quantum mechanical formalism that has been widely used to explain the strong coupling phenomenon is the Jaynes–Cummings (JC) model. JC model describes only the

interaction of a single emitter with a single quantized cavity mode. The emitter is approximated by a two-level system (Figure 2.8), and its ground and excited states are represented by $|g\rangle$ and $|e\rangle$. These states are separated by energy $\hbar\omega_m$, where ω_m is the transition frequency. The two-level system is described by raising ($\hat{\sigma}^\dagger$) and lowering ($\hat{\sigma}$) operators. The $\hat{\sigma}^\dagger$ the operator generates a transition from the $|g\rangle$ state to the $|e\rangle$ state, while the operator $\hat{\sigma}$ does the opposite. Thus, the Hamiltonian of the two-level emitter (\hat{H}_m) reads^{89,90}

$$\hat{H}_s = \hbar\omega_m \hat{\sigma}^\dagger \hat{\sigma}. \quad (2.56)$$

The cavity mode is modelled as a quantized harmonic oscillator, and it is represented by the number states or the Fock states $|n\rangle$. The quantized electromagnetic field is described by the photon creation ($\hat{\alpha}^\dagger$) and annihilation ($\hat{\alpha}$) operators. These operators are defined by:²¹

$$\hat{\alpha}^\dagger |n\rangle = \sqrt{n+1} |n+1\rangle \quad (2.57)$$

$$\hat{\alpha} |n\rangle = \sqrt{n} |n-1\rangle. \quad (2.58)$$

The operator $\hat{\alpha}^\dagger$ creates a quantum of energy or one photon, whereas $\hat{\alpha}$ does the opposite and lowers the system from $|n\rangle$ to $|n-1\rangle$ states. A microcavity that confines a photon of energy $\hbar\omega_c$ is described by the cavity Hamiltonian (\hat{H}_{cav}) and after dropping the zero-point energy term, the \hat{H}_{cav} is then written as⁹¹

$$\hat{H}_{cav} = \hbar\omega_c \hat{\alpha}^\dagger \hat{\alpha}. \quad (2.59)$$

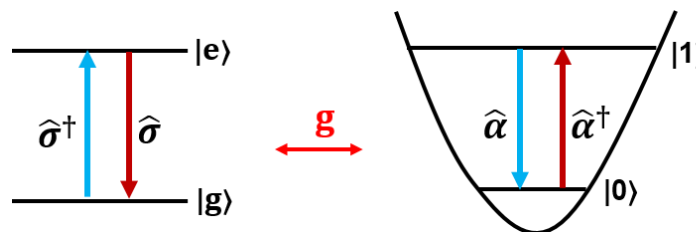


Figure 2.8. The JC model combines the two fundamental models of quantum mechanics: the two-level system and the quantized harmonic oscillator, to describe the properties of an emitter coupled with a single cavity mode. The coupling is characterized by a coupling strength g . Loss of excitation in the two levels system appears as a gain in the excitation of the oscillator and vice versa.⁸⁹

The emitter interacts with the quantized cavity mode by a dipole transition operator, which is represented as^{40,91}

$$\hat{\mathbf{D}} = \boldsymbol{\mu}(\hat{\sigma}^\dagger + \hat{\sigma}), \quad (2.60)$$

where $\boldsymbol{\mu}$ is the molecular transition dipole moment. The emitter-cavity interaction Hamiltonian operator reads

$$\hat{H}_{int} = \hat{\mathbf{D}} \cdot \mathbf{E}(\mathbf{r}_d), \quad (2.61)$$

here $\mathbf{E}(\mathbf{r}_d) = \varepsilon_{vac}(\hat{\alpha}^\dagger + \hat{\alpha})$ is the electric field operator at the position of the emitter, where ε_{vac} is the vacuum electric field. Hence, the interaction Hamiltonian can be written as

$$\hat{H}_{int} = \hbar g(\hat{\alpha}^\dagger + \hat{\alpha})(\hat{\sigma}^\dagger + \hat{\sigma}), \quad (2.62)$$

where $\hbar g = \varepsilon_{vac}\boldsymbol{\mu}$ is the coupling strength. By omitting the terms that do not correspond to absorption or emission of a single photon (or terms that do not conserve the number of excitation), such as $\hat{\alpha}^\dagger\hat{\sigma}^\dagger$ and $\hat{\alpha}\hat{\sigma}$, the light-matter coupling term is then written as⁹¹

$$\hat{H}_{int} = \hbar g(\hat{\sigma}\hat{\alpha}^\dagger + \hat{\sigma}^\dagger\hat{\alpha}). \quad (2.63)$$

The term $\hat{\alpha}^\dagger\hat{\sigma}$ in Eqn. 2.63 describes an emission of a single photon, whereas $\hat{\alpha}\hat{\sigma}^\dagger$ describes the promotion of an emitter to the excited state by absorption of a photon.⁹¹ For a single two-level system interacting with a cavity mode, the effective Hamiltonian is the sum of the single emitter excitation, the cavity excitation, and the atom-field interaction Hamiltonians. Therefore, the \hat{H}_{JC} takes the form

$$\hat{H}_{JC} = \hbar\omega_m\hat{\sigma}^\dagger\hat{\sigma} + \hbar\omega_c\hat{\alpha}^\dagger\hat{\alpha} + \hbar g(\hat{\sigma}\hat{\alpha}^\dagger + \hat{\sigma}^\dagger\hat{\alpha}). \quad (2.64)$$

JC Hamiltonian predicts quantum hybridization between the excitations in the emitter and in the cavity, which leads to the idea of the so-called dressed light-matter states. In the case of resonance interaction (when $\omega_m = \omega_c$), JC Hamiltonian results in the following eigenstates:^{40,92}

$$|\pm\rangle_n = \frac{1}{\sqrt{2}}(|g, n_{ph} + 1\rangle \pm |e, n_{ph}\rangle). \quad (2.65)$$

The corresponding eigenvalues of energies are:³¹

$$E_{\pm n} = \hbar\omega \left(n + \frac{1}{2} \right) \pm \hbar g \sqrt{n_{ph} + 1}, \quad (2.66)$$

where n_{ph} is the number of photons. The new eigenstates are the superposition of the emitter and the quantized cavity field. At resonance, the emitter and the cavity mode contribute equally to the dressed light-matter states, termed upper (UP) and lower (LP) polaritons. The energy difference between these states - Rabi splitting ($\hbar\Omega_R$) - is given by

$$\hbar\Omega_R = 2\hbar g \sqrt{n_{ph} + 1} = 2\boldsymbol{\mu} \sqrt{\frac{\hbar\omega_c}{2\epsilon_0 V}} \sqrt{n_{ph} + 1}, \quad (2.67)$$

where $\boldsymbol{\mu}$ is the transition dipole moment of the emitter, and V is the mode volume of the cavity.

In practice, the single molecule-cavity coupling is rarely observed at ambient conditions, as it requires a very high- Q -low- V cavity with a high transition dipole moment of the molecule.⁹³ Thus, strong coupling experiments are mostly performed using an ensemble of molecules. The Tavis–Cummings (TC) or Dicke model - an extension of JC model - has been employed to describe the interaction of N identical two-level emitters strongly interacting with a single cavity mode. The Tavis–Cummings Hamiltonian (\hat{H}_{TC}), in the case of N emitters coupled with a single cavity mode, is given by^{40,94}

$$\hat{H}_{TC} = \hbar\omega_c \hat{a}^\dagger \hat{a} + \sum_j \hbar\omega_m \hat{\sigma}_j^\dagger \hat{\sigma}_j + \hbar \sum_j g_j (\hat{\sigma}_j \hat{a}^\dagger + \hat{\sigma}_j^\dagger \hat{a}), \quad (2.68)$$

here the superscript j indicates each of the N emitters.

For N identical emitters similarly coupled to the cavity ($g_j \equiv g$), solving the \hat{H}_{TC} results in two bright dressed states:

$$|1, +\rangle = \frac{|g, \dots, g\rangle |1\rangle \pm \frac{1}{\sqrt{N}} \sum_j \hat{\sigma}_j^\dagger |g, \dots, g\rangle |0\rangle}{\sqrt{2}}. \quad (2.69)$$

At resonance, the eigenstates of \hat{H}_{TC} shows the Rabi splitting increase with a factor \sqrt{N} :

$$\hbar\Omega_R = 2\sqrt{N}g\hbar = 2\mu\sqrt{\frac{\hbar\omega_c N}{2\epsilon_0 V}}. \quad (2.70)$$

$\hbar\Omega_R \propto \sqrt{\frac{N}{V}} = \sqrt{C}$,³¹ where C is the concentration of the two level system. Hence, strong coupling can be easily achieved by increasing the concentration of molecules in the mode volume of the cavity.

In addition to two bright states, the single excitation subspace also contains $(N - 1)$ dark states orthogonal to $|1, +\rangle$. According to Baranov et al.,⁴⁰ the wave function of dark states can be written as:

$$|D\rangle = \frac{1}{2}(\hat{\sigma}_1^\dagger - \hat{\sigma}_j^\dagger)|G\rangle, j > 1. \quad (2.71)$$

The excitonic dark states do not couple with the cavity mode, and their energies are the same as the energy of the uncoupled excited emitters. These states are called dark states, as the transition dipole moment between the global ground state $|G\rangle$, $|g, \dots, g\rangle \otimes |0\rangle$, and any of these states is zero. Dark states (also called ‘‘exciton reservoir’’) have a significant role in the deexcitation processes of the coupled systems; the upper polariton state depopulates to these states with a fast rate (150 fs).⁹⁵ Moreover, considering the dark states is also important in the description of the effects of strong coupling on chemical dynamics.^{50,62}

3. Materials and Methods

In this chapter, the fundamental principles of the methods used to prepare samples and optical instruments employed to collect the experimental data are described. The chemicals and materials used in this work are listed in section 3.1. The working principles of physical vapor deposition techniques employed to prepare microcavity mirrors and the spin coating method are explained in section 3.2. Section 3.3 aims to explain the basic ideas and parameters of the optical settings used in this work.

3.1. Chemicals and Materials

Methyl salicylate (99%), methylcyclohexane (99%), benzonitrile (99%), toluene (99%), polyvinyl acetate (MW: 100,000), phthalocyanine tetrasulfonate (99%), and polyvinyl alcohol (MW: 85,000) were purchased from Sigma-Aldrich and used without further purification. Spectroscopic-grade methanol was obtained from Merck, Germany. For all single-molecule studies, solutions were prepared with triply distilled water.

Silver and gold targets ($d = 54$ mm, 0.2 mm thickness, 99.9%) used to prepare IR-microcavity mirrors were supplied by Mennica-Metal Sp. z o.o. CaF_2 substrates ($d = 25.0$ mm, 5.0 mm thickness) were obtained from Crystran Ltd.; mirror mounts with piezoelectric control (Thorlabs, KC1-PZ/M) were purchased from Thorlabs, Inc.

The silver wire (99.9%) used to prepare $\lambda/2$ -microcavity mirrors was obtained from Johnson Matthey GmbH. SiO_2 pieces (99.9%) and the chromium were from chemPure. Microscope coverslips (22 x 22 mm) were used as a substrate to prepare the bottom mirrors of $\lambda/2$ -microcavities. A N-BK7 plano-convex lens (Thorlabs, Inc) was employed as a substrate to prepare the upper mirror of the $\lambda/2$ -microcavities.

3.2. Sample Preparations

3.2.1. Optical Microcavity Mirrors Preparation

Here we shall describe the methods employed to prepare the microcavity mirrors. The design and the characterization of various microcavities were described in the results and discussion sections of Chapters 4, 5, and 6. The microcavity mirrors were prepared by using physical vapor deposition (PVD) techniques. In this work, the PVD was conducted by either sputtering or electron-beam evaporation techniques and will be briefly described in the following sections. For further information on these methods, see, for instance, Swann⁹⁶ and Seshan.⁹⁷

The IR-microcavity was prepared using a magnetron sputtering technique. Sputtering is a PVD method in which atoms are ejected from the cathodically connected source material (a target) by a bombardment of high-energy particles (mostly ions from inert gases).⁹⁶ The IR-microcavity mirrors used in this work were prepared using a direct current (DC) magnetron sputter coater (Leica EM MED 020). Figure 3.1 illustrates the working principles of this technique. The target (either Au or Ag) and the substrate (CaF₂ window) were placed in the sputtering chamber. When the base pressure reached 10⁻⁵ mbar, argon gas was introduced into the sputtering chamber. The sputtering was started when the working pressure reached 2.0 x 10⁻² mbar. The low pressure is required to avoid atom gas collisions after ejection from the target. The sputtering current was kept constant at 25 mA for the preparation of both Au and Ag mirrors. First, a plasma (argon ions) is created by ionizing argon atoms by applying high voltage using a DC power source. The argon ions were accelerated towards the surface of the target and knocked out atoms from the surface. The ejected atoms condense on the substrate surface (Figure 3.1). A tightly bound metal film was formed when more and more atoms coalesced on the substrate and started to bind to each other. The magnetron is used to enhance the sputtering process by generating a dense plasma around the target through a magnetic field.⁹³ The film thickness was controlled using the quartz crystal film thickness monitoring system (Leica EM QSG100) during the sputtering process.

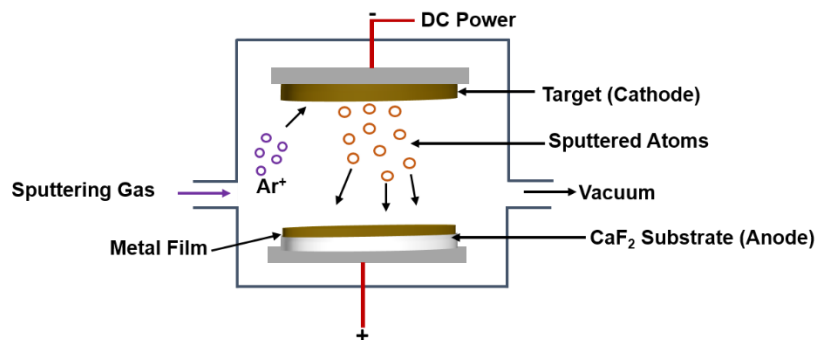


Figure 3.1. Schematic of an Au film preparation by a DC sputtering process. A constant (DC) voltage was applied in DC sputtering between the anode (substrate) and the cathode (target).⁹⁸

The metal and dielectric layers of the $\lambda/2$ -microcavity were prepared using electron-beam evaporation (EB3, Edwards). The evaporation was conducted under a high vacuum condition ($p \approx 10^{-6}$ mbar). A high voltage current (provided by the EB3 Power Supply) was passed through a tungsten filament inside the electron gun, leading to electron emission. The

electron beam was accelerated towards the crucible containing the target material to be deposited by applying a voltage. The electrons were focused on a unified beam using a magnetic field created by a permanent magnet.⁹⁹ The kinetic energy of the electron beam was transferred to the target, causing it to evaporate and deposit onto a clean microscope cover glass (Figure 3.2). The thickness of the deposited material was controlled during the evaporation process using an oscillating quartz unit (FTM7, Edwards).

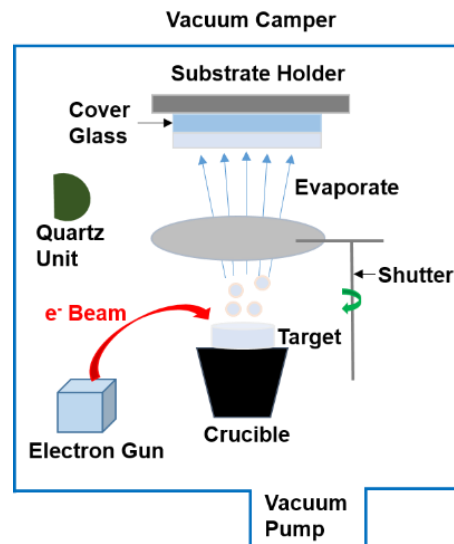


Figure 3.2. A simplified schematic illustration of electron-beam evaporation for deposition of optical microcavity mirrors.⁹⁹

3.2.2. Spin Coating

The spin coating method was employed to prepare polymer films with organic molecules embedded in the polymer. In general, the desired materials were dissolved in an appropriate solvent, and 20 μL solutions were deposited on the center of the substrates, such as uncoated CaF_2 window, clean coverslips, or the bottom cavity mirror, using a pipette. The spin coater was started immediately, and rotation of the substrate at high speed resulted in a polymer film on the substrate surface. The film thickness (h_f) generally depends on the angular velocity (ω) and the weight percent of the polymer (C):

$$h_f = KC(\omega)^\alpha, \quad (3.1)$$

where α is a constant with a value of -0.5 for most solvents, and the coefficient K depends on the solvent type, viscosity value, polymer-solvent interaction, and vaporization rate.^{100,101}

Hence, we optimized the polymer film thicknesses by varying the weight percent of the polymer and spin coating speed.

In order to investigate Raman scattering under strong coupling, polyvinyl acetate (PVAc), 15% w/w, was dissolved in toluene, and the solution was sonicated at 35 °C for 30 minutes. After cooling to room temperature, the solution was filtered using a 0.22 μm Nylon filter. Then the PVAc solution was spin-coated (Chetmat Technology INC.) at a speed of 870 rpm for 60 s. These spinning conditions ensured that one of the cavity resonances was ON resonance with the PVAc carbonyl stretch mode. The OFF resonance cavity was obtained by spin-coating the same PVAc solution at a speed of 1000 rpm for a duration of 60 s. Multiple ON and OFF resonance samples were made, and the preparation procedure proved to be highly reproducible; further details can be found in section 5.2.

For single-molecule and tautomerization studies, a solution of PVA (1% w/v) and phthalocyanine tetrasulfonate (PcS₄) (10⁻⁹ M) in water was spin-coated onto clean coverslips or onto the lower mirror of the cavity at speeds of 8000 rpm.

3.3. Optical Setups and Measurements

3.3.1. FTIR Spectrometer

For vibrational strong coupling studies, all transmission spectra were recorded with an FTIR spectrometer (Bruker VERTEX 70), equipped with a liquid-nitrogen-cooled MCT (HgCdTe) detector. All transmission spectra were obtained with a resolution of 0.5 cm⁻¹ and averaged over 50 subsequent scans. An illustration of the optical setup of the FTIR instrument is shown in Figure 3.3. The heart of the FTIR spectrometer is the Michelson interferometer, which consists of a beam splitter and two planar moving and fixed mirrors.

The beam splitter transmits half of the incident beam from the IR source towards the moving mirror and reflects the other half to the fixed mirror. An optical path difference is introduced due to reflection from the moving mirror, and the two beams are then rejoined at the beam splitter. This results in an interference pattern because of the continuous change of the optical path difference of the two mirrors. Part of the recombined beam leaves the interferometer, interacts with the sample, and is detected by the MCT detector. The interferogram output is formed when the mirror is moved at a constant velocity, as the intensity of radiation reaching the detector varies in a sinusoidal manner. The time-domain spectrum (an interferogram) is converted to an IR spectrum (frequency domain) by the mathematical operation, Fourier transformation.¹⁰²

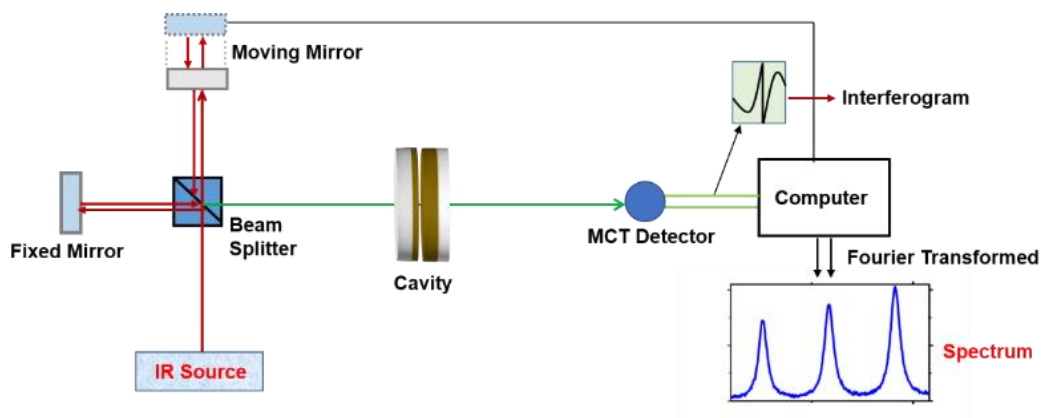


Figure 3.3. Schematic of the FTIR instrument. The interferogram obtained is recorded with an MCT (HgCdTe) detector, and Fourier transformed into the transmission spectrum of the cavity.¹⁰³

3.3.2. Raman Scattering Measurements

Raman scattering and SERS measurements were performed using Renishaw inVia micro-Raman system, operating in back-scattering geometry. For all measurements, the laser excitation wavelength was set to 532 nm. As depicted in Figure 3.4, for polymer spaced microcavities and the SERS samples, a Leica 50x 0.75 NA objective was used to focus the excitation source onto the sample and to collect the back-scattered Raman signal. A movable stage was employed to move the sample and acquire 2D mapping. Data were collected in a raster scanning fashion, and the final spectra were obtained by averaging over 140 spectra acquired from a large area of the microcavity. On the other hand, for liquid-filled open microcavity samples, the excitation laser light was focused onto the sample surface, and the back-scattering signal was collected using a long working distance Renishaw 15x objective.

A simplified setup of the micro-Raman system is shown in Figure 3.4. To remove Rayleigh scattering light, the scattered light passes through holographic notch filters. The Raman scattered signal then reaches the diffraction grating element, where the light is separated into its monochromatic components. The signal is directly sent to the thermo-electrically cooled CCD camera for detection and finally processed in the computer to obtain the Raman spectra.

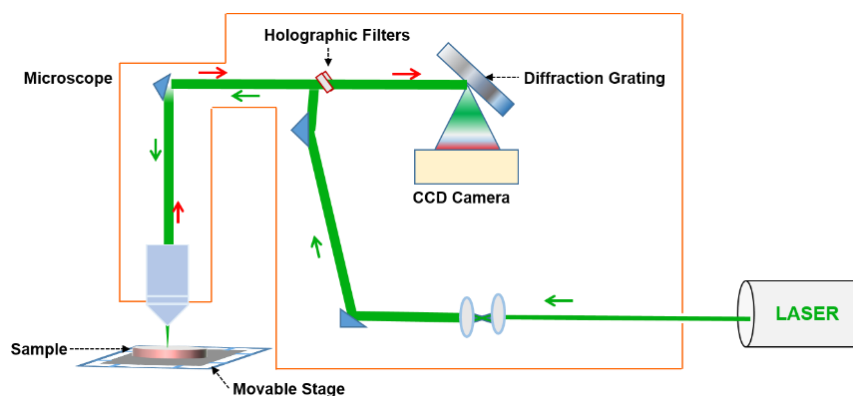


Figure 3.4. A simplified layout of the micro-Raman setup.¹⁰⁴

3.3.3. Single-Molecule Imaging and Time Trace Measurements

Since the first optical detection of single molecules at low temperatures in 1989 by Moerner and Kador,¹⁰⁵ there has been tremendous progress in single-molecule spectroscopy and imaging optics. Single-molecule emission-sensitive detectors are widely available, and versatile excitation sources have been developed. Due to these improvements, nowadays, the detection of single molecules is a routine practice in many laboratories around the world. However, studying and manipulating individual molecules is not a trivial task. In order to investigate individual fluorescent molecules, one has to: (1) maximize the collection efficiency of single-molecule emission, (2) properly reject the background signal, and (3) use very dilute samples. Finally, the observation of single molecules should be supported by time trace (fluorescence intermittency) and photon antibunching measurements.

A standard technique for studying single molecules is confocal microscopy. In this technique, a fluorophore (usually embedded in a polymer film) is illuminated by focusing the excitation source (a laser) with a high numerical aperture (NA) objective. Upon excitation, molecules emit fluorescence. A part of the fluorescence light is collected by the same objective (epi-fluorescence microscope setup). Thus, the objective lens is a crucial component of the single-molecule optical system. The NA is defined as:

$$NA = n \sin \alpha, \quad (3.2)$$

where n is the refractive index of the medium between the objective lens and the sample, and α is the largest angle that can be collected by the objective lens.

The ability to identify the smallest distance between two adjacent objects (d_{min}) is inversely related to the NA and given by Abbe's formula:

$$d_{min} = 0.61 \frac{\lambda}{NA}, \quad (3.3)$$

where λ is the wavelength of the excitation source.

Eqn. 3.3 shows that the best resolution that can be reached is $\sim 200 \text{ nm}$, by considering the best conditions such as a 400 nm excitation light and an oil immersion objective with 1.4 NA.¹⁰⁶ Thus, the spatial resolution of a single-molecule confocal image is limited by diffraction. Background signal reduction can be done using high-quality optical filters, and a pinhole can be placed in the detection path to avoid out-focused light.

In this work, single-molecule imaging, time trace, photon antibunching, and lifetime measurements were performed using a home-built laser scanning confocal microscope. A scheme of the setup is depicted in Figure 3.5. For single-molecule imaging, a continuous-wave 633 nm (5 μW , Gaussian laser mode) was used as the excitation source. The excitation was passed through an appropriate band-pass filter (BPF) and focused onto an illumination pinhole ($d = 20 \mu\text{m}$). A neutral density (ND) filter was employed to adjust the incident laser power. The collimated excitation beam was reflected by a dichroic mirror beam splitter and focused onto the sample by a high numerical aperture oil objective lens (Carl Zeiss, $NA = 1.46$). The fluorescence emission, collected by the same objective lens, passes through the dichroic mirror, and is separated from residual reflected laser light by using a long-pass (LP) filter. By raster scanning the sample through the focal spot, fluorescence confocal images were detected using an avalanche photodiode (APD). For the spectral measurements, a spectrograph (SP-2500i, Princeton Instruments) equipped with an internally cooled CCD camera (ProEM:512B+, Princeton Instruments) was used. For photon antibunching and fluorescence decay studies, the confocal setting was coupled with the Time Correlation Single Photon Counting (TCSPC) module (HydraHarp 400, PicoQuant, Germany).

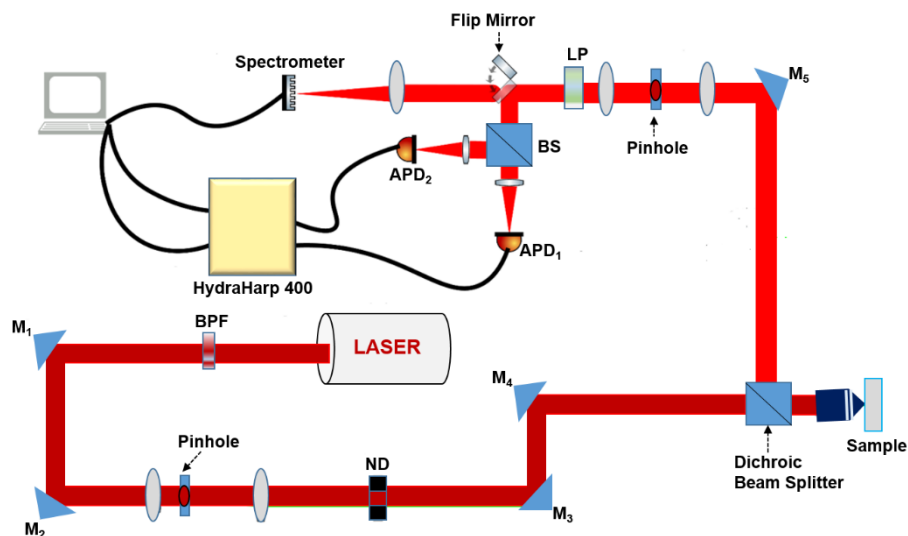


Figure 3.5. Illustration of the home-built laser scanning confocal microscope and a dual detection system for antibunching measurements.

3.3.4. Photon Antibunching Measurements

A direct proof for the presence of only a single molecule in the sample is the observation of photon antibunching. This purely quantum mechanical phenomenon enables one to determine the number of emitters contributing in a ray of light.¹⁰⁷ Conceptually, antibunching means a finite temporal separation between photons.

For photon antibunching measurements, the fluorescence signal is split by a 50:50 non-polarizing beam splitter and focused onto two APDs (Figure 3.5). This is the Hanbury-Brown and Twiss setup for antibunching measurements. One detector is used to provide a ‘start’ signal, and the other, which records with a delay, is used to provide a ‘stop’ signal. The APDs were connected with Time-Correlated Single Photon Counting (TCSPC) module, and the photons impinging on the detectors were detected by the TCSPC. This measurement gives a histogram of the time differences between the photons at both detectors and the photon antibunching data are analyzed with a commercial software SymPhoTime 64 (PicoQuant, Germany). Both continuous-wave (633 nm) and pulsed excitation (640 nm, 10 MHz) were used during photon antibunching measurements.

3.3.5. Fluorescence Decay Measurements

The fluorescence decay of individual molecules were measured using TCSPC. A pulsed laser ($\lambda_{\text{ex}} = 640 \text{ nm}$, $5 \mu\text{W}$) with a repetition rate of 10 MHz was employed as the excitation source. The fluorescence decay curves were analysed and fitted with SymPhoTime 64, and the fluorescence lifetime was determined from the decay curves.

TCSPC is a statistical method that is based on the detection and counting of individual photons. The arrival time of the single photons is measured repetitively with respect to the pulsed laser light source (the reference signal). This technique can be considered as a ‘stopwatch’ or a start-stop method. The ‘start’ signal is provided by the laser pulse, and the ‘stop’ signal is achieved by the detection of a single photon from the fluorophore with the APD. The measurement of this time delay is repeated many times to account for the statistical nature of the fluorophores emission. The delay times are sorted into a histogram that plots the occurrence of emission over time after the excitation. Finally, the fluorescence lifetime of the molecule can be extracted by an exponential fitting of this histogram.¹⁰⁸ One limitation of the analysis of TCSPC measurements is the fact that, in general, the temporal length of the laser pulse and instrumental noises cannot be neglected. Thus, the total observed fluorescence decay $R(t)$ is represented as a convolution of the instrument response function (IRF) $G(t)$ with the impulse response of the sample, which would be obtained by applying an infinitesimally small δ -pulse, $F(t)$. Thus:⁸²

$$R(t) = \int_0^t G(t^*) F(t - t^*) dt^*. \quad (3.4)$$

Experimentally, the IRF was acquired by recording the temporal profile of the excitation light. It contains all of the relevant correction factors for the detector and the complete TCSPC system.

3.3.6. Imaging Single-Molecule Tautomerization Reactions

For imaging of the single-molecule tautomerization reaction, azimuthally (APDM) and radially (RDPM) polarized doughnut-modes were used as excitation sources. Since these beams have a ring shape with a circular intensity profile and zero intensity in the center, they are known as doughnut modes. The properties of laser beam propagation modes can be found by solving the scalar Helmholtz equation:^{109,110}

$$(\nabla^2 + k^2)\mathbf{E} = 0, \quad (3.5)$$

where \mathbf{E} and k are the electric field and the wavenumber, respectively. The well-known solutions of Eqn. 3.5, under the paraxial limit, are Hermite-Gauss modes (HG) and Laguerre-Gauss modes (LG). Mathematically, doughnut modes can be expressed as a linear combination of HG and LG modes.¹¹⁰ There are two ways to generate doughnut modes: either inside a laser cavity or by directly converting the normal Gaussian mode using a mode converter (i.e., outside the laser cavity). The latter is a widely used method due to its experimental simplicity and flexibility.¹⁰⁹ In this work, APDM and RDPM were generated by propagating the Gaussian shaped beam of a 633 nm laser through a commercial mode converter (Arcoptix). The resulting image pattern reflects the orientation of the transition dipole moment and the tautomerization reaction of the single PcS₄ molecule can be directly observed by a reorientation of the pattern.

4. Multimode Vibrational Strong Coupling Using a Tunable Microcavity

This chapter is based on:

Takele, W. M.; Wackenhut, F.; Piatkowski, L.; Meixner, A. J.; Waluk, J. Multimode Vibrational Strong Coupling of Methyl Salicylate to a Fabry–Pérot Microcavity. *J. Phys. Chem. B* **2020**, *124*, 5709-5716.

4.1. Introduction

Controlling molecular vibrations is crucial, since they play a central role in studying the structure, dynamics, and composition of matter.¹¹¹ Over the decades, overcoming the barrier of a chemical reaction by exciting molecular vibration with an intense laser field has been employed as a physical method to control chemical reactivity.¹¹² The main challenge in this approach is the redistribution of excitation energy to the vibrational degrees of freedoms that are not involved in the chemical reaction coordinate.¹¹³ Another option is vibrational strong coupling (VSC), where the chemical dynamics can be controlled by the zero-point-energy of fluctuations of the optical mode of the cavity.^{60,61} VSC is attained when IR-active molecular vibrations hybridize with the vacuum electric field of an IR microcavity. Consequently, a vibrational transition splits into lower (VP^-) and higher (VP^+) vibrational polaritons, separated by the vibrational Rabi splitting energy ($\hbar\Omega_R$), which is illustrated in Figure 4.1.¹¹⁴

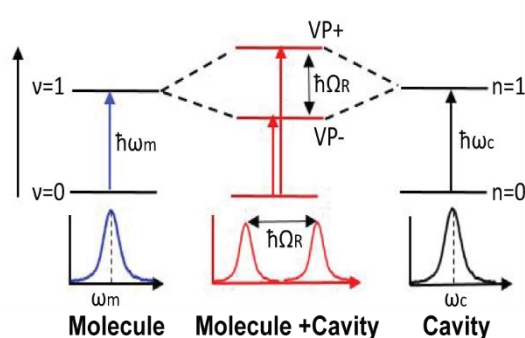


Figure 4.1. Schematic illustration of vibrational strong coupling: when the molecular vibration frequency (ω_m) becomes isoenergetic with the cavity mode (ω_m), the lower (VP^-) and upper (VP^+) vibrational polaritons can be formed. Adapted from ref. 114. Copyright (2020) American Chemical Society.

Experimentally, the VP^+ and VP^- states can be seen in the transmission spectrum of the coupled system, as two new peaks with energies shifted from the original frequency by half the

Rabi splitting. This, in turn, has been claimed to provide a novel way to tailor thermally activated ground state chemical reactions. Indeed, in 2016, Thomas et al.¹¹⁵ have confirmed that coupling the vibrational transition involving the silane deprotection reaction to the cavity mode can decrease the reaction rate by modifying the transition state of the reaction from an associative to a dissociative type. On the other hand, recently, Lather et al.¹¹⁶ demonstrated the catalytic effect of VSC on the solvolysis of *para*-nitrophenyl acetate; speeding up the reaction rate by an order of magnitude was observed when the cavity mode was tuned to the C=O stretching mode of both the reactant and the solvent. Recently, Ebbesen and co-workers showed that the VSC could be used to modify the branching ratio of two competing reaction pathways in a molecule.¹¹⁷ Early on, Pang et al. found that VSC induces changes in the equilibrium constant on the charge transfer complexation of the trimethylated benzene with iodine, confirming modifications in the ΔG^0 of the reaction.¹¹⁸ Xiang et al. demonstrated that strong coupling between cavity modes and donor and acceptor molecules enhanced vibrational energy transfer between molecules in the liquid phase.¹¹⁹

To study the influence of the confined field of the microcavity on the vibrational energy levels molecules in a liquid state, we made use of an open infrared microcavity. VSC has been mostly achieved using a fixed thickness microcavity, for which the resonance condition can be attained by tilting the sample with respect to the light propagation direction.⁴⁶⁻⁴⁸ In this work, we designed a voltage-tunable microcavity, and we investigated multimode coupling – the hybridization of various vibrational transitions simultaneously with a single cavity mode – in methyl salicylate (MS). Our microcavity setting enables us to achieve the resonance condition without moving and/or rotating the sample and to control the parallelism of the cavity mirrors after assembly. Moreover, in order to explain the multimode VSC dynamics, a theoretical model was developed, based on a damped coupled harmonic oscillators model.

4.2. Open Microcavity Design and Characterization

Strong coupling of electromagnetic radiation with matter is typically realized by embedding molecules in an appropriate Fabry-Pérot microcavity made of two semi-transparent, typically metal-coated or Bragg mirrors. An open microcavity structure, which has one of the cavity mirrors mounted on a piezoelectric actuator, has the advantage of controlling the parallelism of the cavity mirrors after assembly along with a nearly unlimited tuning range.¹²⁰ In this work, we have used a piezo-based tunable Fabry-Pérot open microcavity, which can be readily employed to hybridize vibrational modes of a molecule with the vacuum modes of the cavity in a broad range of cavity mode orders.

The design of the open microcavity is shown in Figure 4.2. The cavity mirrors were prepared by sputtering a 10 nm thick Au layer on the CaF₂ window (for details, see Chapter 3). The open microcavity structure was obtained by placing the Au-coated CaF₂ substrates onto a piezo-actuated kinematic mirror mount (Thorlabs, KC1-PZ/M) and positioned at a well-defined distance away from each other using a home-built cavity holder. The cavity modes were tuned by applying a voltage on a piezoelectric element integrated into the upper mirror holder. The quality of the microcavity modes was checked by recording the transmission spectra of empty microcavities before each experiment. For a vibrational strong coupling study, the microcavity was filled through capillary action by depositing drops of MS dissolved in methylcyclohexane onto the edges of the CaF₂ windows with the use of a micropipette. The free space transmission spectra of MS, BN, and methylcyclohexane were obtained by injecting the solution between two uncoated CaF₂ windows.

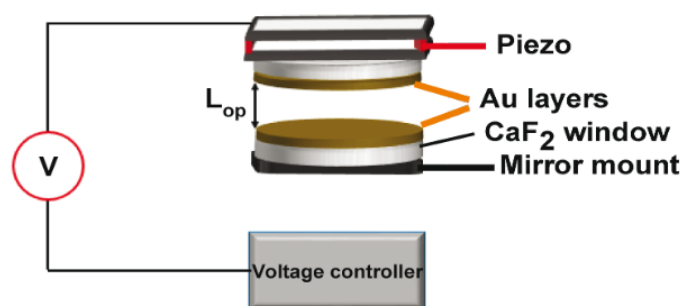


Figure 4.2. Schematic of the open microcavity structure employed to couple liquid phase samples. Adapted from ref. 114. Copyright (2020) American Chemical Society.

Figure 4.3a shows the transmission spectra of an empty microcavity as a function of the applied voltage. As shown from these plots, a voltage increment of 1 V leads to a 5 cm⁻¹ shift of the cavity mode. Microcavities with a Q-factor of 70–100 can be prepared, and depending on the concentration of the sample, the optical path length (L_{op}) – the separation between the mirrors – can be varied from 5 μm to 30 μm.

The FSR is the separation between two adjacent cavity modes, calculated by using the following formula:

$$FSR = \nu_{m+1} - \nu_m, \quad (4.1)$$

where ν_m is the resonance frequency of the cavity mode. The number of cavity modes (m) can be determined from the FSR using the following formula:¹²⁰

$$m = \frac{v_m}{FSR}. \quad (4.2)$$

The separation between the mirrors is calculated by using the following equation:

$$L_{op} = \frac{m}{2v_m}. \quad (4.3)$$

In our setting, the L_{op} of the cavity can be decreased to 5 μm , with a free spectral range (FRS) of about 1000 cm^{-1} (Figure 4.3b). The observed decrease in cavity transmission towards lower wavenumbers is due to the evolution of the dielectric constant of a metal film in this spectral region.⁴³ The microcavity employed in this work has the advantage of precise tuning of the cavity modes and can be employed for coupling any molecular vibration in the infrared region.

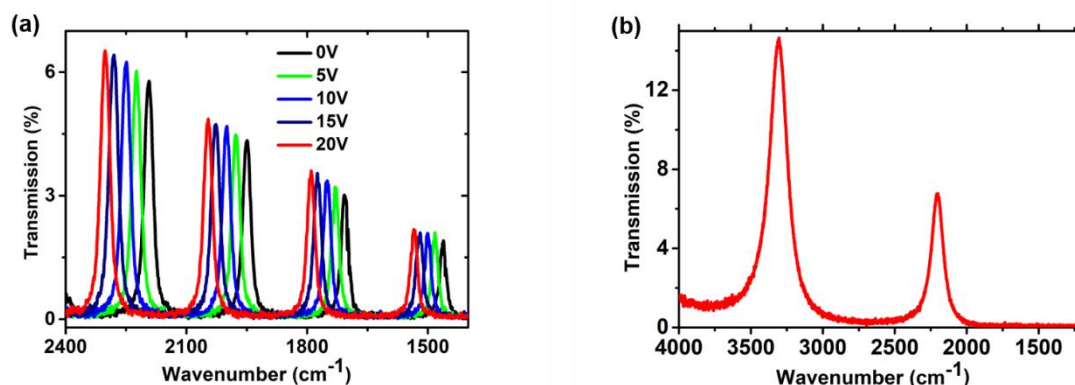


Figure 4.3. (a) Transmission spectrum of an empty open microcavity, obtained by varying the voltage applied to a piezoelectric element of the mirror holder. (b) The transmission spectrum of an empty microcavity with L_{op} of 5 μm .

4.3. Vibrational Strong Coupling in Methyl Salicylate

To investigate the effects of vibrational strong coupling on the infrared spectra of molecules in a liquid phase, we chose methyl salicylate (MS) as a model compound because of its intense C=O vibrational mode and narrow mode bandwidth of 16 cm^{-1} .

The comparison between the FTIR spectra of MS dissolved in methylcyclohexane (MCH), and pure MCH is shown in Figure 4.4. Most of the MS vibrational frequencies are isolated from the solvent vibrational peaks. The FTIR spectrum of MS has an intense and sharp C=O stretching frequency at 1685 cm^{-1} . The vibrations at 1585 cm^{-1} and 1616 cm^{-1} are due to the MS aromatic C=C vibrations.^{121,122} The vibrational peak assignments of MS are indicated

in Table 4.1, and all vibrational transitions are consistent with those reported in the literature. In principle, any vibrational transition in the mid-infrared region can easily couple with a cavity mode. However, most reports in the literature have demonstrated VSC phenomenon using polar functional groups such as carbonyl (C=O), cyanide (C≡N), amide (H₂N-C=O), and C≡O ligands, as these are vibrations with large optical absorptivity, usually isolated from the solvent and neighbouring vibrational peaks.⁴⁸

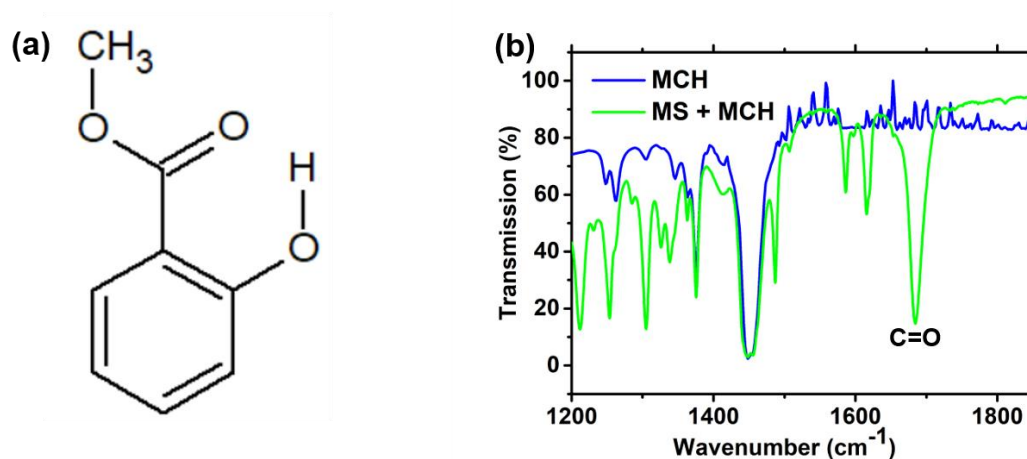


Figure 4.4. (a) Chemical structure of methyl salicylate (MS). (b) Comparison of FTIR transmission spectra of pure methylcyclohexane (MCH) and methyl salicylate (MS) dissolved in MCH.

Table 4.1: Vibrational frequency peak assignments for the FTIR MS.^{121,122}

Vibrational frequency (cm ⁻¹)	Vibrational assignments
3193	O-H symmetric stretching
1685	C=O symmetric stretching
1616	Phenyl stretching vibrations
1585	
1487	
1448	
1304	
1340	In-plane O-H deformation
1253	(C=O)-O stretching

In order to achieve VSC in MS, the microcavity mode was voltage-tuned toward the C=O vibrational frequency. When the cavity mode and the C=O vibrational frequency become isoenergetic, two new peaks at 1650 and 1710 cm⁻¹ are observed in the MS-filled microcavity transmission spectrum (Figure 4.5a, red curve). These are the new vibrational polaritonic states (VP⁻ and VP⁺) in MS. The separation between VP⁻ and VP⁺ states (60 cm⁻¹) – the Rabi splitting – is larger than the FWHM of both the C=O (16 cm⁻¹) and the cavity mode (30 cm⁻¹). This indicates that the interaction of the C=O transition and the cavity mode satisfies the strong coupling criteria.³¹ The transmission spectrum of the MS filled off-resonance cavity is shown in green in Figure 4.5a, and in this case, the strong coupling effect is not observed, however, a minute dispersive line shape is detected at the C=O vibrational transition of MS.

Figure 4.5b displays the effect of concentration on the Rabi splitting. The Rabi splitting strongly depends on the molecular concentration. As the concentration increases, the splitting between the VP⁺ and VP⁻ peaks becomes larger. For lowest concentrations, i.e., 0.05% v/v and 0.5% v/v, the spectral separation between the VP⁺ and VP⁻ states are smaller than the full width at half maximum of the cavity mode (Figure 4.5b), hence the coupled system is in the weak coupling regime. However, when we increase the concentration to 5% v/v of MS, the separation between the VP⁻ and VP⁺ peaks exceeds the bandwidth of the cavity. The concentration dependence result confirms that many molecules are interacting with a single cavity mode. This is possible because the volume occupied by the molecule is much smaller than the cavity mode volume.¹²³ The black crosses display the peak separation calculated with a harmonic oscillator approach, which is discussed below.

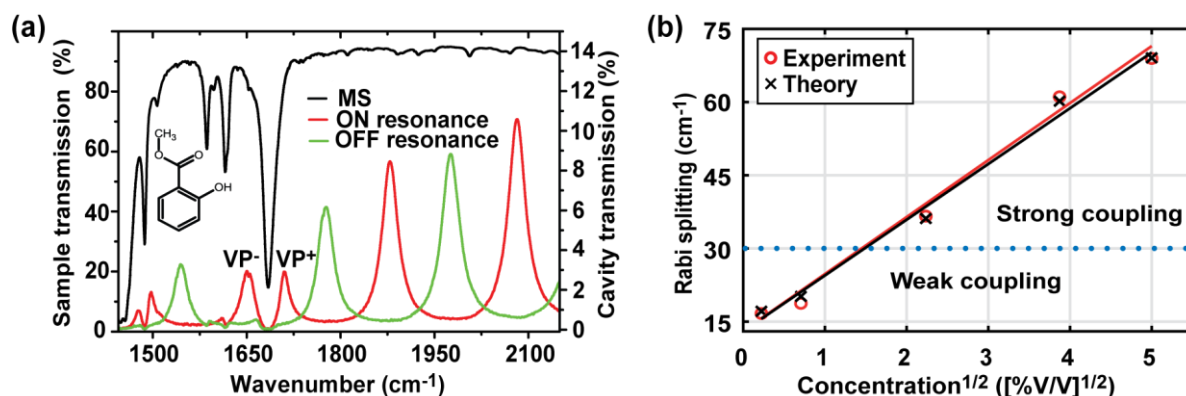


Figure 4.5. The FTIR spectrum of 15% v/v MS dissolved in MCH is shown in black. The transmission spectrum of MS solution in on and off-resonance cavity is shown in green and red, respectively. (b) The effect of concentration on the Rabi splitting of the C=O vibration of MS. The red circles and black crosses indicate the experimental and calculated values, respectively. The linear fits to the experimental and theoretical data are shown in solid red and black lines, respectively. The weak/strong coupling regimes threshold is indicated by the dotted line. Reprinted from ref. 114. Copyright (2020) American Chemical Society.

During VSC, a vibrational transition couples to a propagating photon in the cavity mode. Because of this, vibrational polaritons have a typical dispersion property that inherits from the photonic component.¹²⁴ To confirm this feature, the polariton dispersion as a function of the cavity tuning is plotted in Figure 4.6. At the resonance frequency, C=O vibration and the uncoupled cavity mode cross each other (marked by the two red lines), whereas the maxima of the VP⁺ and VP⁻ peaks avoid crossing, which also proves the realization of VSC in MS.

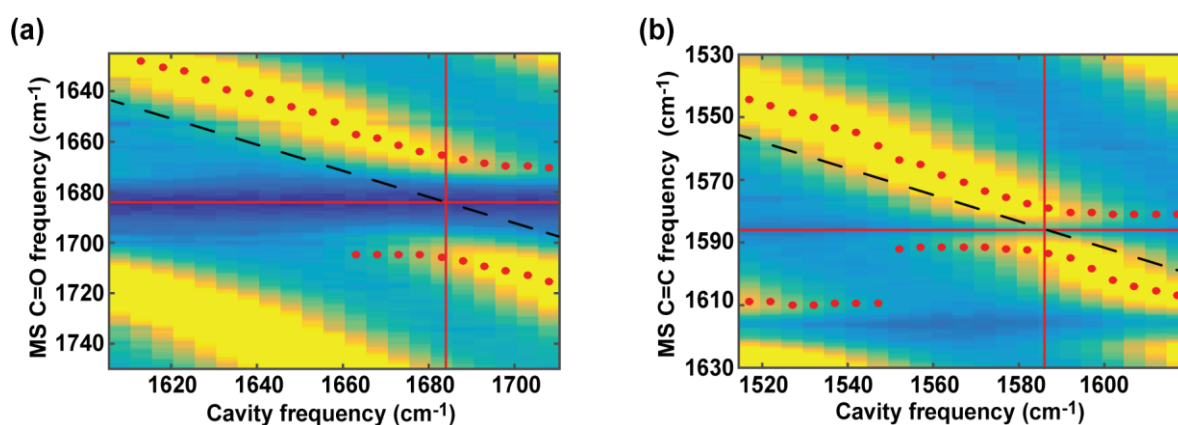


Figure 4.6. Anticrossing plots for the C=O (a) and C=C (b) vibrations of MS (5% v/v) hybridized to a microcavity. The dots show polaritonic peaks maxima. Solid red lines indicate resonant frequencies of the cavity and C=O and C=C stretching modes, while black dashed

lines indicate the cavity mode tuning, highlighting the anti-crossing character of the dispersion plot. Reprinted from ref. 114. Copyright (2020) American Chemical Society.

4.4. Theoretical Description of Multimode VSC

Coupled damped harmonic oscillators were used to describe multimode VSC in MS theoretically. The oscillator shown in Eqn. 4.4 was used to model the cavity mode, and the other three oscillators were employed to model the three different vibrational transitions of MS hybridized to the same cavity mode. The equations of motion of such a coupled oscillator system read:¹²⁵

$$\ddot{x}_1(t) + \gamma_1 \dot{x}_1(t) + \omega_1^2 x_1(t) + \kappa_2 x_2(t) + \kappa_3 x_3(t) + \kappa_4 x_4(t) = 0 \quad (4.4)$$

$$\ddot{x}_2(t) + \gamma_2 \dot{x}_2(t) + \omega_2^2 x_2(t) + \kappa_2 x_1(t) = 0 \quad (4.5)$$

$$\ddot{x}_3(t) + \gamma_3 \dot{x}_3(t) + \omega_3^2 x_3(t) + \kappa_3 x_1(t) = 0 \quad (4.6)$$

$$\ddot{x}_4(t) + \gamma_4 \dot{x}_4(t) + \omega_4^2 x_4(t) + \kappa_4 x_1(t) = 0 \quad (4.7)$$

where γ_1 , γ_2 , γ_3 , and γ_4 are the damping constants, ω_1 , ω_2 , ω_3 , and ω_4 are the resonance frequencies, and κ_2 , κ_3 , and κ_4 are the coupling constants. The cavity mode described by Eqn. 4.4 is coupled to vibrations represented by Eqn.s 4.5–4.7 through the terms proportional to κ , which allows a reversible energy exchange between the vibrations $x_{2-4}(t)$ and the cavity mode $x_1(t)$. The coupled differential equations were solved numerically to obtain the time evolution of the amplitudes $x_{1-4}(t)$, and the amplitudes were Fourier-transformed to obtain the transmission spectra. The Fourier transform of the time evolution of the cavity mode $x_1(t)$ is particularly interesting, as it can be probed experimentally; it is equivalent to the transmission spectrum of the coupled system.

The cavity and molecular damping constants were kept constant during all simulations. The cavity damping constant was obtained from the FWHM of the off-resonant cavity mode, while the molecular damping constant was calculated from the FWHM of the free space transmission spectra of MS. The parameters which were varied during the simulation are the coupling constants and the spectral position of the cavity mode. The parameters used to simulate the spectra of BN and MS are given in Tables 4.2 and 4.3, respectively.

Table 4.2. Parameters employed to simulate the spectra of benzonitrile shown in Figure 4.7.

	Frequency (cm ⁻¹)	γ (meV)	κ (meV)
Vibration 1	2229	1.2	2.3
Cavity 1	2227	2.0	-

First, we assessed the proposed theoretical model using benzonitrile (BN), as it has a well-isolated C \equiv N vibration. The experimental (red line) and simulated (black line) transmission spectra of BN filled microcavity is shown in Figure 4.7. The cavity modes are shown as the dashed blue vertical lines. The transmission spectrum of BN solution is shown as the green area. When the cavity mode is coupled with the C \equiv N stretching vibration at 2229 cm⁻¹, the splitting into the VP⁻ and VP⁺ states can be observed in the transmission spectrum (Figure 4.7a). The Rabi splitting is 50 cm⁻¹, which agrees with the value reported by George et al.⁴³ Figure 4.7b displays the experimental (red line) and simulated (black line) transmission spectra of an off-resonance cavity. Apart from a weak signature of coupling, the transmission spectrum is similar to that of an empty cavity. The experimental and simulated spectra match very well, indicating that the coupled harmonic oscillator is an appropriate approach to model VSC.

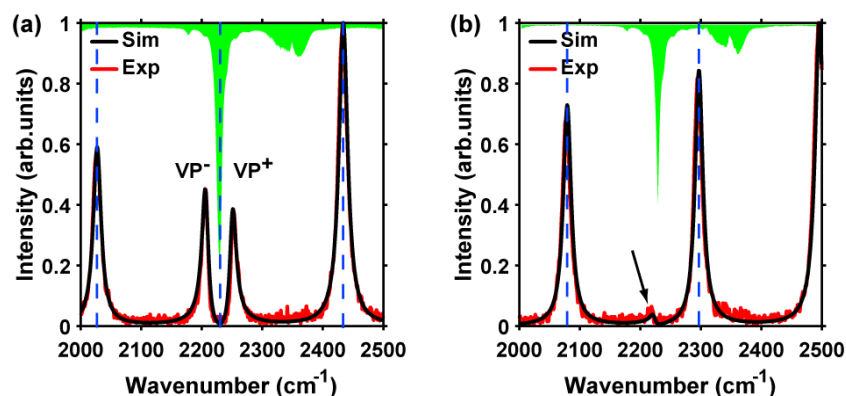


Figure 4.7. Experimental (red line) and simulated (black line) cavity transmission spectra of benzonitrile filled microcavity; in (a) the cavity is on-resonance with C \equiv N vibration, while it was off-resonance. The green area indicates the transmission spectrum of bare BN.

The experimental transmission spectrum of 25% v/v MS in an on-resonance cavity is presented in Figure 4.8a (red line). The transmission spectrum of the corresponding uncoupled MS is shown as the green area. The splitting is observed when one of the cavity modes is on-resonance to the C=O stretching (at 1685 cm⁻¹). Multiple vibrational coupling is observed due

to the presence of other cavity modes, e.g., at 1275 cm^{-1} and 1465 cm^{-1} . The blue vertical lines indicate the cavity modes. The experimental spectrum of another MS-filled cavity is shown in Figure 4.8b, where the cavity mode located at 1323 cm^{-1} couples to vibrations in this spectral range. Although the cavity modes at 1533 cm^{-1} and 1730 cm^{-1} are off-resonant to the C=O vibration, coupling with this vibration can be observed at 1685 cm^{-1} (indicated by the black arrow). Such patterns are observed for different vibrations, for instance, at 1458 cm^{-1} , 1616 cm^{-1} , and are identified by weak dispersive line shapes in the coupled system's transmission spectrum. Since MS has several vibrations that are spectrally close enough to couple with the same cavity mode, the interaction of the cavity modes with MS is more complex than for BN. In the following, we explore this multimode coupling behaviour in detail.

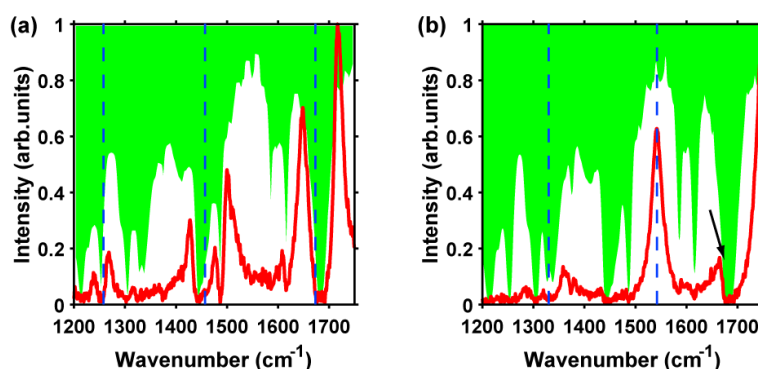


Figure 4.8. The experimental transmission spectrum of methyl salicylate (25% v/v) in an on-resonance (a) and an off-resonance cavity (b), red lines. The green area indicates the corresponding transmission spectrum of the MS solution.

Figure 4.9 shows the comparisons of the experimental transmission spectrum of 25% v/v of MS in the resonant cavity (red curve) and the calculated spectra (black curves). In the first case, we only considered the absorption of uncoupled molecules (Figure 4.9a); the hybridization of the cavity mode with MS molecular vibrations is switched off. Absorption has to be considered, as the number of uncoupled molecules is much larger than that of coupled molecules in the cavity volume.⁴⁸ This is realized by multiplying the calculated cavity transmission spectrum by the free space transmission spectrum of MS. Although there is no strong light-matter coupling, considering only absorption leads to a splitting of the originally Lorentzian shaped cavity transmission spectrum. Nevertheless, the intensity ratios of all peaks are not well reproduced, particularly the dip at 1685 cm^{-1} , and because of this, the mean square error (MSE), which is the measure of the fitting quality, is 28.7. Hence, considering only the absorption of uncoupled molecules is not enough to model the experimental spectrum. In the

second scenario (Figure 4.9b), we consider absorption and hybridization of MS vibrations individually to the cavity modes. We observe multimode coupling, but the peaks at 1465 cm^{-1} and 1685 cm^{-1} do not fit properly the experimental spectrum and need further treatment. However, the MSE decreases to 18.2.

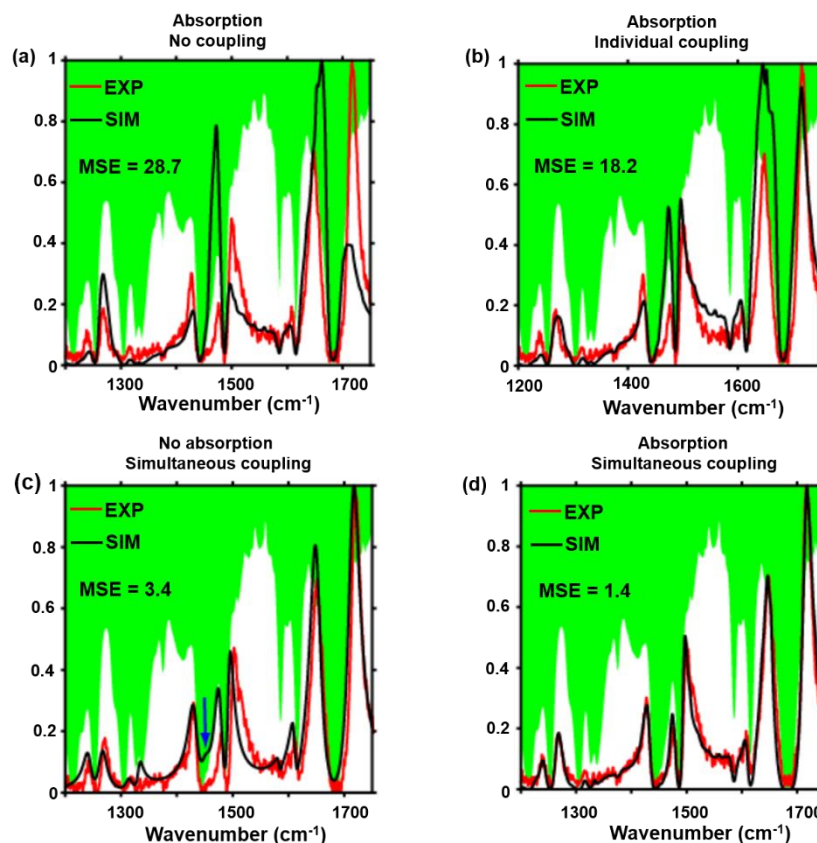


Figure 4.9. Experimental (red line) and calculated (black line) cavity transmission spectra for a 25% v/v solution of MS inside an on-resonant cavity. The green area shows the transmission spectrum of MS in free space. The mean square error (MSE) indicates the fit quality. In panel (a), only absorption is considered, while in (b), we take into account both absorption and individual coupling - the interaction of the vibrations that are only resonant with the respective cavity mode. Panel (c) demonstrates the case of multimode coupling - simultaneously coupling of the resonant and the closest two off-resonant molecular vibrations to the same cavity mode, and in this scenario, the absorption was excluded. The simulated spectrum shown in panel (d) was obtained by including both absorption and simultaneous coupling of the nearest MS vibrations to a single cavity mode.

The calculated spectra shown in Figure 4.9c and 4.9d are obtained by considering the influence of simultaneous coupling - the interaction of the closest two off-resonant molecular vibrations in addition to the resonance condition. In the former, the absorption of uncoupled

molecules was not considered. In the latter, we take into account both absorption and simultaneous coupling of the nearest MS vibrations to a single cavity mode. In both scenarios, the fitting between the experimental data and the calculated spectra improves a lot. However, the best match between the calculation and the experimental data was found in the last case, and the MSE decreases to 1.4 (Figure 4.9d). Hence, this confirms that absorption of uncoupled molecules must be considered and that we observe multimode hybridization of, at least, three molecular vibrations with the same cavity mode. The multimode coupling mainly affects the intensity of the peaks, whereas the Rabi splitting is less influenced.

Table 4.3. Parameters used to simulate spectra of methyl salicylate shown in Figure 4.9.

	Frequency	γ (meV)	κ (meV)
Vibration 1	1253	1.8	0.8
Vibration 2	1304	2.0	1.5
Vibration 3	1325	1.0	1.0
Cavity 1	1256	2.5	-
Vibration 4	1443	2.1	1.0
Vibration 5	1458	3.2	1.1
Vibration 6	1487	0.8	0.8
Cavity 2	1465	3.3	-
Vibration 7	1586	0.7	1.0
Vibration 8	1616	1.0	1.3
Vibration 9	1685	2.4	2.6
Cavity 3	1674	4.3	-

Finally, the experimental Rabi splitting was compared with the calculated values, which is presented in Figure 4.5b. The experimental Rabi splitting obtained from the peak separation between the VP^- and VP^+ states is indicated in red in Figure 4.5b. The peak separation between the vibrational polaritonic states obtained from the simulated spectra is shown in black crosses in Figure 4.5b and there is an excellent agreement between the experimental and calculated Rabi splitting values.

4.5. Conclusions

Strong coupling between IR-active molecular vibration and a vacuum field of a cavity mode results in the formation of vibrational polaritons. In the previous five years, vibrational strong coupling has been widely investigated because of its potential to modulate chemical dynamics and to influence spectral properties of molecules. Here, we realized multimode vibrational strong coupling in liquid phases using Fabry–Pérot type open microcavity. The hybridization of molecular vibrations with the cavity mode is described by a coupled damped harmonic oscillators model. The microcavity employed in this work can be fine-tuned to any molecular vibration, which makes it an appropriate tool for investigating molecular properties under vibrational strong coupling. Our theoretical model reveals that, in order to properly simulate the experimental spectra, one must consider the nearest off-resonance molecular vibrations in addition to the resonance condition. This indicates that cavity coupling can be occurring even for molecular vibrations that are off-resonant, but close to a cavity mode. The best fit between the experimental and calculated spectra was found when the influence of absorption of uncoupled molecules and the simultaneous coupling of close off-resonant molecular vibrations are considered.

5. Raman Scattering Under Vibrational Strong Coupling

This chapter is based on:

Takele, W. M.; Wackenhut, F.; Piatkowski, L.; Gawinkowski, S., Meixner, A. J.; Waluk, J. Scouting for Strong Light-Matter Coupling Signatures in Raman Spectra (Ready for Submission).

5.1. Introduction

Raman spectroscopy has become an excellent research tool due to its non-destructive nature, simple sample preparation, and microscopy capabilities.¹²⁶ It also has an advantage over IR spectroscopy, as a Raman signal is not significantly influenced by strongly IR absorbing solvents such as water or CO₂.¹²⁷ Since Raman scattering is an inherently inefficient process (~1 out of 10⁶ incident photons), detecting Raman signals from low concentration samples and single molecules is hard. Over the years, different Raman signal enhancement strategies have been proposed to overcome this limitation. The widely employed method is surface-enhanced Raman spectroscopy (SERS), which enhances Raman signal through molecules adsorbed on or near gold or silver nanostructures.¹²⁸ Huge Raman signal enhancement and better spatial resolution can also be achieved in tip-enhanced Raman spectroscopy by combining the sensitivity of SERS and the lateral resolution of scanning probe microscopy.¹²⁹ The Purcell Raman enhancement – the stimulating effect of vacuum fluctuations within a microcavity – has also been utilized to improve the Raman signal. This strategy is an analogy of fluorescence emission enhancement by weak light-matter coupling effect,¹³⁰ and it has been used to boost Raman scattering from various kinds of materials, such as organic molecules,¹³¹ carbon tubes,¹³⁰ and isotopic gas,¹³² to mention a few.

Another approach that has been suggested to improve Raman scattering efficiency is the strong light-matter coupling phenomenon. Polariton states formed by the hybridization between excitons and an optical microcavity¹³³ or surface plasmon¹³⁴ modes have been utilized to enhance the Raman signal. Maximum signal intensity is obtained when the polariton state becomes resonant with the Raman excitation energy. In 2015, Shalabney et al.¹³⁵ claimed three orders of magnitude increase of the Raman scattering cross-section when the C=O IR-vibration of polyvinyl acetate (PVAc) was strongly coupled with the optical mode of an IR-microcavity. They proposed that the coherent nature of the polaritonic states is responsible for the enhanced Raman cross-section. The concept of the Stokes Raman scattering under vibrational strong coupling is shown in Figure 5.1. In free space, the molecule in the virtual state decays into the

first excited vibrational state (green arrow). However, if the first excited vibrational state is coupled strongly with the cavity mode, the molecule in the virtual state may relax to either of the VP^+ or VP^- modes (black arrows in Figure 5.1). Here, we studied the possible effects of VSC on the Raman scattering properties of samples in the liquid phase and the solid polymer film.

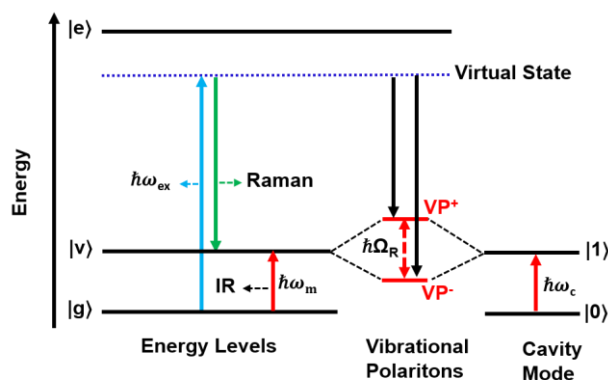


Figure 5.1. Raman scattering under vibrational strong coupling: When the IR-vibrational frequency of the molecule (ω_m) is strongly coupled with the cavity mode (ω_c), vibrational polaritons (VP^+ and VP^-) can be formed, and the system in the virtual state may decay to either VP^+ or VP^- states (black arrows).

5.2. Microcavity Preparations

In order to study the liquid samples under VSC, we employed the open microcavity setting that is described in Chapter 4. In this case, the microcavity mirrors were prepared from Ag films (10 nm). The structure of the microcavity and its transmission spectrum is shown in Figure 5.2.

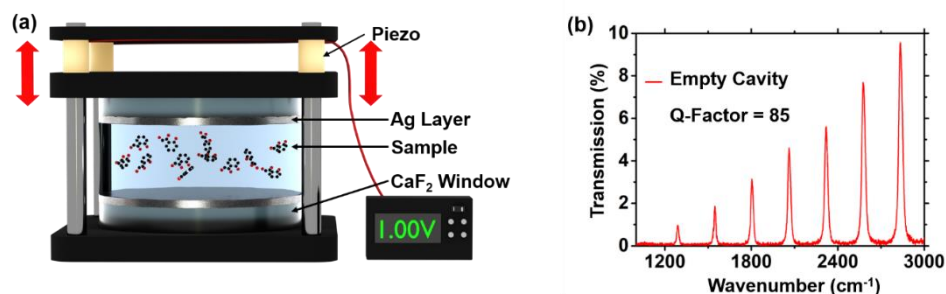


Figure 5.2. (a) The design of the microcavity used to study liquid samples. (b) Transmission spectrum of an empty microcavity with a Q-factor of 85.

The structures of various polymer-spaced microcavities used to investigate the Raman scattering properties of PVAc film under VSC are shown in Figure 5.3. The reference sample (configuration S1 in Figure 5.3) was prepared on a CaF₂ window by spin coating 15% w/w of PVAc solution dissolved in toluene at a speed of 870 rpm for 60 s. The details of the spin-coating condition and the PVAc solution preparation are described in the Methods section (Chapter 3). In order to prepare the polymer-spaced cavities, first, either 10 nm or 30 nm Ag (depending on the experiment) film was deposited on a CaF₂ window. Then, 15% w/w of PVAc solution was spin-coated at a speed of 870 rpm for 60 s. These spinning conditions give a PVAc layer of approximately 5 μm thickness and ensure that one of the cavity modes is on resonance with the PVAc C=O stretching vibration. The off-resonance cavity was prepared by spin-coating the same PVAc solution at a speed of 1000 rpm for a duration of 60 s. Finally, the optical microcavity was obtained when either 10 nm or 30 nm thick Ag film was sputtered on top of the PVAc film. Numerous ON and OFF resonance samples were made, and the preparation method is highly reproducible. In order to prepare the SERS sample, a few drops of silver nanoparticles (~100 nm size) colloid solution was cast on a clean CaF₂ window and left until dry. Finally, a PVAc solution was deposited on top of the SERS substrate using a micropipette and spin-coated at a speed of 870 rpm for a duration of 60 s.

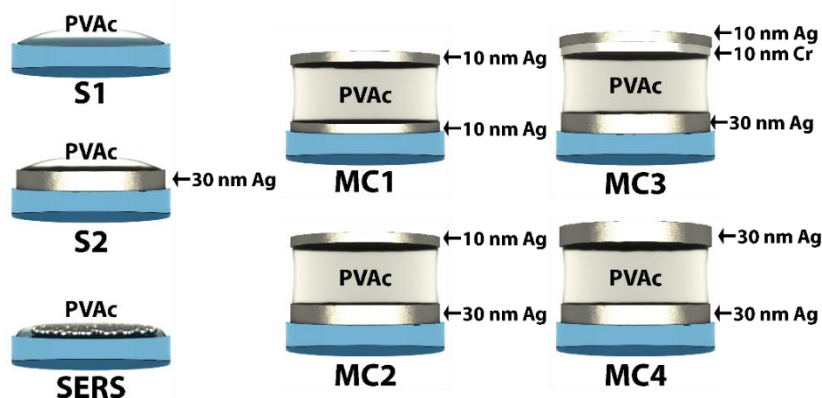


Figure 5.3. Schematic illustration of various samples used in this work; S1, S2, and SERS indicate a thin PVAc film deposited on CaF₂ window, 30 nm Ag film, and a SERS substrate, i.e., a few drops of silver nanoparticle solution cast on a clean CaF₂ window, respectively. MC1-MC4 illustrate different PVAc spaced microcavity configurations.

5.3. Raman Scattering Properties of Liquid Phase Samples Under Vibrational Strong Coupling

First, we investigated the Raman scattering characteristics of benzonitrile (BN) by coupling the C≡N IR vibration with the cavity mode. As described in section 4.4 of Chapter 4, vibrational polaritons were observed when the C≡N IR stretching frequency of BN was strongly coupled with one of the cavity modes. Here we studied the effect of the coupling on the Raman spectrum of BN (cyan curve in Figure 5.4a). Figure 5.4a shows the Raman spectra of BN inside the ON (blue) and OFF (red) resonance microcavity. Apart from a decrease in the background intensity, new peaks due to the formation of the vibrational polaritons were not observed in the Raman spectrum of the coupled system. This suggests that vibrational polaritonic states observed in the transmission spectrum (Figure 4.7a, Chapter 4) cannot be detected using Raman scattering measurements.

Next, we studied the effect of the multimode VSC in methyl salicylate (MS) described in Chapter 4 on the Raman spectrum properties of MS. Figure 5.4b (cyan curve) shows the Raman spectrum of the MS sample, obtained by injecting the solution in-between two CaF₂ windows, using the same structure as the cavity without the Ag films. The C=O vibration of MS is observed at 1670 cm⁻¹, which fully agreed with the value reported before.¹²² Figure 5.4b depicts the Raman spectra of MS (blue and red curves, respectively) acquired from the on- and the off-resonance cavities shown in Figure 4.5a of Chapter 4. Similar to the case of BN, no changes or formation of new spectral features were observed in the Raman spectra of the coupled system. The decrease in Raman signal intensity is due to the lower transmission of the semi-transparent cavity mirror. In order to confirm that the sample remains under strong coupling conditions, the transmission spectra of the coupled system were measured before and after acquiring the Raman spectra. Moreover, the cavity assembly was scanned in the focal plane to verify that the measured spectra remain unchanged irrespectively of the position probed with the laser.

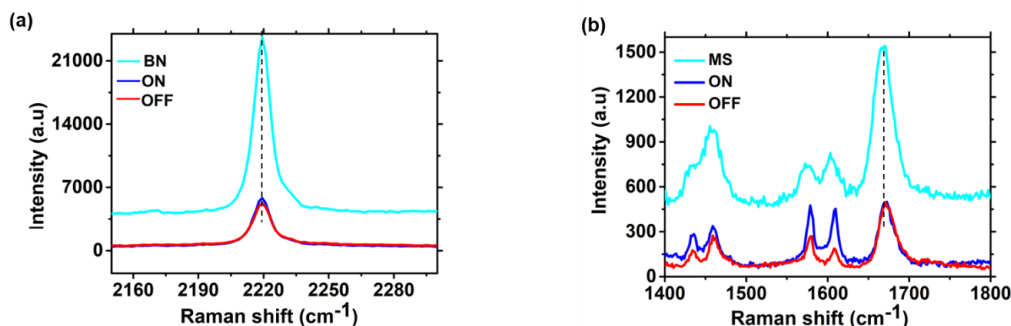


Figure 5.4. (a) Raman spectra of BN in free space (cyan) and obtained from the on- (blue) and off- resonance (red) cavities. (b) Raman spectra of MS in free space (cyan) and obtained from the on- (blue) and off-resonance (red) cavities.

5.4. Raman Scattering Characteristics of a Polymer Film Under Vibrational Strong Coupling

The liquid phase samples considered do not show the signatures of vibrational strong coupling in the Raman spectra, while they do clearly show them in the IR spectrum. The final system studied here is a PVAc film; the chemical structure of the polymer is shown in Figure 5.5a. Figure 5.5b (cyan curve) demonstrates the transmission spectrum of PVAc deposited on a CaF_2 window. The intense and sharp peak observed at 1740 cm^{-1} is due to the stretching frequency of the $\text{C}=\text{O}$ group. The transmission spectrum of the PVAc spaced cavity (configuration MC1 in Figure 5.3) did show two new peaks when the cavity mode is tuned to the $\text{C}=\text{O}$ vibration frequency PVAc (Figure 5.5b, blue curve). These are polaritonic peaks formed due to the VSC effect, and the separation between them is 150 cm^{-1} . For the off-resonance case, splitting due to the VSC was clearly not seen (the red curve in Figure 5.5b).

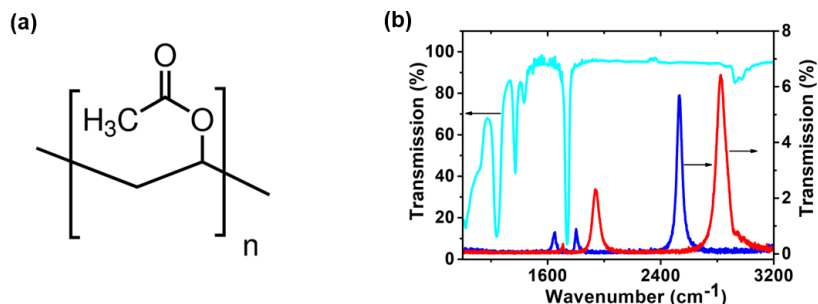


Figure 5.5. (a) Chemical structure of polyvinyl acetate (PVAc). (b) Transmission spectra of a PVAc film (S_1 sample type in Figure 5.3) (cyan) and embedded in an on- (blue) and off-resonance (red) optical microcavities configuration MC1 in Figure 5.3.

The cyan line in Figure 5.6a shows the Raman spectrum of PVAc on a bare CaF₂ window (configuration S₁ in Figure 5.3). The Raman peaks of PVAc are observed at 1023 cm⁻¹, 1375 cm⁻¹, 1440 cm⁻¹, and 1730 cm⁻¹. All Raman peaks are consistent with those reported in literature.¹³⁶ The Raman spectrum of the on-resonance PVAc spaced cavity (configuration MC1 in Figure 5.3) is shown in Figure 5.6a (blue curve). We have observed a similar spectra feature to those reported by Shalabney et al.,¹³⁵ specifically at around 1950 cm⁻¹ and 1600 cm⁻¹. The spectral features observed from the off-resonance sample (Figure 5.6a, red spectrum) are the same as for the on-resonance case. This indicates that the new spectral features observed in the Raman spectra of the cavity samples cannot be associated with the formation of polaritonic states. We measured the transmission spectrum of the PVAc spaced cavity after Raman measurement, Figure 5.6b (black curve). To reveal the origin of these peaks, we reproduced the experimental conditions used by Shalabney et al.¹³⁵ by changing the bottom cavity layer of MC1 to 30 nm Ag (cavity setting MC2 in Figure 5.3). The Raman spectrum characteristics (Figure 5.6a, olive curve) were the same as in cavity configuration MC1.

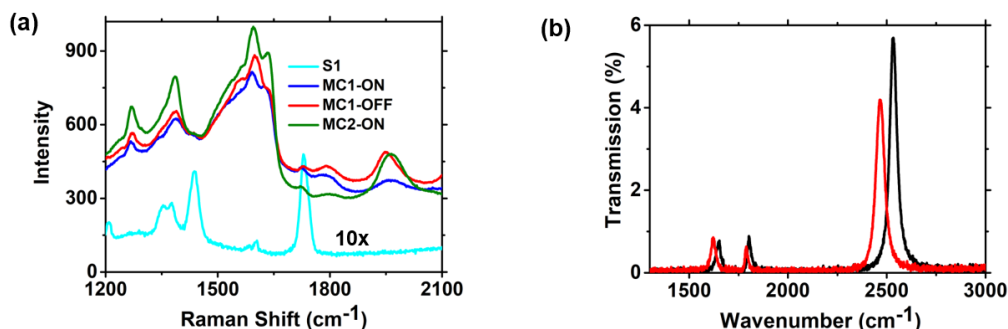


Figure 5.6. (a) Raman spectra of PVAc film (cyan, S₁ sample type in Figure 5.3) and embedded in an on- (blue) and off- (red) resonance optical microcavities (configuration MC1 in Figure 5.3) and configuration MC2. (b) Transmission spectrum of PVAc film embedded in an optical microcavity: Measured after Raman measurement, for the sample shown in configuration MC1 in Figure 5.3 (black curve); cavity transmission with C=O resonators of PVAc film when a thin Cr layer (10 nm) was used to separate the PVAc film from the top Ag layer, configuration MC3 in Figure 5.3, (red curve).

To confirm the effect of the Ag surface on the Raman spectrum of the PVAc film, we recorded various Raman spectra by employing different sample configurations shown in Figure 5.3 (S₂, MC3, and MC4). As shown in Figure 5.7a, Raman spectra obtained from PVAc spin-

coated on clean CaF₂ substrate (S₁) and a 30 nm thick layer of Ag (S₂) are identical. Hence, the surface of the 30 nm thick bottom Ag layer does not affect the Raman spectrum of the PVAc film. In configuration MC3, the direct contact between the PVAc film and the top Ag layer was prevented by depositing 10 nm Cr on the polymer film. Figure 5.6 (red curve) shows the transmission spectrum of this sample, and the result of this measurement confirmed that the Cr layer does not affect the coupling of the PVAc film with the cavity mode. The Raman spectrum of the PVAc film obtained using this configuration is presented in Figure 5.7a (black spectrum), and it is the same as the reference sample (Figure 5.7a, cyan curve). The spectrum of PVAc film obtained using 30 nm Ag as the top, and the bottom mirror (configuration MC4) also resembles the reference spectrum (Figure 5.7a, magenta spectrum). In this case, the Raman spectrum is much noisier because of the lower transmission of the cavity mirrors.

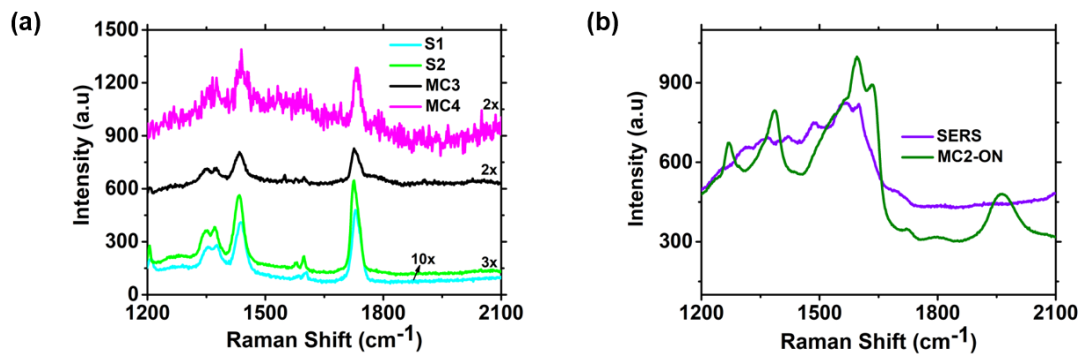


Figure 5.7. (a) Raman spectra of PVAc obtained with different sample configurations shown schematically in Figure 5.3 – for MC3 and MC4 the measurements were conducted under resonance condition. (b) Comparison of the SERS spectrum of PVA acquired using 100 nm spherical Ag nanoparticles as a substrate and the Raman spectrum obtained from configuration MC2 shown in Figure 5.3.

The measured Raman spectra for the cavity samples MC1/MC2 were significantly more intense than for the reference sample S1, suggesting that surface enhancement effects may play a role. To verify whether the features of the Raman spectra obtained from cavities MC1 and MC2 originate from surface enhancement effects, we measured SERS spectra of PVAc spin-coated on a surface made of a layer of Ag nanospheres. The SERS spectrum of PVAc (Figure 5.7b) is similar to cavity settings MC1 (on- and off-resonance cavities) and MC2. We characterized the surface roughness and nanometer-scale structure of the cavity mirrors used in our study using AFM (Figure 5.8).

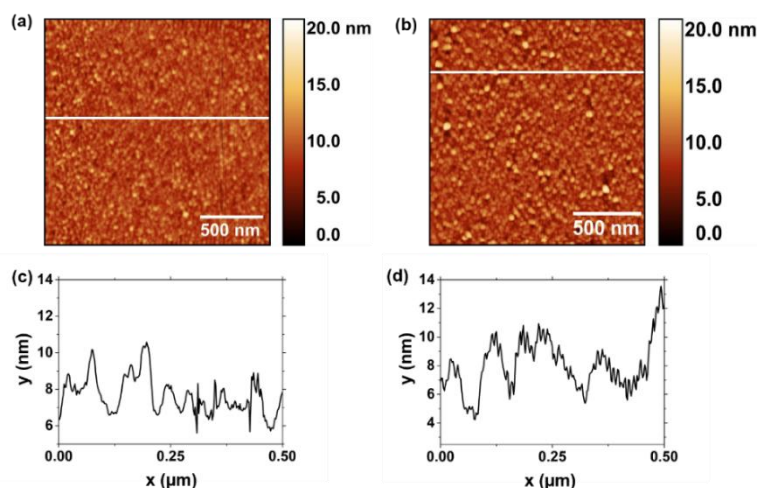


Figure 5.8 AFM images and height profiles of different Ag films sputtered on glass surfaces. (a) 10 nm Ag, (b) 30 nm Ag. Figures c and d show their respective height profiles. The RMS roughness of 1.33 nm and 1.78 nm are calculated for 10 nm Ag and 30 nm Ag, respectively.

Taylor et al.¹³⁶ reported the Raman spectrum of PVAc in free space; the Raman bands observed at 1023 cm^{-1} , 1375 cm^{-1} , 1440 cm^{-1} , and 1730 cm^{-1} were assigned to the CH_2 twisting, CH_3 asymmetric deformation, CH_2 asymmetric deformation, and $\text{C}=\text{O}$ stretching, respectively. All these vibrations were visible in our reference sample, but we also observed additional bands at 1580 cm^{-1} and 1604 cm^{-1} (Figure 5.9, curve b) in the reference sample. These peaks are most probably due to toluene molecules left in the PVAc film after evaporation, and the peak positions and features are consistent with the Raman spectrum of liquid toluene (Figure 5.9, curve c). The comparison of the Raman spectrum of PVAc film dissolved in toluene obtained using cavity setting MC2 and the SERS spectrum of toluene is presented in Figure 5.9, curves d and e, respectively. A fair agreement between the spectral features confirmed that the strong band observed at about 1600 cm^{-1} in our cavity samples is due to the SERS enhancement of toluene phenyl stretching vibrations. The significant Raman enhancement of this band at 1600 cm^{-1} in the SERS spectra of toluene is due to the surface selection rule for the enhancement effect.¹³⁷

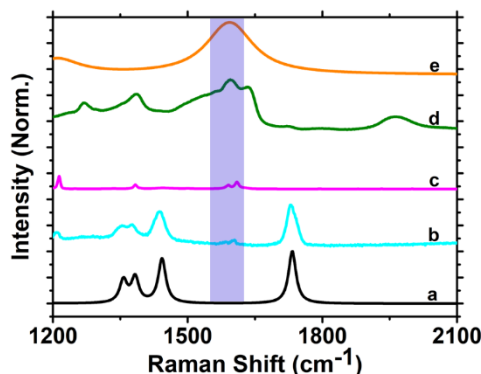


Figure 5.9. Comparison of Raman spectra of PVAc and toluene: (a) neat PVAc, (b) PVAc film dissolved in toluene, (c) liquid toluene, and (d) PVAc in MC2 cavity configuration shown in Figure 5.3. (e) SERS spectrum of liquid toluene.

Until now, to the best of our knowledge, only Shalabney et al.¹³⁵ claimed enhancement of the Raman signal under vibrational strong coupling, mostly two to three orders of magnitude enhancement from the VP^- mode. The authors claimed that the Raman signal is boosted due to an increase in the total Raman cross-section when the C=O vibration of the PVAc polymer film hybridized with the cavity mode. In contrast, the theoretical work of Pino et al.¹³⁸ suggested that the Raman cross-section is conserved during VSC, as long as ultrastrong VSC is not realized. They predicted that the induced change in the ground state by ultra-strong VSC could enhance Raman signal by less than a factor of two. They also showed that the Raman and IR bands in the coupled system should be located at the same energies. This is in contrast with the experimental work of Shalabney et al.,¹³⁵ where the separation between the polaritonic peaks obtained from the Raman data was about two times larger than the one obtained from the IR transmission spectrum. The theoretical work of Strashko and Keeling¹³⁹ also anticipated that a significant enhancement of Raman scattering is obtained under ultra-strong VSC.

On the other hand, many experimental works show an enhancement of the Raman signal by electronic strong coupling. For example, Tartakovskii et al.¹⁴⁰ reported an increase in Raman signal when the excitation energy of cyanine dye J aggregates and scattered photons are in resonance with the polaritonic states. Minamimoto et al.¹⁴¹ also demonstrated that electrochemically controlled strong coupling can be used to enhance Raman scattering spectra of molecules. In these and other works,^{142,143} neither polaritonic signatures nor a shift in the Raman peak positions have been observed in the Raman spectra of the coupled systems.

Finally, why the polaritonic states are not visible in the Raman spectra of the coupled systems, although they can be seen clearly in the FTIR transmission spectra? During an ensemble VSC, many molecules show up the same energy as those the free space sample, as described in section 2.6.2 of Chapter 2, these are the so-called dark states. Thus, in the Raman spectra of the coupled system, the dark states might dominate the transitions in the bright states (i.e., the polaritonic states), and because of this, we have observed only the Raman spectra of the uncoupled molecules in the cavity mode volume. From this, one can speculate that in the systems taken into account in our study, the fraction of the uncoupled molecules dominates those interacting with the cavity mode.

5.5. Conclusions

We studied the effect of vibrational strong coupling on the Raman scattering properties of molecules. Although the polaritonic peaks were observed in the transmission spectra of all the systems considered, they were not visible in the Raman spectra. For the PVAc film embedded in-between 10 nm Ag mirrors, two new peaks can be observed in the Raman spectra. These peaks have different properties compared to the VP^+ and VP^- states observed from the transmission spectrum of the PVAc film. First, the full width at half the maximum of these peaks is larger than the full width at half maximum of the polaritonic states observed from the FTIR measurements. Second, the separation between these peaks is unexpectedly large, two times larger than the Rabi splitting obtained from the transmission spectrum. Comparing the broad and strong peaks observed at about 1600 cm^{-1} with literature values, it is evident that they do not emerge from the polaritonic states but rather from the SERS enhancement of the phenyl vibrational peaks of the solvent toluene. The Raman spectrum acquired by separating the upper Ag mirror from the PVAc film by a thin Cr layer is similar to the PVAc film reference spectrum. This indisputably confirms that Raman scattering to the levels arising from vibrational strong coupling effect has not been observed. Nevertheless, one could ask whether the coupling effects may still be present, but their detection remains a challenge due to dominant scattering from uncoupled molecules.

6. Controlling the Photophysical Properties of Single Molecules by the Purcell Effect of an Optical Microcavity

This chapter is based on:

Takele, W. M.; Wackenhut, F.; Liu, Q.; Piatkowski, L.; Meixner, A. J.; Waluk, J. Tailoring Tautomerization of Single Phthalocyanine Molecules Through Modification of Chromophore Photophysics by the Purcell Effect of an Optical Microcavity (Submitted).

6.1. Introduction

The use of conventional ensemble spectroscopic methods has made a remarkable impact on our understanding of the physical and chemical properties of molecules. However, to fully understand the processes occurring at the molecular level, one must utilize single-molecule techniques. Single-molecule spectroscopy has allowed for the investigation of many photophysical, biological, and photochemical processes that are hidden by averaging during ensemble measurements.^{144,145} Some of the phenomena that have been investigated include fluorescence intermittency,¹⁴⁶ protein folding,¹⁴⁷ and photon antibunching.¹⁰⁷ Moreover, single fluorophores have been utilized for analyte sensing,¹⁴⁸ generation of single-photon sources,¹⁴⁹ and high-resolution optical imaging.¹⁵⁰ Incorporating single molecules as active components in electronics is also a promising approach for the next generation of miniaturization of electronic devices.¹⁵¹

For most single-molecule based applications, an ideal fluorophore should survive long (slow photobleaching), not show a random fluctuation of fluorescence intensity, and give a bright emission.^{152,153} In practice, however, it is hard to find fluorophores that exhibit all of these requirements. For optical probing of individual fluorescent molecules, visible light (typically a laser) has been employed. However, there is a fundamental size difference between a single emitter ($d \sim 1 \text{ nm}$) and visible light ($\lambda \sim 500 \text{ nm}$).³⁹ Besides, at ambient temperature, the absorption cross-section of a single-molecule is often small.¹⁵⁴ This fundamental size mismatch influences the photon absorbing probability of single quantum emitters and simultaneously lowers the spontaneous emission rate. Another inherent problem of single-molecules is their limited photostability; thus, we need to achieve brightness by keeping the excitation power low. Accordingly, considerable efforts have been devoted to enhancing the fluorescence signal and the photostability of single-molecules. One “physical” approach to address these challenges is microcavity-controlled fluorescence.

As described in the theory section, weak light-matter coupling (Section 2.4 of Chapter 2) enhances the spontaneous emission rate by changing the available local density of states for light emission (the Purcell effect). Plasmonic Purcell enhancement has been widely employed to control the photobleaching and blinking of single molecules. For instance, Cang et al. reported the suppression of photobleaching and prolonged lifespan of single molecules by the Purcell enhancement in plasmonic nanostructures.¹⁵⁵ Wientjes et al. showed a huge fluorescence enhancement of light-harvesting complex by coupling single molecules to a gold nanoantenna.¹⁵⁶ Stefani et al. demonstrated the decrease in blinking dynamics of a single fluorophore in the presence of a nearby gold film.¹⁵⁷ In general, lowering the triplet formation efficiency - by decreasing the lifetime of the singlet excited state *via* the Purcell effect - should result in higher photostability since there is less chance for the excited molecule to interact with the atmospheric oxygen.¹⁵⁵ Here, we investigate the influence of the confined optical fields in $\lambda/2$ -microcavity on the blinking dynamics and photostability of single phthalocyanine tetrasulfonate (PcS₄) molecules (Figure 6.1a).

Phthalocyanines (Pcs) are macrocyclic molecules with π -electron conjugation similar to that of hemes in biological systems and first synthesized by accident in 1907. Pcs have attractive electronic properties, unique thermal and chemical stability, and support intense electromagnetic radiation.¹⁵⁸ Because of these, Pc derivatives have found practical applications in organic solar cells,¹⁵⁹ catalysis,¹⁶⁰ and photodynamic therapy,¹⁶¹ to mention a few. Pcs are synthetic analogues of porphyrins, and they have intense $\pi \rightarrow \pi^*$ transitions (Q-bands) and larger fluorescence quantum yields compared to porphyrin derivatives. These properties make Pc derivatives a better choice for single-molecule spectroscopy studies.¹⁶² Pc derivatives are extensively studied at the single-molecule level using scanning tunneling microscopy.^{163,164} In this work, the single-molecule properties of PcS₄ are studied employing confocal laser scanning microscopy.

The absorption spectrum of PcS₄ in water (10^{-6} M) is presented in Figure 6.1b. There are two strong broad bands: the Soret band in the near-UV ($\lambda_{max}= 332$ nm) and the Q-band at 630 nm. PcS₄ exhibits a deep-red emission peak at 700 nm, which is shown in Figure 6.3 (black curve) for a PcS₄-PVA film. The absorption peaks agree well with previously reported values.¹⁶⁵

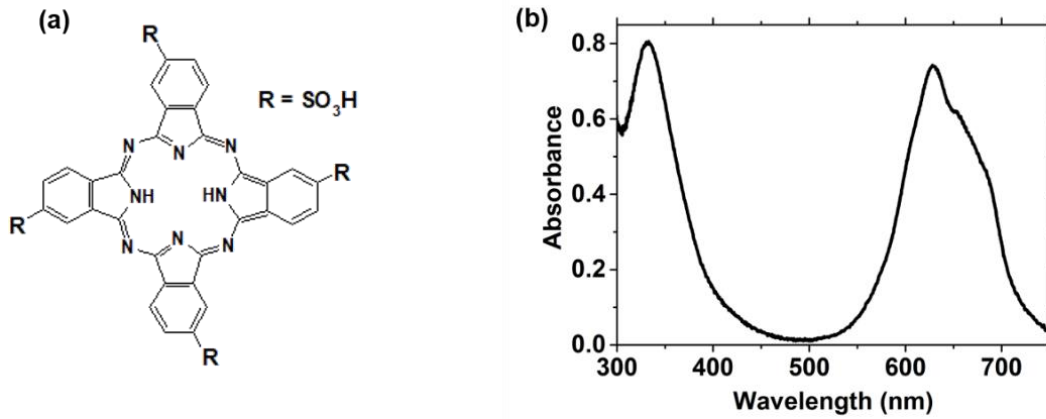


Figure 6.1. (a) The chemical structure of phthalocyanine tetrasulfonate (PcS₄). (b) Absorption spectrum of PcS₄ (10⁻⁶ M) dissolved in water.

6.2. $\lambda/2$ -Microcavity Preparation and Characterization

Figure 6.2 shows the schematic illustration of the optical microcavity used in these experiments together with a simplified sketch of the confocal microscope setup. It consists of two opposed silver mirrors with single PcS₄ molecules embedded in a PVA matrix placed in-between them.¹⁶⁶ The bottom mirror was prepared by sequentially evaporating 0.5 nm Cr, 30 nm Ag, and 70 nm SiO₂ layers on a clean microscope coverslip, while the upper cavity mirror was prepared on a convex lens by covering it with 0.5 nm Cr, 60 nm Ag, and 70 nm SiO₂ layers, consecutively. The Cr layer was used for adhesion, while the SiO₂ layer prevented the contact between the embedded dye molecules and the Ag film. The optical microcavity structure is assembled by gluing the lower and the upper mirror onto a home-built mirror holder. A piezo-actuator kinematic mirror mount (KC1-PZ/M, Thorlabs) was used to tune the cavity length by moving the upper mirror relative to the fixed bottom mirror.

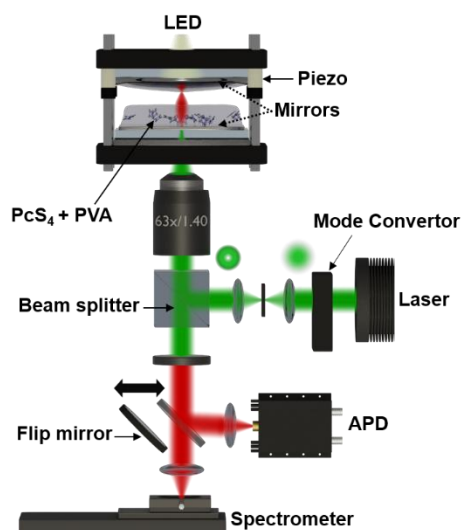


Figure 6.2. Schematic illustration of the piezo-tunable microcavity along with a simplified confocal microscopy setup.

To realize a strong radiative emission via the Purcell effect, one must control the reflectivity and the thickness of the cavity. The higher the reflectivity and the smaller optical separation between the mirrors, the faster is the radiative emission rate due to the cavity effect.¹⁶⁷ Thus, for all measurements, the optical path length of the cavity was adjusted to be in the first cavity order ($L_{op} = \lambda/2$). The transmission spectrum of the microcavity was acquired by illuminating from above with a white-light LED. A sample transmission spectrum with a Q-factor of 50 is shown in Figure 6.3 (red curve). Previous studies demonstrated that such a relatively low Q-factor microcavity is sufficient to modulate the fluorescence emission properties of single quantum emitters *via* the Purcell effect.^{166,168} The transmission can be voltage-tuned towards the fluorescence emission maximum of PcS₄ (black curve in Figure 6.3).

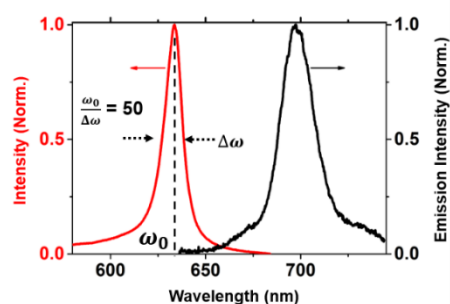


Figure 6.3. Exemplary microcavity transmission spectrum with a Q-factor of 50 (red) and the free space ensemble emission spectrum of a PcS₄-PVA film (black).

6.3. Single-Molecule Detection in the Free Space and Inside a $\lambda/2$ -Microcavity

We first studied the single-molecule properties of PcS₄ molecules in free space. The samples were prepared by spin coating PcS₄-PVA solution on a clean glass surface, and a home-built confocal microscope was used for the observation of single-molecule emission. Figure 6.4a shows a representative fluorescence image obtained using a 633 nm laser (Gaussian mode). The well-separated bright diffraction-limited spots are attributed to the fluorescence emission of single PcS₄ molecules. Once a single molecule is in the excited state, it stays there for a finite time, which is on average equal to the fluorescence lifetime of the molecule, when triplet population is negligible, before it relaxes back to the ground state and can be excited again. As a result, only one photon can be detected from the same molecule at a specific time. This temporal separation between two subsequent photon emissions from the same molecule is called photon antibunching, and it has been used to prove whether a single emitter is present in the sample.¹⁶⁹

Photon antibunching data can be obtained with continuous wave (CW) or pulsed laser excitation. Figure 6.4b (black trace) shows the measured second-order photon correlation function obtained upon CW excitation from the bright spot indicated by the white arrow in Figure 6.4a. The clear photon antibunching dip with $g^{(2)}(\tau) = 0.35$ proves that the emission is from a single PcS₄ molecule. The photon antibunching result obtained under pulsed excitation for another single PcS₄ molecule is shown in red in Figure 6.4b. In this case, the pulse at the lag time of zero is missing, which is a characteristic feature of single-molecule antibunching upon pulsed excitation.^{169,170}

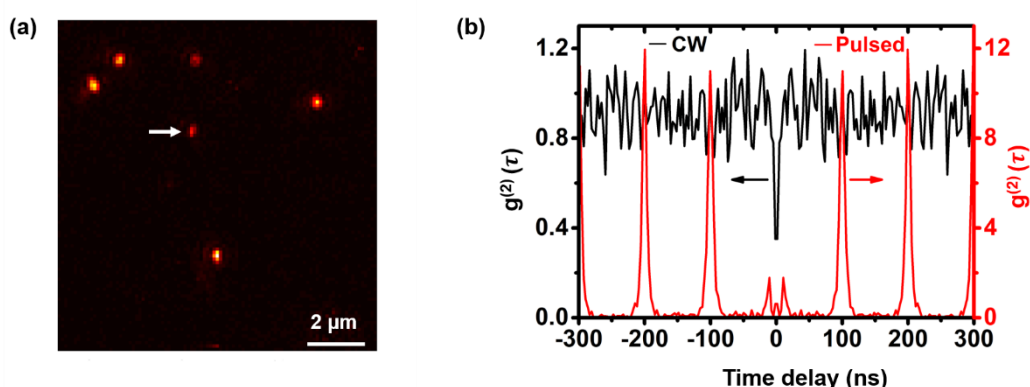


Figure 6.4. (a) Confocal microscopy image of single PcS₄ molecules embedded in PVA film. (b) Single PcS₄ molecule photon antibunching: the black curve shows the second order correlation function $g^{(2)}(\tau)$ measured from the single PcS₄ molecule indicated by the white

arrow in Figure 6.4a, under continuous wave (633 nm laser) excitation and using the pulsed laser (640 nm) excitation (red trace).

Figure 6.5a presents a single-molecule fluorescence image obtained by raster scanning the PcS₄-PVA film inside the microcavity through the excitation focus. In $\lambda/2$ -microcavity, the emission occurs only in a ring where the molecular fluorescence matches the resonance condition of the microcavity.^{166,168} The antibunching data obtained from the PcS₄ molecules inside a microcavity confirm that individual emitters are observed (Figure 6.5b).

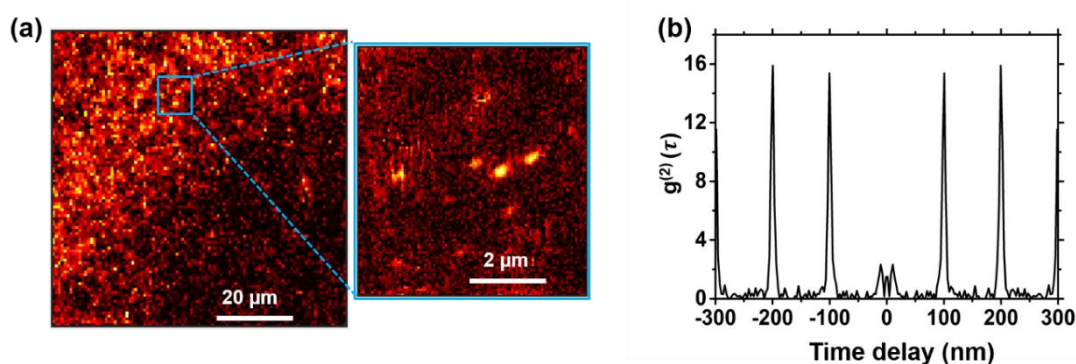


Figure 6.5. (a) Scanning confocal fluorescence microscopy image of the first-order interference region of the microcavity with individual PcS₄ molecules embedded in a PVA film appearing as bright spots. (b) Photon antibunching measured for the single PcS₄ molecule in a resonance cavity, using the pulsed laser (640 nm) excitation.

6.4. Photophysical Properties Under the Purcell Effect

The fluorescence lifetime, the blinking dynamics, and photostability of individual molecules were studied by placing PcS₄ molecules embedded in PVA film inside a resonant $\lambda/2$ -microcavity. Figure 6.6 schematically demonstrates the effect of the confined optical field in a microcavity on the photophysical processes of single emitters. The electronic and vibrational energy levels of the molecule are represented by the solid and dashed horizontal blue lines, respectively. In the fluorescence imaging experiments, single molecules are excited from the lowest vibrational level of the electronic ground state (S_0) into a higher vibrational energy level of the first electronically excited state (S_1). We assume that the excited molecule obeys Kasha's rule to return back to the ground state S_0 , which requires that the molecule decays from the lowest vibrational level of the first excited state.¹⁷¹ Hence, fluorescence

emission, internal conversion, and intersystem crossing always occur from this level. Kasha's rule is valid when vibrational relaxation via energy transfer to the environment is much faster than the depopulation of S_1 . The radiative decay into a vibrational level of S_0 , associated with the emission of a fluorescence photon, is indicated by a black downward arrow and the rate constant k_f . It is this rate constant, which can be tuned by varying the LDOS in the microcavity. Alternatively, the molecule can decay non-radiatively by transferring its energy as heat to the environment, k_{nr} , this process is independent of the LDOS.⁸⁶

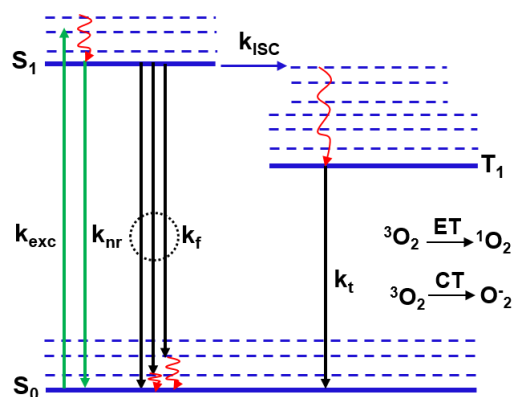


Figure 6.6. A simplified three-level scheme showing the influence of an optical microcavity on emission and the switching of a single molecule between fluorescent (ON) and dark (OFF) states and photobleaching. k_{exc} , k_f and k_{isc} , k_t refer to the rate constants for the excitation, fluorescence, S_1 - T_1 intersystem crossing, and triplet decay rates.

There is also a possibility that the molecule undergoes intersystem crossing from S_1 to the long-lived triplet state T_1 , which gives rise to non-emissive dark (OFF) states. This can cause either intermittent fluorescence emission (blinking) or permanent damage of the fluorophore (photobleaching) due to the reactivity of the triplet state with atmospheric triplet oxygen (3O_2), which leads to the formation of highly unstable species such as the singlet oxygen (1O_2) and the superoxide radical (O_2^-) through energy (ET) and charge transfer (CT) mechanisms, respectively (Figure 6.6).^{171,172} When the cavity is tuned on resonance with the fluorescence maximum, a shortening of the S_1 excited state lifetime *via* the Purcell effect occurs, which as a consequence decreases the triplet formation efficiency. Hence, the probability of photobleaching and the intramolecular proton transfer reaction that may occur in the excited states should be lower. In the following, we shall describe only the former, and the latter shall be discussed in Chapter 7.

Figure 6.7a presents the exemplary time-correlated single-photon counting histograms of single PcS₄ molecules embedded in PVA in free space (blue) and inside a resonant microcavity (green). The black trace shows the instrument response function (IRF), and it was employed for the single exponential deconvolution fitting to calculate the fluorescence lifetimes; we obtained fluorescence lifetimes of 3.58 ns and 2.31 ns for molecules embedded in PVA in free space (blue) and inside a resonant microcavity (green), respectively. Figure 6.7b shows a corresponding fluorescence lifetime distribution histogram for n = 74 single molecules embedded in PVA in free space and n = 68 single molecules inside the microcavity. An average lifetime of 3.56 ± 1.01 ns is obtained for molecules embedded in PVA in free space and 2.25 ± 0.43 ns inside a resonant cavity. Hence, the cavity enhances the spontaneous emission rate of the ON state.

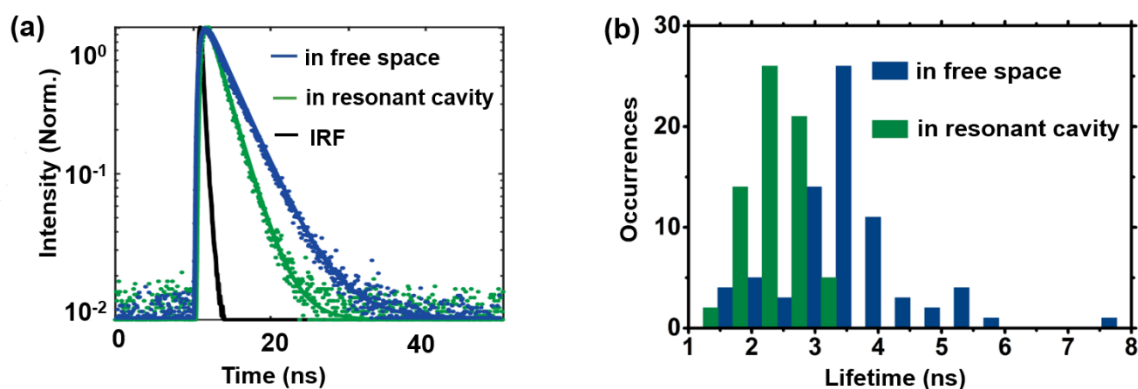


Figure 6.7. (a) Time-correlated single-photon counting decay traces of single PcS₄ molecules embedded in PVA in free space (blue trace) and inside the microcavity (green trace). The blue and green curves are single exponential fits to the fluorescence decays of the single molecules embedded in PVA in free space and inside a resonant microcavity together with the IRF (black). (b) Lifetime histograms of single PcS₄ molecules in free space (n = 74) and in the resonant microcavity (n = 68).

To investigate the influence of the confined optical fields of a microcavity on the blinking dynamics and the photostability of single PcS₄ molecules, we recorded fluorescence time traces. Figure 6.8a-b shows exemplary fluorescence intensity time traces of single PcS₄ molecules (the binning time for both measurements was 10 ms). For molecules embedded in PVA in free space, the ON and OFF states appear with several long OFF time periods (black rectangle in Figure 6.8a). In contrast, in the case of molecules placed in a resonant cavity OFF states are not observed for extended periods (Figure 6.8b). This indicates that the microcavity

influences the blinking dynamics of individual molecules. We described this observation by calculating the ON-ratio K_{on} , which is a measure of the blinking dynamics, from the intensity time traces by $K_{\text{on}} = \left(\frac{t_{\text{on}}}{t_{\text{on}} + t_{\text{off}}} \right) \cdot 100$.¹⁷³ t_{on} and t_{off} are times when the molecules are in the bright and dark states, respectively. t_{on} and t_{off} are obtained from the fluorescence intensity time traces by defining a threshold – of twice the background signal for a molecule that is in the bright state – indicated by the black dashed lines in Figure 6.8a-b.

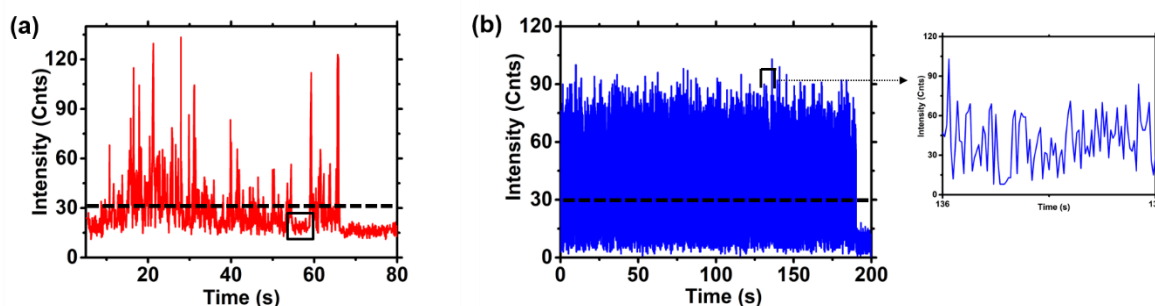


Figure 6.8. Single-molecule properties of PcS₄. (a) Fluorescence intensity time trace of a single PcS₄ molecule embedded in a thin PVA film. (b) Fluorescence intensity time trace of a single PcS₄ molecule embedded in the PVA matrix and placed inside the resonant microcavity.

The ON-ratio histogram obtained by calculating K_{on} from n molecules embedded in the PVA matrix in free space ($n = 102$) and placed inside a resonant cavity ($n = 102$) is shown in Figure 6.9a. For the PcS₄ molecules in free space the average ON-ratio is 23%, while for the molecules placed inside the resonant microcavity the average ON-ratio increases to 36%. This confirms that the microcavity reduces the OFF-periods of single molecule emission by decreasing the residence time of the molecule in the S₁ state.

Finally, we investigated the influence of the microcavity on the photobleaching behaviour of single PcS₄ molecules. As shown in the representative time traces in Figure 6.8, this particular PcS₄ molecule placed inside a resonant cavity had a longer survival time compared to the molecule in free-space. In this context, the survival time means the total time before a single molecule undergoes irreversible photobleaching. Figure 6.9b presents the survival time distributions for single PcS₄ molecules embedded in PVA in free space ($n = 102$) and placed inside a microcavity ($n = 102$). Mean survival times of 60.1 s and 131.8 s are obtained for the molecules embedded in the PVA matrix in free space and in the resonant cavity, respectively, by fitting the histograms with single exponential decay functions. Thus, reducing the lifetime by the Purcell effect of the microcavity improves the photostability of the

single PcS₄ molecules. Similar single-molecule fluorescence behaviour has been observed for other organic dyes placed in the vicinity of noble metal nanoparticles. For instance, Fu et al. demonstrated that the average bleaching time of single Cy5 molecules coupled to silver nanoparticles improved significantly, compared to molecules immobilized on a glass substrate.¹⁷⁴

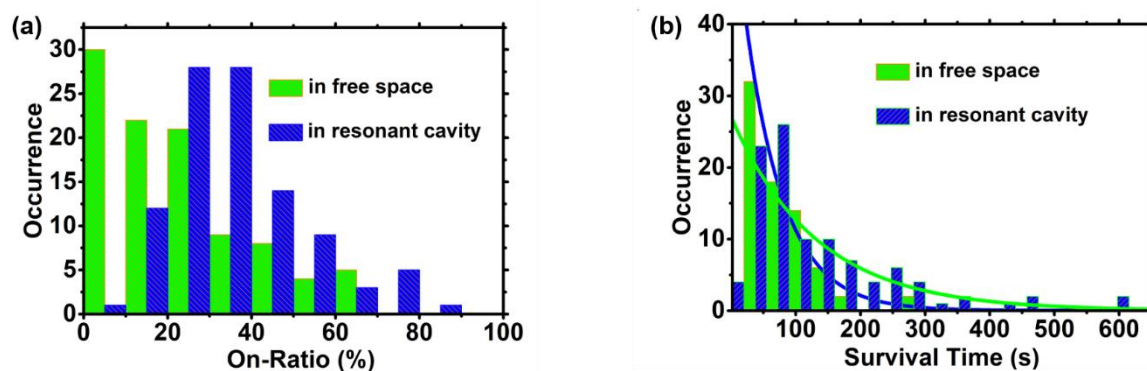


Figure 6.9. (a) On-ratio histogram of single PcS₄ molecules in free space and inside the resonant microcavity. (b) Histogram of the survival times of single PcS₄ molecules; the green and blue lines indicate exponential fits to the histograms obtained from molecules in free space and placed inside a microcavity, respectively.

6.5. Conclusions

The use of single molecules in chemical, biophysical, and quantum optics applications continues to increase. However, their applications are hindered because of photobleaching and stochastic blinking of individual fluorophores. Here, we demonstrate that the confined optical fields in a microcavity can be used to control the blinking dynamics and the photostability of single molecules. Decreasing the lifetime of the singlet excited state by the Purcell effect significantly reduces transitions of individual molecules to the non-fluorescent triplet state. Because of this, we have recorded more than two-fold increase in the photostability of single molecules. This reveals that the weak coupling between a cavity mode and a molecular transition can be used to control the damage of an excited molecule.

7. Tailoring the Tautomerization Properties of Single Phthalocyanine Molecules by the Vacuum Electromagnetic Field of an Optical Microcavity

This chapter is based on:

Takele, W. M.; Wackenhut, F.; Liu, Q.; Piatkowski, L.; Meixner, A. J.; Waluk, J. Tailoring Tautomerization of Single Phthalocyanine Molecules Through Modification of Chromophore Photophysics by the Purcell Effect of an Optical Microcavity (Submitted).

7.1. Introduction

Tautomerization, the addition of a proton at one molecular site and its removal from another, is a fundamental phenomenon in nature,¹⁷⁵ and it plays a significant role in DNA mutation,¹⁷⁶ chemical,¹⁷⁷ and enzymatic reactions.¹⁷⁸ Phthalocyanine and porphyrin derivatives contain two hydrogen atoms in the inner part of their structures. The migration of these protons in the framework of four nitrogen atoms is known as NH tautomerization. Over the decades, NH tautomerization has been studied extensively to understand the reaction mechanisms¹⁷⁹⁻¹⁸¹ and explore its technological applications.^{182,183} During NH tautomerization in porphyrin and phthalocyanine, the switching happens without a significant conformational change. It has been proposed to use this intriguing property in the emerging field of single molecules based “hardware” elements such as molecular switches¹⁸³ and photonic molecular wires.¹⁸⁴

Two types of mechanisms are known for the NH tautomerization process, i.e., concerted and stepwise. In the former, the two protons move synchronously, while the characteristic feature of the latter is *trans-cis-trans* conversion. In the stepwise mechanism, the tautomerization occurs by consecutive migration of the two protons one after another.^{180,181} After many years of research,¹⁸⁵⁻¹⁸⁸ it is now established that the double proton transfer process in porphyrin occurs by the stepwise mechanism. The *trans*-tautomer is more stable than the intermediate *cis*-tautomer. The tautomerization occurs in the ground electronic state on the time scale of tens of microseconds at room temperature. The *trans-cis* conversion involves tunneling from an excited vibrational level (Figure 7.1), which can be populated by thermal activation.¹⁸⁶

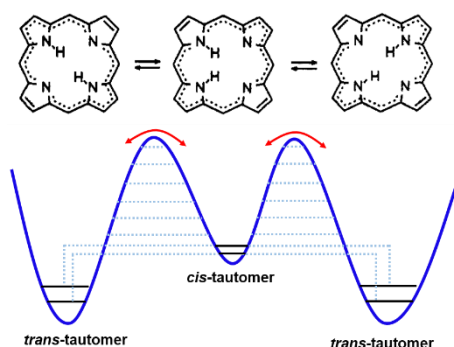


Figure 7.1. Tunneling mechanism for the stepwise NH tautomerization of porphyrin. Modified from ref. 186.

Phthalocyanines are structurally similar to porphyrins. Thus, one might expect similar tautomerization mechanisms. Strenalyuk et al. studied the structure and tautomerization mechanism of phthalocyanine. Their results showed that the *trans*-tautomer is 41.6 kJ/mol more stable than the *cis*-tautomer, and the stepwise NH tautomerization mechanism is preferable for phthalocyanine.¹⁸¹

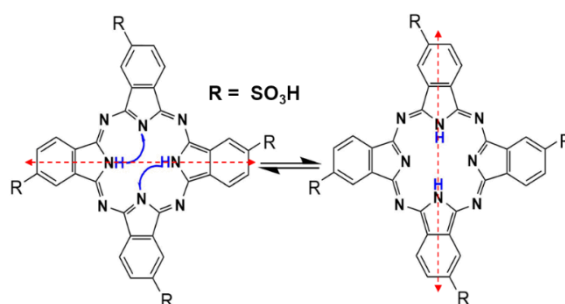


Figure 7.2. A schematic of *trans-trans* tautomerization of phthalocyanine tetrasulfonate (PcS₄) by intramolecular double hydrogen transfer. As indicated with the double red arrows, the orientation of the transition dipole moment rotates by 90° in the course of tautomerization.

7.2. Methods of Probing and Controlling NH Tautomerization

The dynamics of ground state NH tautomerization have been widely studied using NMR spectroscopy.¹⁸⁹ Wehrle et al. investigated the tautomerization time scale in crystalline porphyrin, using ¹⁵N cross-polarization magic-angle spinning (CPMAS) NMR spectroscopy. The results confirmed that the exchange of two inner hydrogens between nitrogen atoms is fast

at room temperature; however, it is “frozen” below 192 K.¹⁹⁰ The time scale of the dynamics of the inner proton of the solid-state phthalocyanine has also been investigated employing ¹⁵N and ¹³C CPMAS NMR spectroscopy, and like porphyrin, it was found to occur on the time scale of a few microseconds at about room temperature.¹⁹¹

Another powerful strategy for studying tautomerization is investigating the influence of the double proton transfer on the polarization of probing light. Fluorescence anisotropy studies have been widely employed to study the rate of NH tautomerization in the excited state.¹⁹² On the other hand, pump-probe polarization spectroscopy enables to detect both the ground and lowest excited-electronic states proton transfer rates. Fita et al. have employed this technique to study the tautomerization rate of various alkylated porphycenes.¹⁹³ Their finding confirms that: (1) self-exchange reaction is faster for molecules with strong intramolecular hydrogen bonds; (2) tunneling is significant even at 293 K. All the methods explained above provide only averaged information, as the measurements have been performed only for molecular ensembles.

Nowadays, it is possible to monitor and control the tautomerization properties of individual molecules. These can be realized mainly using three types of techniques.¹⁹⁴ The first method is single-molecule fluorescence microscopy with azimuthal polarization doughnut mode (APDM) and radial polarization doughnut mode (RPDM) excitations. This technique enables to directly observe the reorientation of the transition dipole moment during NH tautomerization. The tautomerization properties of porphycene derivatives have been widely investigated using this technique.^{195,196} Meixner, Waluk and coworkers¹⁹⁶ first recorded fluorescence emission images of single porphycene molecules embedded in a thin PMMA film, using an azimuthally polarized laser beam excitation (Figure 7.3a). The ring-like pattern of the emission intensity (molecule Σ in Figure 7.3a) is due to the presence of two transition dipoles (TDMs) forming an angle of $\sim 72^\circ$, which correspond to two *trans* tautomers of one single molecule that can rapidly interconvert on the time scale of the experiment. The double-lobe pattern observed from chromophore Π is due to either a fixed TDM (localization of the inner hydrogens) or to a specific orientation of the molecule in the polymer matrix.^{179,196}

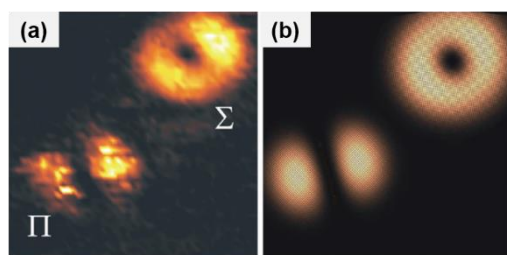


Figure 7.3. a) Confocal fluorescence image of single porphycene molecules obtained using an azimuthal polarization doughnut mode (APDM) beam. (b) Simulated fluorescence patterns, obtained by considering two differently oriented molecules with two TDMs forming an angle of 72° . The image scan area is $2.5 \times 2.5 \mu\text{m}^2$. Reprinted by permission from ref. 196. Copyright (2005) American Chemical Society.

Surface-enhanced Raman spectroscopy has also been employed to study the tautomerization properties of single porphycene molecules. For instance, Gawinkowski et al. recorded thousands of spectra from porphycene molecules placed on gold nanostructures. Repeated disappearance and appearance of some Raman peaks have been observed, due to *trans-cis-trans* tautomerization of individual porphycene molecules.¹⁹⁷

Last but not least, scanning tunneling microscopy (STM) allows looking at protons that take part in the tautomerization process at a single-molecule level.¹⁹⁸ It also enables to modulate NH tautomerization by external stimuli. For example, Böckmann et al.¹⁹⁹ studied the tautomerization properties of single porphycene molecules on a Cu(111) surface at 5 K using STM. The molecules exist in the *trans*-state on the Cu surface. However, many molecules were converted into the *cis* tautomer upon photoirradiation. Ladenthin et al. induced the *cis* \leftrightarrow *cis* tautomerization in a porphycene molecule placed on a Cu(110) surface through mechanical force, through a metallic tip close to a molecule at zero bias voltage.²⁰⁰ Recently, the intramolecular proton transfer rate in phthalocyanine molecules has been controlled by decreasing the tautomerization barrier via an electric field.²⁰¹

As explained in Chapter 6, the Purcell effect influences the singlet electronic excited-state dynamics and the probability of molecules crossing into the triplet states. Thus, it can be employed to tailor photoinduced tautomerization processes that occur in the excited states. In phthalocyanines, the orientation of the transition dipole moment (TDM) rotates by 90° upon tautomerization (Figure 7.2),²⁰² which has been visualized by the combination of confocal

microscopy with higher-order laser beams, i.e., azimuthally polarization doughnut mode (APDM) and radially polarized doughnut mode (RPDM).

7.3. Modulating Tautomerization by the Purcell Effect

The influence of the Purcell effect on the dynamics of NH tautomerization of individual phthalocyanine tetrasulfonate (PcS₄) molecules has been studied by placing PcS₄ molecules embedded in PVA in the $\lambda/2$ -microcavity described in Chapter 6. To study the correlation between the photophysical changes observed due to the Purcell effect and the dynamics of the NH tautomerization, consecutive confocal fluorescence images were acquired for single PcS₄ molecules embedded in PVA film in free space and inside the resonant cavity. For comparison, both APDM and RPDM were used as an excitation source.

Figure 7.4 presents a series of sequential fluorescence images for PcS₄ molecules in free space. When molecules were excited with APDM, either a ring-like or double lobe pattern shapes were observed. The former pattern indicates that tautomerization can be faster, whereas the latter pattern shows that NH tautomerization in PcS₄ can be slower than the image acquisition time. For instance, in Figure 7.4a (1), eleven single molecules were observed, and among them, two single molecules display ring-like patterns (indicated in green circles), and nine molecules display double-lobe features. The molecules that show the double-lobe pattern and do flip after successive scans are indicated by two-headed yellow arrows; this shows a change in the orientation of TDM of the same PcS₄ molecule because of *trans-trans* tautomerization. A single PcS₄ molecule did bleach after one scan, as is shown by a white arrow (Figure 7.4a, scan 1).

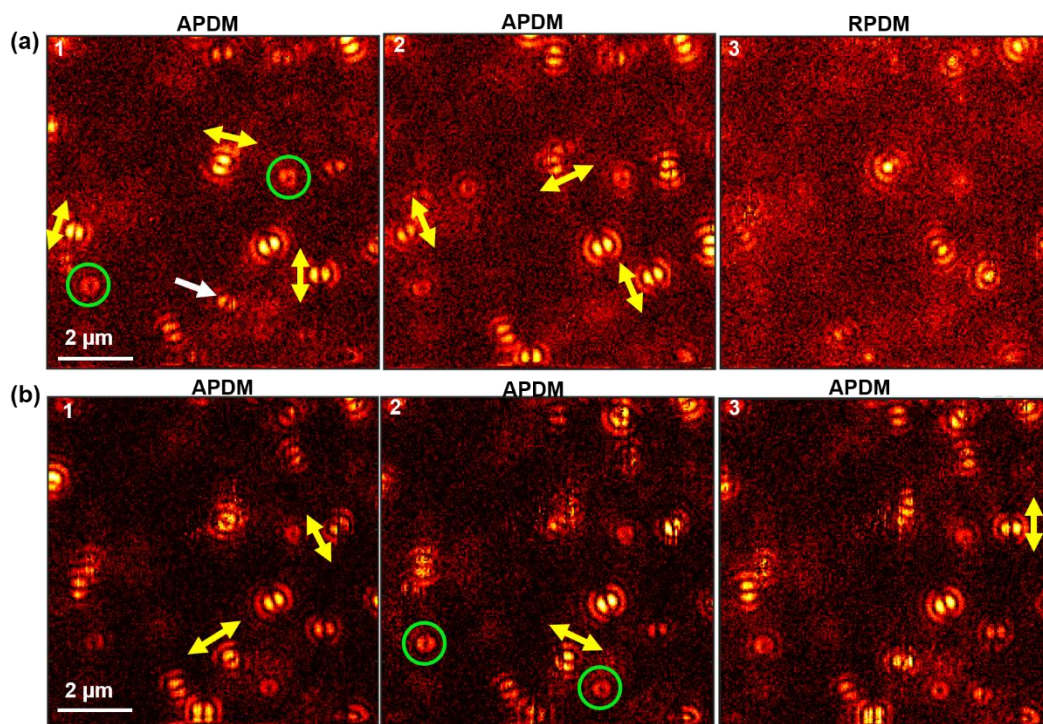


Figure 7.4. Successive fluorescence emission images of single PcS_4 molecules in free space: (a) obtained using APDM and RPDM excitation. (b) Recorded with APDM (for another sample). Single molecules displayed double lobe pattern and flipped, as indicated with double-headed arrows, while the green circles show molecules that undergo fast tautomerization (ring-like pattern).

Chizhik et al.²⁰² and Quabis et al.²⁰³ calculated intensity distribution of the electric field component of APDM and the RPDM in free space, focused using high objective lens. Their results confirmed that the APDM mode contains only in-plane components. However, the RPDM has both in-plane and longitudinal components (Figure 7.5).²⁰² Thus, as demonstrated in Figure 7.4a (3), molecules excited with RPDM in free space display both spot-like and double-lobe features. Additional consecutive confocal fluorescence images for molecules embedded in PVA in free space, acquired with APDM excitation, are presented in Figure 7.4b.

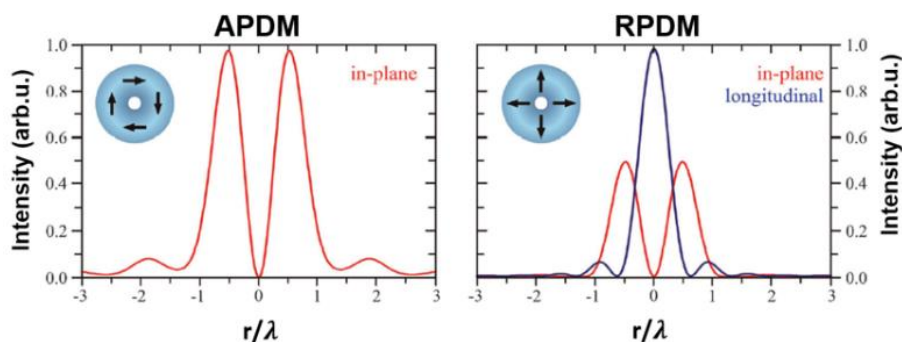


Figure 7.5. The calculated electric field intensity distribution of RPDM and APDM in free space. Reprinted by permission from ref. 202. Copyright (2013) Royal Society of Chemistry.

In contrast to PcS₄ molecules in free space, molecules placed inside a $\lambda/2$ -microcavity display only a double lobe pattern for both RPDM and APDM excitations (Figure 7.6). Besides, the flipping of the double-lobe patterns is observed very rarely (double-headed arrows in Figure 7.6), and no ring-like patterns were observed. These observations suggest that weak light-matter coupling can be used to modulate the intramolecular proton transfer dynamics, which can be directly observed on the single molecule level.

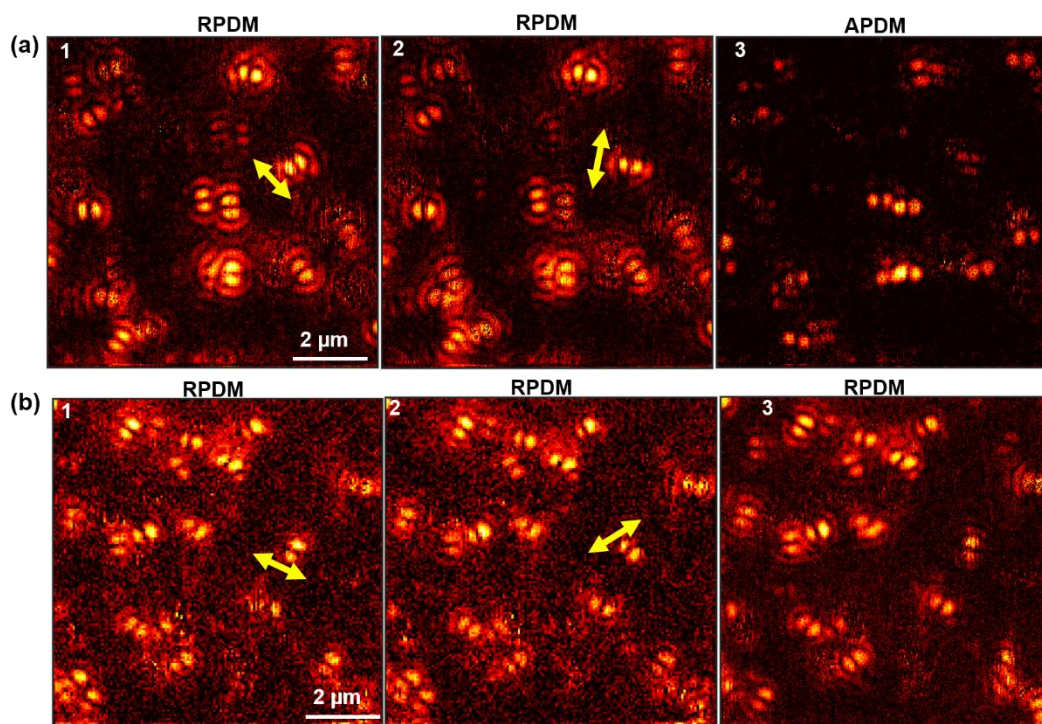


Figure 7.6. The influence of the Purcell effect on the NH tautomerization dynamics of single PcS₄ molecules. Images of individual molecules placed in a $\lambda/2$ -microcavity and obtained one after another: (a) acquired with RPDM and APDM, and (b) acquired with RPDM (for another sample).

Before presenting the statistical analysis of our results and discussing why tautomerization in PcS₄ is less probable inside a microcavity, we shall discuss first why the fluorescence emission patterns are different for molecules studied in free space and inside a microcavity. Khoptyar et al.²⁰⁴ calculated the electric field intensity distribution of the APDM and the RPDM beams focused inside the center of $\lambda/2$ microcavity using a high NA objective lens. It was found that both RPDM and APDM beams have a maximum in-plane component in the center of the cavity. However, the RPMD beam displays no longitudinal component in the center of the $\lambda/2$ cavity. Because of this, we have observed only double lobe patterns in the case of images acquired inside a microcavity.

The observed spatial single-molecule emission features are classified into three categories: double-lobe not flipped, double-lobe flipped, and ring-like. The histogram shown in Figure 7.7 presents the contributions of the three patterns from 110 single molecules. For molecules in free space, 22% of single molecules display the change in TDM reorientation, while 8% of molecules show ring-like features. In contrast, for molecules placed inside the microcavity, only 6% of the single PcS₄ molecules exhibit reorientation of the TDM during a consecutive scan. Moreover, ring-like patterns are not at all observed for PcS₄ molecules placed inside the microcavity. This verifies that the tautomerization dynamics of single molecules can be modulated by the Purcell effect of an optical microcavity.

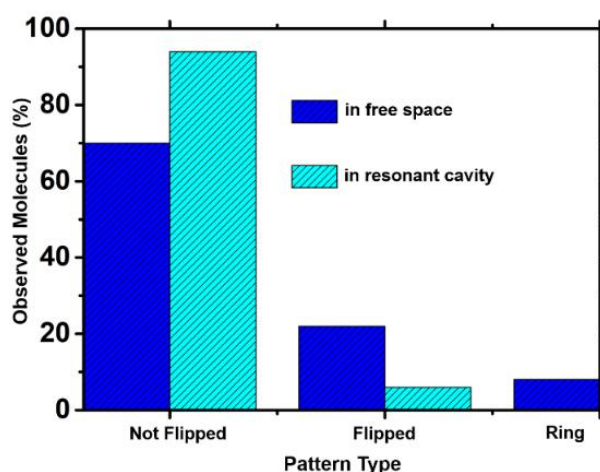


Figure 7.7. A histogram showing single molecules ($n = 110$) that display double-lobe and ring-like features for molecules embedded in PVA in free-space and inside a $\lambda/2$ -microcavity.

As explained above, the tautomerization mechanism and dynamics of phthalocyanine have many similarities with porphyrin. The ground state double proton intramolecular transfer reaction in porphyrin stops below 100 K. Nevertheless, the tautomerization can be initiated through light even at about 4 K.²⁰⁵ Recently, Doppagne et al. studied the tautomerization properties of individual phthalocyanine molecules employing the combination of STM and fluorescence spectroscopy, and they showed that the excited state of the molecule is involved in the tautomerization process. It has been claimed that the process takes place from the lowest triplet state.²⁰⁶

The triplet state quantum yield of tautomerization (ϕ_{taut}) is given by:

$$\phi_{taut} = \phi_T \cdot k_r \cdot \tau_T, \quad (7.1)$$

where ϕ_T , k_r , and τ_T are the triplet formation yield, the tautomerization rate, and the triplet lifetime, respectively. The triplet formation yield is given by:

$$\phi_T = k_{ISC} \cdot \tau_s, \quad (7.2)$$

where k_{ISC} and τ_s the intersystem crossing rate and the lowest excited singlet state lifetime. As described in Chapter 6, τ_s decreases when the molecule is placed in an optical microcavity (Figure 6.7). Thus, the triplet formation yield can be decreased inside a microcavity. This is also supported by the reduction of photobleaching and blinking (the details are given in Chapter 6). As a result, tautomerization should be less probable. Nevertheless, one might ask whether the reduction of τ_s approximately by 50% through the cavity effect is enough to slow down the tautomerization dynamics to the degree observed in Figure 7.8. As the cavity does not influence τ_T , lowering of τ_T could not be the reason for the reduction of the triplet tautomerization quantum yield. A change in the tautomerization potential in the triplet state can also be a possible source of a lower ϕ_{taut} , as it results in a reduction of k_r .

7.4. Conclusions

Confocal fluorescence microscopy with higher-order laser beams was used to study the tautomerization properties of single PcS₄ molecules. This method allows us to observe transition dipole moment reorientation during *trans-trans* tautomerization in single PcS₄ molecules. The changes in fluorescence emission pattern of single PcS₄ molecules embedded in PVA in free space and placed in a microcavity were compared by exciting with APDM and RPDM and we have observed a significant difference in the spatial fluorescence emission

patters of single molecules due to the cavity effect. We can modulate the photoinduced tautomerization properties of single phthalocyanine molecules *via* the Purcell effect of an optical microcavity. The cavity reduces the probability of molecules entering into the triplet state by enhancing the spontaneous emission rate. As a result, we have observed a significant slowing down of NH tautomerization in single PcS₄ molecules. This suggests that in our single-molecule method, we are probing the tautomerization reactions in the lowest triplet state. Our result opens a way to modulate photoinduced intramolecular reaction without external stimulus or changing the constitution of molecules, only by tuning the local density of optical states in an optical microcavity.

8. Summary and Outlook

For decades, chemists have been tailoring the physical and chemical properties of molecules by changing their chemical structure, conjugation, or constitution of atoms. For instance, a minor modification in the conjugation of organic molecules can dramatically change their ability to absorb and emit light. Obviously, chemical synthesis will continue to be widely used in modifying the properties of molecules due to its versatility and wide applications. Another approach is employing the concepts of cavity quantum electrodynamics, i.e., the phenomena of weak and strong light-matter coupling. Cavity quantum electrodynamics has been widely studied because of its practical applications in condensate physics, quantum cryptography, quantum computing, and nanophotonics. However, its potential for chemistry and material science has only recently started to be exploited. In this thesis, the spectral and photophysical properties, as well as excited state reactivity of molecules, were modulated using the vacuum electromagnetic field of an optical microcavity. For this purpose, voltage tunable microcavities were used, and molecular properties were studied at the ensemble and single-molecule levels.

In the first project of this thesis, an IR-microcavity was designed to study the influence of strong coupling on IR-absorption properties of selected systems. First, the characteristic features of strong coupling such as Rabi splitting and anticrossing have been realized by coupling the intense C=O vibrational mode of methyl salicylate with the optical mode of the cavity. The coupling of more than one molecular vibration with the same cavity mode has also been observed. Then the dynamics of the multimode coupling have been described theoretically using coupled damped harmonic oscillators. The results uncovered that the best fit between the experimental and calculated spectra of the coupled system is found when: (i) the spectrally closest off-resonance molecular vibrations, in addition to the resonance condition, are considered, and (ii) the influence of absorption of uncoupled molecules and the simultaneous coupling of close off-resonant molecular vibrations are taken into account.

In the stable methyl salicylate isomer, the phenolic O-H is intramolecularly hydrogen-bonded to the C=O group (Figure 8.1). Due to this, excited state intramolecular proton transfer (ESIPT) process can occur upon photoexcitation. Methyl salicylate behaves like a three energy levels system containing the ground state, the “normal” (MS), initially excited state (MS*), and the tautomer excited state (MSt*); Figure 8.1. MS shows a dual fluorescence, i.e., a normal emission at 350 nm and tautomer emissions at 450 nm that arise from the initially excited (MS*) and the tautomer excited (MSt*) states, respectively. Thus, one could study in the future

the influence of the multimode coupling reported in this work on the ESIPT properties of methyl salicylate.

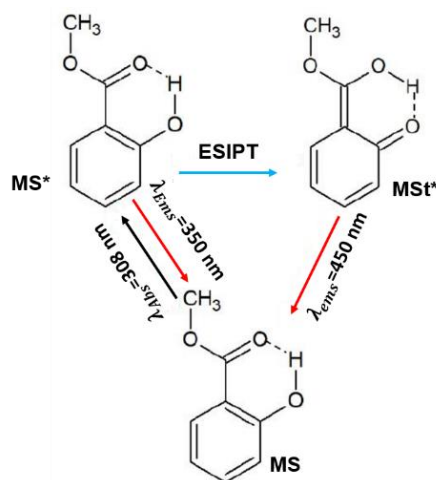


Figure 8.1. Excited state intramolecular proton transfer processes in methyl salicylate. Upon photoexcitation at 308 nm, methyl salicylate shows dual fluorescence, i.e., the normal emission at 350 nm and the tautomer emission at 450 nm that arise from the initially excited (MS^*) and tautomer excited (MS^*t) states, respectively.

Substantial time and efforts were invested to detect vibrational polaritons in selected systems in a liquid phase (methyl salicylate and benzonitrile) from the Raman scattering of the coupled systems. However, the polaritonic states were not visible in the Raman spectra, even though they can be detected in the transmission spectra of the same coupled system. Furthermore, the Raman scattering properties of polyvinyl acetate (PVAc) were studied under vibrational strong coupling regime, employing various polymer-spaced microcavities. When the PVAc film was placed in-between 10 nm Ag mirrors or 30 nm Ag bottom and 10 nm Ag top cavity mirrors, two new peaks were observed in the Raman spectra of the coupled system. However, separating the PVAc film from the top mirror with a thin layer of Cr gives spectral features similar to those observed for a reference PVAc sample. Hence, the new peaks observed in the Raman spectra of the coupled system are due to the SERS enhancement effect of the cavity mirrors. Additional experiments and literature comparisons confirmed that the SERS signals arise mainly from the toluene residue used to dissolve PVAc.

From the Raman scattering results, it was anticipated that the fraction of uncoupled molecules in the cavity volume dominates over the molecules hybridizing with the cavity mode. Due to this, the polaritonic states were not probed from the Raman scattering signal of the coupled system. Hence, one might plan to study the Raman scattering properties of molecules under ultrastrong vibrational coupling. When the Rabi splitting increases, the

number of molecules coupling with the cavity mode also increases. Thus, the likelihood of detecting Raman scattering arising from vibrational polaritons is higher in the case of ultrastrong coupling.

In the third project of this work, we have investigated the influence of weak light-matter coupling on the blinking dynamics, the photobleaching properties, and the NH tautomerization dynamics of single phthalocyanine tetrasulfonate (PcS₄) molecules. The experiments performed included fluorescence microscopy imaging of individual molecules, time-resolved fluorescence studies, and optical imaging of tautomerization using higher-order laser beams as an excitation source. In order to study the effect of the Purcell effect on photophysical and the intramolecular proton transfer dynamics of single PcS₄ molecules, the changes in the fluorescence time traces and the reorientation transition dipole moment due to tautomerization were compared for PcS₄ molecules embedded in PVA in free space and inside a $\lambda/2$ -microcavity. The results show that fluorescence intermittency, photobleaching, and photoinduced intramolecular proton transfer reaction of individual molecules become less likely in the case of molecules placed in a resonant cavity. The main reason for these observations is the enhanced spontaneous emission rate due to modification of the local optical density of states in the microcavity, which reduces the transitions of individual molecules to the triplet state. This unveils that weak light-matter coupling can steer photophysical and photoinduced chemical reactions that occur in the triplet state to the desired direction. One can envision that the photostability results may find applications in the design of efficient single-photon sources, whereas the ability to switch ON and OFF double proton transfer reactions at will by an optical microcavity could be utilized in molecular electronics.

The effects of strong coupling on the photostability and photoinduced intramolecular reaction of single molecules could be investigated in future work and compared with the results presented in this thesis. Since polaritonic states are hybrid states of the cavity photon and exciton, their relaxation rate should be faster than the intersystem crossing rate. Thus, the polaritonic states formed by electronic strong coupling could reduce the population of the triplet states. Consequently, the probability of observing photochemical, photophysical, and intramolecular processes in the triplet state from the coupled system could be lowered. To perform such type of experiments effectively, perhaps one has to employ plasmonic cavities as a coupling medium.

Finally, the results obtained in this thesis demonstrate that light-matter interaction phenomena inside a microcavity have the full potential to be used as a standard tool in modulating molecular properties and mitigating unwanted photoinduced chemical reactions.

However, to fully utilize these phenomena, many experimental and theoretical researches should be performed in the future to establish the theory of molecules—cavity interaction and its applications in the broader contexts of chemical and material sciences.

References

- (1) Zeilinger, A.; Weihs, G.; Jennewein, T.; Aspelmeyer, M. Happy Centenary, Photon. *Nature* **2005**, *433*, 230-236.
- (2) Thomas, N. C. The Early History of Spectroscopy. *J. Chem. Educ.* **1991**, *68*, 631–634.
- (3) Ruggenthaler, M.; Tancogne-Dejean, N.; Flick, J.; Appel, H.; Rubio, A. From a Quantum-Electrodynamical Light–Matter Description to Novel Spectroscopies. *Nat. Rev. Chem.* **2018**, *2*, 0118.
- (4) Flick, J.; Ruggenthaler, M.; Appel, H.; Rubio, A. Atoms and Molecules in Cavities, from Weak to Strong Coupling in Quantum-Electrodynamics (QED) Chemistry. *Proc. Natl. Acad. Sci. U. S. A.* **2017**, *114*, 3026–3034.
- (5) Hecht, J. Short History of Laser Development. *Opt. Eng.* **2010**, *49*, 091002.
- (6) Vahala, K. J. Optical Microcavities. *Nature* **2005**, *424*, 839–846.
- (7) Konrad, A.; Kern, A. M.; Brecht, M.; Meixner, A. J. Strong and Coherent Coupling of a Plasmonic Nanoparticle to a Subwavelength Fabry-Pérot Resonator. *Nano Lett.* **2015**, *15*, 4423–4428.
- (8) Bär, S.; Chizhik, A.; Gutbrod, R.; Schleifenbaum, F.; Chizhik, A.; Meixner, A. J. Microcavities: Tailoring the Optical Properties of Single Quantum Emitters. *Anal. Bioanal. Chem.* **2010**, *396*, 3-14.
- (9) Chizhik, A. I.; Chizhik, A. M.; Khoptyar, D.; Bär, S.; Meixner, A. J.; Enderlein, J. Probing the Radiative Transition of Single Molecules with a Tunable Microresonator. *Nano Lett.* **2011**, *11*, 1700–1703.
- (10) Thompson, R. C. High Resolution Laser Spectroscopy of Atomic Systems. *Rep. Prog. Phys.* **1985**, *48*, 531–578.
- (11) Lindroth, E.; Calegari, F.; Young, L.; Harmand, M.; Dudovich, N.; Berrah, N.; Smirnova, O. Challenges and Opportunities in Attosecond and XFEL Science. *Nat. Rev. Phys.* **2019**, *1*, 107–111.
- (12) Ambrose, W. P.; Goodwin, P. M.; Jett, J. H.; Van Orden, A.; Werner, J. H.; Keller, R. A. Single Molecule Fluorescence Spectroscopy at Ambient Temperature. *Chem. Rev.* **1999**, *99*, 2929–2956.
- (13) Schleifenbaum, F.; Blum, C.; Elgass, K.; Subramaniam, V.; Meixner, A. J. New Insights into the Photophysics of DsRed by Multiparameter Spectroscopy on Single Proteins. *J. Phys. Chem. B* **2008**, *112*, 7669–7674.
- (14) Blum, C.; Stracke, F.; Becker, S.; Müllen, K.; Meixner, A. J. Discrimination and

- Interpretation of Spectral Phenomena by Room-Temperature Single-Molecule Spectroscopy. *J. Phys. Chem. A* **2001**, *105*, 6983–6990.
- (15) Brif, C.; Chakrabarti, R.; Rabitz, H. Control of Quantum Phenomena: Past, Present and Future. *New J. Phys.* **2010**, *12*, 075008.
- (16) Koehl, R. M.; Nelson, K. A. Coherent Optical Control over Collective Vibrations Traveling at Lightlike Speeds. *J. Chem. Phys.* **2001**, *114*, 1443–1446.
- (17) Xiao, Y. F.; Gong, Q. Optical Microcavity: From Fundamental Physics to Functional Photonics Devices. *Sci. Bull.* **2016**, *61*, 185–186.
- (18) Bitarafan, M. H.; DeCorby, R. G. On-Chip High-Finesse Fabry-Pérot Microcavities for Optical Sensing and Quantum Information. *Sensors* **2017**, *17*, 1748.
- (19) Kavokin, A.V.; Baumberg, J.J; Malpuech, G.; Laussy, F.B. *Microcavities*, Oxford University Press, **2007**.
- (20) Mochalov, K. E.; Vaskan, I. S.; Dovzhenko, D. S.; Rakovich, Y. P.; Nabiev, I. A Versatile Tunable Microcavity for Investigation of Light-Matter Interaction. *Rev. Sci. Instrum.* **2018**, *89*, 053105.
- (21) Fox, M. *Quantum Optics an Introduction*, Oxford University Press, **2006**.
- (22) Kern, A. M.; Zhang, D.; Brecht, M.; Chizhik, A. I.; Failla, A. V.; Wackenhut, F.; Meixner, A. J. Enhanced Single-Molecule Spectroscopy in Highly Confined Optical Fields: From $\lambda/2$ -Fabry-Pérot Resonators to Plasmonic Nano-Antennas. *Chem. Soc. Rev.* **2014**, *43*, 1263–1286.
- (23) Saleh, B.E.A.; Teich, M.C. *Fundamentals of Photonics*, John Wiley and Sons, Inc., **1999**.
- (24) Hertzog, M.; Wang, M.; Mony, J.; Börjesson, K. Strong Light-Matter Interactions: A New Direction within Chemistry. *Chem. Soc. Rev.* **2019**, *48*, 937–961.
- (25) Purcell, E., M. Spontaneous emission probabilities at radio frequencies. *Phys. Rev.* **1946**, *69*, 681.
- (26) Drexhage, K. H.; Kuhn, H.; Schäfer, F. P. Variation of the Fluorescence Decay Time of a Molecule in Front of a Mirror, *Ber. Bunsen Phys. Chem.*, **1968**, *72*, 329.
- (27) Nezhad, M. P.; Simic, A.; Bondarenko, O.; Slutsky, B.; Mizrahi, A.; Feng, L.; Lomakin, V.; Fainman, Y. Room-Temperature Subwavelength Metallo-Dielectric Lasers. *Nat. Photonics* **2010**, *4*, 395–399.
- (28) Ryu, H. Y. Investigation of the Purcell Effect in GaN-Based Vertical LED Structures Using FDTD Simulation. *Opt. Quantum Electron.* **2016**, *48*, 6.
- (29) Holzmeister, P.; Pibiri, E.; Schmied, J. J.; Sen, T.; Acuna, G. P.; Tinnefeld, P. Quantum

- Yield and Excitation Rate of Single Molecules Close to Metallic Nanostructures. *Nat. Commun.* **2014**, *5*, 5356.
- (30) Andrew, P.; Barnes, W. L. Förster Energy Transfer in an Optical Microcavity. *Science* **2000**, *290*, 785–788.
- (31) Dovzhenko, D. S.; Ryabchuk, S. V.; Rakovich, Y. P.; Nabiev, I. R. Light-Matter Interaction in the Strong Coupling Regime: Configurations, Conditions, and Applications. *Nanoscale* **2018**, *10*, 3589–3605.
- (32) Rempe, G.; Walther, H.; Klein, N. Observation of Quantum Collapse and Revival in a One-Atom Maser. *Phys. Rev. Lett.* **1987**, *58*, 353–356.
- (33) Weisbuch, C.; Nishioka, M.; Ishikawa, A.; Arakawa, Y. Observation of the Coupled Exciton-Photon Mode Splitting in a Semiconductor Quantum Microcavity. *Phys. Rev. Lett.* **1992**, *69*, 3314–3317.
- (34) Michetti, P.; Mazza, L.; Rocca, G. C. Strongly Coupled Organic Microcavities. in *Organic Nanophotonics, Nano-Optics and Nanophotonics*, Springer-Verlag: Berlin Heidelberg, **2015**.
- (35) Lidzey, D. G.; Bradley, D. D. C.; Skolnick, M. S.; Virgili, T.; Walker, S.; Whittaker, D. M. Strong Exciton-Photon Coupling in an Organic Semiconductor Microcavity. *Nature* **1998**, *395*, 53–55.
- (36) Lidzey, D.G.; Bradley, D. D. C.; Virgili, T.; Armitage, A.; Skolnick, M. S.; Walker, S. Room Temperature Polariton Emission from Strongly Coupled Organic Semiconductor, *Phys. Rev. Lett.* **1999**, *82*, 3316-3319.
- (37) Bahsoun, H.; Chervy, T.; Thomas, A.; Börjesson, K.; Hertzog, M.; George, J.; Devaux, E.; Genet, C.; Hutchison, J. A.; Ebbesen, T. W. Electronic Light-Matter Strong Coupling in Nanofluidic Fabry-Pérot Cavities. *ACS Photonics* **2018**, *5*, 225–232.
- (38) Chikkaraddy, R.; De Nijs, B.; Benz, F.; Barrow, S. J.; Scherman, O. A.; Rosta, E.; Demetriadou, A.; Fox, P.; Hess, O.; Baumberg, J. J. Single-Molecule Strong Coupling at Room Temperature in Plasmonic Nanocavities. *Nature* **2016**, *535*, 127–130.
- (39) Hugall, J. T.; Singh, A.; Van Hulst, N. F. Plasmonic Cavity Coupling. *ACS Photonics* **2018**, *5*, 43–53.
- (40) Baranov, D. G.; Wersäll, M.; Cuadra, J.; Antosiewicz, T. J.; Shegai, T. Novel Nanostructures and Materials for Strong Light-Matter Interactions. *ACS Photonics* **2018**, *5*, 24–42.
- (41) Shalabney, A.; George, J.; Hutchison, J.; Pupillo, G.; Genet, C.; Ebbesen, T. W. Coherent Coupling of Molecular Resonators with a Microcavity Mode. *Nat. Commun.*

- 2015**, 6, 5981.
- (42) Long, J. P.; Simpkins, B. S. Coherent Coupling between a Molecular Vibration and Fabry-Pérot Optical Cavity to Give Hybridized States in the Strong Coupling Limit. *ACS Photonics* **2015**, 2, 130–136.
- (43) George, J.; Shalabney, A.; Hutchison, J. A.; Genet, C.; Ebbesen, T. W. Liquid-Phase Vibrational Strong Coupling. *J. Phys. Chem. Lett.* **2015**, 6, 1027–1031.
- (44) George, J.; Chervy, T.; Shalabney, A.; Devaux, E.; Hiura, H.; Genet, C.; Ebbesen, T. W. Multiple Rabi Splittings under Ultrastrong Vibrational Coupling. *Phys. Rev. Lett.* **2016**, 117, 53601.
- (45) Menghrajani, K. S.; Fernandez, H. A.; Nash, G. R.; Barnes, W. L. Hybridization of Multiple Vibrational Modes via Strong Coupling Using Confined Light Fields. *Adv. Opt. Mater.* **2019**, 7, 1900403.
- (46) Muallem, M.; Palatnik, A.; Nessim, G. D.; Tischler, Y. R. Strong Light-Matter Coupling and Hybridization of Molecular Vibrations in a Low-Loss Infrared Microcavity. *J. Phys. Chem. Lett.* **2016**, 7, 2002-2008.
- (47) Crum, V. F.; Casey, S. R.; Sparks, J. R. Photon-Mediated Hybridization of Molecular Vibrational States. *Phys. Chem. Chem. Phys.* **2018**, 20, 850-857.
- (48) Erwin, J. D.; Smotzer, M.; Coe, J. V. Effect of Strongly Coupled Vibration-Cavity Polaritons on the Bulk Vibrational States within a Wavelength-Scale Cavity. *J. Phys. Chem. B* **2019**, 123, 1302–1306.
- (49) Hertzog, M.; Rudquist, P.; Hutchison, J. A.; George, J.; Ebbesen, T. W.; Börjesson, K. Voltage-Controlled Switching of Strong Light – Matter Interactions Using Liquid Crystals. *Chem. Eur. J.* **2017**, 23, 18166-18170.
- (50) Pino, J. Del; Feist, J.; Garcia-Vidal, F. J. Quantum Theory of Collective Strong Coupling of Molecular Vibrations with a Microcavity Mode. *New J. Phys.* **2015**, 17, 53040.
- (51) Lerario, G.; Ballarini, D.; Fieramosca, A.; Cannavale, A.; Genco, A.; Mangione, F.; Gambino, S.; Dominici, L.; De Giorgi, M.; Gigli, G.; et al. High-Speed Flow of Interacting Organic Polaritons. *Light Sci. Appl.* **2017**, 6, e16212.
- (52) Keeling, J.; Kéna-Cohen, S. Bose-Einstein Condensation of Exciton-Polaritons in Organic Microcavities. *Annu. Rev. Phys. Chem.* **2020**, 71, 435–459.
- (53) Nikolis, V. C.; Mischok, A.; Siegmund, B.; Kublitski, J.; Jia, X.; Benduhn, J.; Hörmann, U.; Neher, D.; Gather, M. C.; Spoltore, D.; et al. Strong Light-Matter Coupling for Reduced Photon Energy Losses in Organic Photovoltaics. *Nat. Commun.* **2019**, 10, 3706.

- (54) Eizner, E.; Brodeur, J.; Barachati, F.; Sridharan, A.; Kéna-Cohen, S. Organic Photodiodes with an Extended Responsivity Using Ultrastrong Light-Matter Coupling. *ACS Photonics* **2018**, *5*, 2921–2927.
- (55) Hutchison, J. A.; Schwartz, T.; Genet, C.; Devaux, E.; Ebbesen, T. W. Modifying Chemical Landscapes by Coupling to Vacuum Fields. *Angew. Chem Int. Ed.* **2012**, *51*, 1592–1596.
- (56) Hutchison, J. A.; Liscio, A.; Schwartz, T.; Canaguier-Durand, A.; Genet, C.; Palermo, V.; Samorì, P.; Ebbesen, T. W. Tuning the Work-Function Via Strong Coupling. *Adv. Mater.* **2013**, *25*, 2481–2485.
- (57) Orgiu, E.; George, J.; Hutchison, J. A.; Devaux, E.; Dayen, J. F.; Doudin, B.; Stellacci, F.; Genet, C.; Schachenmayer, J.; Genes, C.; Pupillo, G.; Samorì, P.; Ebbesen, T.W. Conductivity in Organic Semiconductors Hybridized with the Vacuum Field. *Nat. Mater.* **2015**, *14*, 1123–1129.
- (58) Wang, S.; Chervy, T.; George, J.; Hutchison, J. A.; Genet, C.; Ebbesen, T. W. Quantum Yield of Polariton Emission from Hybrid Light-Matter States. *J. Phys. Chem. Lett.* **2014**, *5*, 1433–1439.
- (59) Stranius, K.; Hertzog, M.; Börjesson, K. Selective Manipulation of Electronically Excited States through Strong Light-Matter Interactions. *Nat. Commun.* **2018**, *9*, 2273.
- (60) Yuen-Zhou, J.; Menon, V. M. Polariton Chemistry: Thinking inside the (Photon) Box. *Proc. Natl. Acad. Sci. U. S. A.* **2019**, *116*, 5214–5216.
- (61) Ribeiro, R. F.; Martínez-Martínez, L. A.; Du, M.; Campos-Gonzalez-Angulo, J.; Yuen-Zhou, J. Polariton Chemistry: Controlling Molecular Dynamics with Optical Cavities. *Chem. Sci.* **2018**, *9*, 6325–6339.
- (62) Vurgaftman, I.; Simpkins, B. S.; Dunkelberger, A. D.; Owrutsky, J. C. Negligible Effect of Vibrational Polaritons on Chemical Reaction Rates via the Density of States Pathway. *J. Phys. Chem. Lett.* **2020**, *11*, 3557–3562.
- (63) Feist, J.; Galego, J.; Garcia-Vidal, F. J. Polaritonic Chemistry with Organic Molecules. *ACS Photonics* **2018**, *5*, 205–216.
- (64) Herrera, F.; Owrutsky, J. Molecular Polaritons for Controlling Chemistry with Quantum Optics. *J. Chem. Phys.* **2020**, *152*, 100902.
- (65) Al-Amri, M.D.; El-Gomati, M. M.; Zubairy, M.S. *Optics in Our Time*, Springer, **2016**.
- (66) Chitu, C.; Dumitran, A.; Manole, C.; Antohe, S. The Light - an Integrated Approach to the Phenomenon. *Procedia - Soc. Behav. Sci.* **2011**, *15*, 277–283.
- (67) Atkins, P.; Friedman, R. *Molecular Quantum Mechanics*, Oxford University Press,

- 2005.**
- (68) Ellgen, P.C. *Thermodynamics and Chemical Equilibrium*, Oklahoma School of Science and Mathematics, **2014**.
- (69) Mortimer, R.G. *Physical Chemistry*, Elsevier Inc., **2008**.
- (70) Silbey, R.J.; Alberty, R.A.; Bawendi, M.G. *Physical Chemistry*, John Wiley & Sons, Inc., **2005**.
- (71) Coates, J. Interpretation of Infrared Spectra, A Practical Approach. *Encycl. Anal. Chem.* **2004**, 1–23.
- (72) Harris, D.C.; Bertolucci, M.D. *Symmetry and Spectroscopy: An Introduction to Vibrational and Electronic Spectroscopy*, Oxford University Press, **1989**.
- (73) Siebert, F.; Hildebrandt, P. *Vibrational Spectroscopy in Life Science*. Wiley-VCH Verlag GmbH and Co. KGaA, Weinheim, **2008**.
- (74) Atkins, P.; Paula, J.D. *Physical Chemistry*, Oxford University Press, **2006**.
- (75) Stuart, B. *Infrared Spectroscopy: Fundamentals and Applications*, John Wiley and Sons, **2004**.
- (76) Reichenbacher, M.; Popp, J. *Challenges in Molecular Structure Determination*; Springer-Verlag Berlin Heidelberg, **2012**.
- (77) McCreery, R.L. *Raman Spectroscopy for Chemical Analysis*, John Wiley and Sons, **2000**.
- (78) Ru, E. L.; Etchegoin, P. *Principles of Surface Enhanced Raman Spectroscopy and Related Plasmonics Effects*. Elsevier Science, **2009**.
- (79) So, P.T.C.; Dong, C.Y. Fluorescence Spectrophotometry. *eLS*. **2002**, 1-4.
- (80) Itoh, T. Fluorescence and Phosphorescence from Higher Excited States of Organic Molecules. *Chem. Rev.* **2012**, *112*, 4541–4568.
- (81) Noomnarm, U.; Clegg, R. M. Fluorescence Lifetimes: Fundamentals and Interpretations. *Photosynth. Res.* **2009**, *10*, 181–194.
- (82) Sauer, M.; Hofkens, J.; Enderlein, J. *Handbook of Fluorescence Spectroscopy and Imaging*, Wiley-VCH Verlag GmbH and Co. KGaA, Weinheim, **2011**.
- (83) Alinejad, N.; Pishbin, N. Spontaneous Emission of an Excited Atom in a Dusty Unmagnetized Plasma Medium. *Adv. Mater. Sci. Eng.* **2014**, 746742.
- (84) Barnes, W. L.; Horsley, S. A. R.; Vos, W. L. Classical Antennae, Quantum Emitters, and Densities of Optical States. *J. Opt.* **2020**, *22*, 73501.
- (85) Barnes, W. L. Fluorescence near Interfaces: The Role of Photonic Mode Density. *J. Mod. Opt.* **1998**, *45*, 661–699.

- (86) Pelton, M. Modified Spontaneous Emission in Nanophotonic Structures. *Nat. Photonics* **2015**, *9*, 427–435.
- (87) Novotny, L. Strong Coupling, Energy Splitting, and Level Crossings: A Classical Perspective. *Am. J. Phys.* **2010**, *78*, 1199–1202.
- (88) Lidzey, D.G.; Coles, D.M. Strong Coupling in Organic and Hybrid-Semiconductor Microcavity Structures. in *Organic and Hybrid Photonic Crystals*, Springer, **2015**.
- (89) Shore, B. W.; Knight, P. L. Topical Review The Jaynes-Cummings Model. *J. Mod. Opt.* **1993**, *40*, 1195–1238.
- (90) Kosik, M.; Burlayenko, O.; Rockstuhl, C.; Fernandez-Corbaton, I.; Słowik, K. Interaction of Atomic Systems with Quantum Vacuum beyond Electric Dipole Approximation. *Sci. Rep.* **2020**, *10*, 5879.
- (91) Vasa, P. Strong Light – Matter Interaction. *Encyclopedia of Applied Physics* **2019**, eap828.
- (92) May, M. A.; Fialkow, D.; Wu, T.; Park, K.; Leng, H.; Kropp, J. A.; Gougousi, T.; Lalanne, P.; Pelton, M.; Raschke, M. B. Nano-Cavity QED with Tunable Nano-Tip Interaction. *Adv. Quantum Technol.* **2020**, *3*, 1900087.
- (93) Zengin, G.; Wersäll, M.; Nilsson, S.; Antosiewicz, T. J.; Käll, M.; Shegai, T. Realizing Strong Light-Matter Interactions between Single-Nanoparticle Plasmons and Molecular Excitons at Ambient Conditions. *Phys. Rev. Lett.* **2015**, *114*, 1–6.
- (94) Garraway, B. M. The Dicke Model in Quantum Optics: Dicke Model Revisited. *Philos. Trans. R. Soc. A Math. Phys. Eng. Sci.* **2011**, *369*, 1137–1155.
- (95) Coles, D. M.; Michetti, P.; Clark, C.; Adawi, A. M.; Lidzey, D. G. Temperature Dependence of the Upper-Branch Polariton Population in an Organic Semiconductor Microcavity. *Phys. Rev. B - Condens. Matter Mater. Phys.* **2011**, *84*, 205214.
- (96) Swann, S. Magnetron Sputtering. *Phys Techno.* **1988**, *19*, 67–75.
- (97) Seshan, K. *Handbook of Thin-Film Deposition Processes and Techniques*, Noyes Publications, **2002**.
- (98) Baptista, A.; Silva, F. J. G.; Porteiro, J.; Míguez, J. L.; Pinto, G.; Fernandes, L. On the Physical Vapour Deposition (PVD): Evolution of Magnetron Sputtering Processes for Industrial Applications. *Procedia Manuf.* **2018**, *17*, 746–757.
- (99) Wang, Z.; Zhang, Z. Electron Beam Evaporation Deposition. *Adv. Nano Depos. Methods* **2016**, 33–58.
- (100) Norrman, K.; Ghanbari-Siahkali, A.; Larsen, N. B. Studies of Spin-Coated Polymer

- Films. *Annu. Reports Prog. Chem. Sect. C* **2005**, *101*, 174–201.
- (101) Mohajerani, E.; Farajollahi, F.; Mahzoon, R.; Baghery, S. Morphological and Thickness Analysis for PMMA Spin Coated Films. *J. Optoelectron. Adv. Mater.* **2007**, *9*, 3901–3906.
- (102) Smith, B.C. *Fundamentals of Fourier Transform Infrared Spectroscopy*, CRC Press, **2011**.
- (103) Lozeman, J. J. A.; Führer, P.; Olthuis, W.; Odijk, M. Spectroelectrochemistry, the Future of Visualizing Electrode Processes by Hyphenating Electrochemistry with Spectroscopic Techniques. *Analyst* **2020**, *145*, 2482–2509.
- (104) Codan, B.; Sergo, V. Implementation of Maskless Laser Lithography Using a Raman Spectroscopy Microprobe. *Rev. Sci. Instrum.* **2008**, *79*, 096103.
- (105) Moerner, W. E.; Kador, L. Optical Detection and Spectroscopy of Single Molecules in a Solid. *Phys. Rev. Lett.* **1989**, *62*, 2535–2538.
- (106) Laine, R. F.; Schierle, G. S. K.; Van De Linde, S.; Kaminski, C. F. From Single-Molecule Spectroscopy to Super-Resolution Imaging of the Neuron: A Review. *Methods Appl. Fluoresc.* **2016**, *4*, 22004.
- (107) Basché, T.; Moerner, W. E.; Orrit, M.; Talon, H. Photon Antibunching in the Fluorescence of a Single Dye Molecule Trapped in a Solid. *Phys. Rev. Lett.* **1992**, *69*, 1516–1519.
- (108) Becker., W. *The BH TCSPC Handbook: Time-correlated Single Photon Counting Modules*, Becker and Hickl GmbH, **2012**.
- (109) Zhan, Q. Cylindrical Vector Beams: From Mathematical Concepts to Applications. *Adv. Opt. Photonics.* **2009**, *1*, 1–57.
- (110) Züchner, T.; Failla, A. V.; Meixner, A. J. Light Microscopy with Doughnut Modes: A Concept to Detect, Characterize, and Manipulate Individual Nanoobjects. *Angew. Chem., Int. Ed.* **2011**, *50*, 5274–5293.
- (111) Cremer, D.; Kraka, E. From Molecular Vibrations to Bonding, Chemical Reactions, and Reaction Mechanism. *Curr. Org. Chem.* **2010**, *14*, 1524–1560.
- (112) Henriksen, N. E. Laser Control of Chemical Reactions. *Chem. Soc. Rev.* **2002**, *31*, 37–42.
- (113) Phuc, N. T.; Trung, P. Q.; Ishizaki, A. Controlling the Nonadiabatic Electron-Transfer Reaction Rate through Molecular-Vibration Polaritons in the Ultrastrong Coupling Regime. *Sci. Rep.* **2020**, *10*, 7318.
- (114) Takele, W. M.; Wackenhut, F.; Piatkowski, L.; Meixner, A. J.; Waluk, J. Multimode

- Vibrational Strong Coupling of Methyl Salicylate to a Fabry-Pérot Microcavity. *J. Phys. Chem. B* **2020**, *124*, 5709–5716.
- (115) Thomas, A.; George, J.; Shalabney, A.; Dryzhakov, M.; Varma, S. J.; Moran, J.; Chervy, T.; Zhong, X.; Devaux, E.; Genet, C.; Hutchison, J. A.; Ebbesen, T. W. Ground-State Chemical Reactivity under Vibrational Coupling to the Vacuum Electromagnetic Field. *Angew. Chem. Int. Ed.* **2016**, *55*, 11462-11466.
- (116) Lather, J.; Bhatt, P.; Thomas, A.; Ebbesen, T. W.; George, J. Cavity Catalysis by Cooperative Vibrational Strong Coupling of Reactant and Solvent Molecules. *Angew. Chem. Int. Ed.* **2019**, *58*, 10635–10638.
- (117) Thomas, A.; Lethuillier-Karl, L.; Nagarajan, K.; Vergauwe, R. M. A.; George, J.; Chervy, T.; Shalabney, A.; Devaux, E.; Genet, C.; Moran, J.; Ebbesen, T. W. Tilting a Ground-State Reactivity Landscape by Vibrational Strong Coupling. *Science* **2019**, *363*, 615–619.
- (118) Pang, Y.; Thomas, A.; Nagarajan, K.; Vergauwe, R. M. A.; Joseph, K.; Patrahau, B.; Wang, K.; Genet, C.; Ebbesen, T. W. On the Role of Symmetry in Vibrational Strong Coupling: The Case of Charge-Transfer Complexation. *Angew. Chem. Int. Ed.* **2020**, *132*, 1–6.
- (119) Xiang, B.; Ribeiro, R. F.; Du, M.; Chen, L.; Yang, Z.; Wang, J.; Yuen-Zhou, J.; Xiong, W. Intermolecular Vibrational Energy Transfer Enabled by Microcavity Strong Light–Matter Coupling. *Science* **2020**, *368*, 665–667.
- (120) Kapon, O.; Yitzhari, R.; Palatnik, A.; Tischler, Y. R. Vibrational Strong Light-Matter Coupling Using a Wavelength-Tunable Mid-Infrared Open Microcavity. *J. Phys. Chem. C* **2017**, *121*, 18845–18853.
- (121) Massaro, R. D.; Dai, Y.; Blaisten-Barojas, E. Energetics and Vibrational Analysis of Methyl Salicylate Isomers. *J. Phys. Chem. A* **2009**, *113*, 10385–10390.
- (122) Varghese, H. T.; Yohannan Panicker, C.; Philip, D.; Mannekutla, J. R.; Inamdar, S. R. IR, Raman and SERS Studies of Methyl Salicylate. *Spectrochim. Acta - Part A Mol. Biomol. Spectrosc.* **2007**, *66*, 959–963.
- (123) Ebbesen, T. W. Hybrid Light-Matter States in a Molecular and Material Science Perspective. *Acc. Chem. Res.* **2016**, *49*, 2403–2412.
- (124) Xiang, B.; Ribeiro, R. F.; Dunkelberger, A. D.; Wang, J.; Li, Y.; Simpkins, B. S.; Owrutsky, J. C.; Yuen-Zhou, J.; Xiong, W. Two-Dimensional Infrared Spectroscopy of Vibrational Polaritons. *Proc. Natl. Acad. Sci. U. S. A.* **2018**, *115*, 4845–4850.
- (125) Junginger, A.; Wackenhut, F.; Stuhl, A.; Blendinger, F.; Brecht, M.; Meixner, A. J.

- Tunable Strong Coupling of Two Adjacent Optical $\lambda/2$ Fabry-Pérot Microresonators. *Opt. Express* **2020**, *28*, 485.
- (126) Zhu, X.; Xu, T.; Lin, Q.; Duan, Y. Technical Development of Raman Spectroscopy: From Instrumental to Advanced Combined Technologies. *Appl. Spectrosc. Rev.* **2014**, *49*, 64–82.
- (127) Jones, R. R.; Hooper, D. C.; Zhang, L.; Wolverson, D.; Valev, V. K. Raman Techniques: Fundamentals and Frontiers. *Nanoscale Res. Lett.* **2019**, *14*, 2-34.
- (128) Pérez-Jiménez, A. I.; Lyu, D.; Lu, Z.; Liu, G.; Ren, B. Surface-Enhanced Raman Spectroscopy: Benefits, Trade-Offs and Future Developments. *Chem. Sci.* **2020**, *11*, 4563–4577.
- (129) Shao, F.; Zenobi, R. Tip-Enhanced Raman Spectroscopy: Principles, Practice, and Applications to Nanospectroscopic Imaging of 2D Materials. *Anal. Bioanal. Chem.* **2019**, *411*, 37–61.
- (130) Hummer, T.; Noe, J.; Hofmann, M. S.; Hansch, T. W.; Hogele, A.; Hunger, D. Cavity-Enhanced Raman Microscopy of Individual Carbon Nanotubes. *Nat. Commun.* **2016**, *7*, 12155.
- (131) Cairo, F.; Martini, F.D.; Murra, D., QED-Vacuum Confinement of Inelastic Quantum Scattering at Optical Frequencies: A New Perspective in Raman Spectroscopy Spectroscopy, *Phys. Rev. Lett.*, **1993**, *70*, 1413-1416.
- (132) Petrak, B.; Cooper, J.; Konthasinghe, K.; Peiris, M.; Djeu, N.; Hopkins, A. J.; Muller, A. Isotopic Gas Analysis through Purcell Cavity Enhanced Raman Scattering. *Appl. Phys. Lett.* **2016**, *108*, 091107.
- (133) Fainstein, A.; Jusserand, B.; Thierry-Mieg, V. Raman Scattering Enhancement by Optical Confinement in a Semiconductor Planar Microcavity. *Phys. Rev. Lett.* **1995**, *75*, 3764–3767.
- (134) Nagasawa, F.; Takase, M.; Murakoshi, K. Raman Enhancement via Polariton States Produced by Strong Coupling between a Localized Surface Plasmon and Dye Excitons at Metal Nanogaps. *J. Phys. Chem. Lett.* **2014**, *5*, 14–19.
- (135) Shalabney, A.; George, J.; Hiura, H.; Hutchison, J. A.; Genet, C.; Hellwig, P.; Ebbesen, T. W. Enhanced Raman Scattering from Vibro-Polariton Hybrid States. *Angew. Chem - Int. Ed.* **2015**, *54*, 7971–7975.
- (136) Taylor, L. S.; Langkilde, F. W.; Zografi, G. Fourier Transform Raman Spectroscopic Study of the Interaction of Water Vapor with Amorphous Polymers. *J. Pharm. Sci.* **2001**, *90*, 888–901.

- (137) Qian, C.; Guo, Q.; Xu, M.; Yuan, Y.; Yao, J. Improving the SERS Detection Sensitivity of Aromatic Molecules by a PDMS-Coated Au Nanoparticle Monolayer Film. *RSC Adv.* **2015**, *5*, 53306–53312.
- (138) del Pino, J.; Feist, J.; Garcia-Vidal, F. J. Signatures of Vibrational Strong Coupling in Raman Scattering. *J. Phys. Chem. C* **2015**, *119*, 29132–29137.
- (139) Strashko, A.; Keeling, J. Raman Scattering with Strongly Coupled Vibron-Polaritons. *Phys. Rev. A* **2016**, *94*, 023843.
- (140) Tartakovskii, A. I.; Emam-Ismael, M.; Lidzey, D. G.; Skolnick, M. S.; Bradley, D. D.; Walker, S.; Agranovich, V. M.; Raman Scattering in Strongly Coupled Organic Semiconductor Microcavities. *Phys. Rev. B* **2001**, *63*, 121302.
- (141) Minamimoto, H.; Kato, F.; Nagasawa, F.; Takase, M.; Murakoshi, K. Electrochemical Control of Strong Coupling States between Localized Surface Plasmons and Molecule Excitons for Raman Enhancement. *Faraday Discuss.* **2017**, *205*, 261–269.
- (142) Cade, N. I.; Ritman-Meer, T.; Richards, D. Strong Coupling of Localized Plasmons and Molecular Excitons in Nanostructured Silver Films. *Phys. Rev. B*, **2009**, *79*, 241404.
- (143) Tribe, W. R.; Baxter, D.; Skolnick, M. S.; Mowbray, D. J.; Fisher, T. A.; Roberts, J. S., In- and out-going resonant Raman scattering from the cavity polaritons of semiconductor quantum microcavities. *Phys. Rev. B* **1997**, *56*, 429–433.
- (144) Zhao, D.; Liu, S.; Gao, Y. Single-Molecule Manipulation and Detection. *Acta Biochim. Biophys. Sin.* **2018**, *50*, 231–237.
- (145) Barkai, E.; Jung, Y. J.; Silbey, R. Theory of Single-Molecule Spectroscopy: Beyond the Ensemble Average. *Annu. Rev. Phys. Chem.* **2004**, *55*, 457–507.
- (146) Stennett, E. M. S.; Ciuba, M. A.; Levitus, M. Photophysical Processes in Single Molecule Organic Fluorescent Probes. *Chem. Soc. Rev.* **2014**, *43*, 1057–1075.
- (147) Michalet, X.; Weiss, S.; Jager, M. Single-Molecule Fluorescence Studies of Protein Folding. *Chem. Rev.* **2006**, *106*, 1785–1813.
- (148) Gooding, J. J.; Gaus, K. Single-Molecule Sensors: Challenges and Opportunities for Quantitative Analysis. *Angew. Chem - Int. Ed.* **2016**, *55*, 11354–11366.
- (149) Zhang, L.; Yu, Y. J.; Chen, L. G.; Luo, Y.; Yang, B.; Kong, F. F.; Chen, G.; Zhang, Y.; Zhang, Q.; Luo, Y.; et al. Electrically Driven Single-Photon Emission from an Isolated Single Molecule. *Nat. Commun.* **2017**, *8*, 580.
- (150) Betzig, E.; Patterson, G. H.; Sougrat, R.; Lindwasser, O. W.; Olenych, S.; Bonifacino, J. S.; Davidson, M. W.; Lippincott-Schwartz, J.; Hess, H. F. Imaging Intracellular Fluorescent Proteins at Nanometer Resolution. *Science* **2006**, *313*, 1642–1645.

- (151) Sun, L.; Diaz-Fernandez, Y. A.; Gschneidner, T. A.; Westerlund, F.; Lara-Avila, S.; Moth-Poulsen, K. Single-Molecule Electronics: From Chemical Design to Functional Devices. *Chem. Soc. Rev.* **2014**, *43*, 7378–7411.
- (152) Li, H.; He, F.; Ji, C.; Zhu, W.; Xu, Y.; Zhang, W.; Meng, X.; Fang, X.; Ding, T. Polymer Spacer Tunable Purcell-Enhanced Spontaneous Emission in Perovskite Quantum Dots Coupled to Plasmonic Nanowire Networks. *Phys. Chem. Chem. Phys.* **2019**, *21*, 22831–22838.
- (153) Rasnik, I.; McKinney, S. A.; Ha, T. Nonblinking and Long-Lasting Single-Molecule Fluorescence Imaging. *Nat. Methods* **2006**, *3*, 891–893.
- (154) Kastrup, L.; Hell, S. W. Absolute Optical Cross Section of Individual Fluorescent Molecules. *Angew. Chem - Int. Ed.* **2004**, *43*, 6646–6649.
- (155) Cang, H.; Liu, Y.; Wang, Y.; Yin, X.; Zhang, X. Giant Suppression of Photobleaching for Single Molecule Detection via the Purcell Effect. *Nano Lett.* **2013**, *13*, 5949–5953.
- (156) Wientjes, E.; Renger, J.; Curto, A. G.; Cogdell, R.; Van Hulst, N. F. Strong Antenna-Enhanced Fluorescence of a Single Light-Harvesting Complex Shows Photon Antibunching. *Nat. Commun.* **2014**, *10*, 1038.
- (157) Stefani, F. D.; Vasilev, K.; Bocchio, N.; Pomozi, A.; Kreiter, M. Photonic Mode Density Effects on Single-Molecule Fluorescence Blinking. *New J. Phys.* **2007**, *9*, 21–21.
- (158) Nyokong, T. Effects of Substituents on the Photochemical and Photophysical Properties of Main Group Metal Phthalocyanines. *Coord. Chem. Rev.* **2007**, *251*, 1707–1722.
- (159) Singh, V. P.; Singh, R. S.; Parthasarathy, B.; Aguilera, A.; Anthony, J.; Payne, M. Copper-Phthalocyanine-Based Organic Solar Cells with High Open-Circuit Voltage. *Appl. Phys. Lett.* **2005**, *86*, 082106.
- (160) Sorokin, A.; Seris, J.-L. Meunier, B. Efficient Oxidative Dechlorination and Aromatic Ring Cleavage of Chlorinated Phenols Catalyzed by Iron Sulfophthalocyanine. *Science* **1995**, *268*, 1163-1165.
- (161) Miller, J. D.; Baron, E. D.; Scull, H.; Hsia, A.; Berlin, J. C.; McCormick, T.; Colussi, V.; Kenney, M.E., Cooper, K.D.; Oleinick, N.L. Photodynamic therapy with the phthalocyanine photosensitizer Pc 4: The case experience with preclinical mechanistic and early clinical-translational studies. *Toxicol. Appl. Pharmacol.* **2007**, *224*, 290–299.
- (162) Paulo, P. M. R.; Costa, S. M. B. Single-Molecule Fluorescence of a Phthalocyanine in Pamam Dendrimers Reveals Intensity-Lifetime Fluctuations from Quenching Dynamics. *J. Phys. Chem. C* **2010**, *114*, 19035–19043.

- (163) Kaiser, K.; Gross, L.; Schulz, F. A Single-Molecule Chemical Reaction Studied by High-Resolution Atomic Force Microscopy and Scanning Tunneling Microscopy Induced Light Emission. *ACS Nano* **2019**, *13*, 6947–6954.
- (164) Wang, Y. F.; Kröger, J.; Berndt, R.; Vázquez, H.; Brandbyge, M.; Paulsson, M. Atomic-Scale Control of Electron Transport through Single Molecules. *Phys. Rev. Lett.* **2010**, *104*, 76802.
- (165) Howe, L.; Zhang, J. Z. Ultrafast Studies of Excited-State Dynamics of Phthalocyanine and Zinc Phthalocyanine Tetrasulfonate in Solutions. *J. Phys. Chem. A* **1997**, *101*, 3207–3213.
- (166) Chizhik, A.; Schleifenbaum, F.; Gutbrod, R.; Chizhik, A.; Khoptyar, D.; Meixner, A. J.; Enderlein, J. Tuning the Fluorescence Emission Spectra of a Single Molecule with a Variable Optical Subwavelength Metal Microcavity. *Phys. Rev. Lett.* **2009**, *102*, 073002.
- (167) Masenelli, B.; Gagnaire, A.; Berthelot, L.; Tardy, J.; Joseph, J. Controlled Spontaneous Emission of a Tri(8-Hydroxyquinoline) Aluminum Layer in a Microcavity. *J. Appl. Phys.* **1999**, *85*, 3032–3037.
- (168) Steiner, M.; Schleifenbaum, F.; Stupperich, C.; Failla, A. V.; Hartschuh, A.; Meixner, A. J. Microcavity-Controlled Single-Molecule Fluorescence. *ChemPhysChem* **2005**, *6*, 2190–2196.
- (169) Ly, S.; Petrova, J.; Huser, T.; Fore, S.; Gao, T.; Voss, J.; Laurence, T. A. Stoichiometry of Reconstituted High-Density Lipoproteins in the Hydrated State Determined by Photon Antibunching. *Biophys. J.* **2011**, *101*, 970–975.
- (170) Großmayer, K. S.; Hertel, D. P. Photon Antibunching in Single Molecule Fluorescence Spectroscopy. In *Advanced Photon Counting: Applications, Methods, Instrumentation*, Springer, **2014**.
- (171) Zheng, Q.; Jüette, M. F.; Jockusch, S.; Wasserman, M. R.; Zhou, Z.; Altman, R. B.; Blanchard, S. C. Ultra-Stable Organic Fluorophores for Single-Molecule Research. *Chem. Soc. Rev.* **2014**, *43*, 1044–1056.
- (172) Jüette, M. F.; Terry, D. S.; Wasserman, M. R.; Zhou, Z.; Altman, R. B.; Zheng, Q.; Blanchard, S. C. The Bright Future of Single-Molecule Fluorescence Imaging. *Curr. Opin. Chem. Biol.* **2014**, *20*, 103–111.
- (173) Liu, Q.; Wackenhut, F.; Hauler, O.; Scholz, M.; Zur Oven-Krockhaus, S.; Ritz, R.; Adam, P. M.; Brecht, M.; Meixner, A. J. Hypericin: Single Molecule Spectroscopy of an Active Natural Drug. *J. Phys. Chem. A* **2020**, *124*, 2497–2504.
- (174) Fu, Y.; Zhang, J.; Lakowicz, J. R. Reduced Blinking and Long-Lasting Fluorescence of

- Single Fluorophores Coupling to Silver Nanoparticles. *Langmuir* **2008**, *24*, 3429–3433.
- (175) Martin, Y. C. Let's Not Forget Tautomers. *J. Comput. Aided. Mol. Des.* **2009**, *23*, 693–704.
- (176) Srivastava, R. The Role of Proton Transfer on Mutations. *Front. Chem.* **2019**, *7*, 536.
- (177) Taylor, P. J.; van der Zwan, G.; Antonov, L. Tautomerism: Introduction, History, and Recent Developments in Experimental and Theoretical Methods. In *Tautomerism Methods and Theory*, Wiley-VCH, **2013**.
- (178) Singh, V.; Fedeles, B. I.; Essigmann, J. M. Role of Tautomerism in RNA Biochemistry. *RNA* **2015**, *21*, 1–13.
- (179) Waluk, J. Spectroscopy and Tautomerization Studies of Porphycenes. *Chem. Rev.* **2017**, *117*, 2447–2480.
- (180) Maity, D. K.; Truong, T. N. Status of Theoretical Modeling of Tautomerization in Free-Base Porphyrin. *J. Porphyr. Phthalocyanines* **2001**, *5*, 289–299.
- (181) Strenalyuk, T.; Samdal, S.; Volden, H. V. Molecular Structure of Phthalocyaninatotin(II) Studied by Gas-Phase Electron Diffraction and High-Level Quantum Chemical Calculations. *J. Phys. Chem. A* **2008**, *112*, 10046–10052.
- (182) Antonov, L.; Deneva, V.; Kurteva, V.; Nedeltcheva, D.; Crochet, A.; Fromm, K. M. Controlled Tautomerism - Switching Caused by an “Underground” Anionic Effect. *RSC Adv.* **2013**, *3*, 25410–25416.
- (183) Liljeroth, P.; Repp, J.; Meyer, G. Current-Induced Hydrogen. Current-Induced Hydrogen Tautomerization and Conductance Switching of Naphthalocyanine Molecules. *Science* **2007**, *317*, 1203–1206.
- (184) Abdel-Latif, M. K.; Kühn, O. Laser Control of Double Proton Transfer in Porphycenes: Towards an Ultrafast Switch for Photonic Molecular Wires. *Theor. Chem. Acc.* **2011**, *128*, 307–316.
- (185) Ishizuka, T.; Sakashita, R.; Iwanaga, O.; Morimoto, T.; Mori, S.; Ishida, M.; Toganoh, M.; Takegoshi, K.; Osuka, A.; Furuta, H. NH Tautomerism of N-Confused Porphyrin: Solvent/Substituent Effects and Isomerization Mechanism. *J. Phys. Chem. A* **2020**, *124*, 5756–5769.
- (186) Braun, J.; Limbach, H. H.; Schlabach, M.; Wehrle, B.; Kocher, M.; Vogel, E. NMR Study of the Tautomerism of Porphyrin Including the Kinetic HH/HD/DD Isotope Effects in the Liquid and the Solid State. *J. Am. Chem. Soc.* **1994**, *116*, 6593–6604.
- (187) Frydman, L.; Olivieri, A. C.; Diaz, L. E.; Frydman, B.; Morin, F. G.; Mayne, C. L.; Grant, D. M.; Adler, A. D. High-Resolution Solid-State ¹³C NMR Spectra of Porphine

- and 5,10,15,20-Tetraalkylporphyrins: Implications for the N—H Tautomerization Process. *J. Am. Chem. Soc.* **1988**, *110*, 336–342.
- (188) Maity, D. K.; Bell, R. L.; Truong, T. N. Mechanism and Quantum Mechanical Tunneling Effects on Inner Hydrogen Atom Transfer in Free Base Porphyrin: A Direct Ab Initio Dynamics Study. *J. Am. Chem. Soc.* **2000**, *122*, 897–906.
- (189) Claramunt, R. M.; Lopez, C.; Santa Maria, M. D.; Sanz, D.; Elguero, J. The Use of NMR Spectroscopy to Study Tautomerism. *Prog. Nucl. Mag. Res. Sp.* **2006**, *49*, 169–206.
- (190) Wehrle, B.; Limbach, H.-H.; Köcher, M.; Ermer, O.; Vogel, E. ¹⁵N-CPMAS-NMR Study of the Problem of NH Tautomerism in Crystalline Porphine and Porphycene. *Angew. Chem - Int. Ed.* **1998**, *26*, 9.
- (191) Wehrle, B.; Limbach, H. Heinrich. NMR Study of Environment Modulated Proton Tautomerism in Crystalline and Amorphous Phthalocyanine. *Chem. Phys.* **1989**, *136*, 223–247.
- (192) Gil, M.; Kijak, M.; Piwonski, H.; Herbich, J.; Waluk, J. Non-Typical Fluorescence Studies of Excited and Ground State Proton and Hydrogen Transfer. *Methods Appl. Fluoresc.*, *5*, 014007.
- (193) Fita, P.; Urbańska, N.; Radzewicz, C.; Waluk, J. Ground-and Excited-State Tautomerization Rates in Porphycenes. *Chem. - A Eur. J.* **2009**, *15*, 4851–4856.
- (194) Waluk, J. Non-Classical Effects in Proton or Hydrogen Transfer. *Pure Appl. Chem.* **2016**, *88*, 1063–1071.
- (195) Piwoński, H.; Sokołowski, A.; Kijak, M.; Nonell, S.; Waluk, J. Arresting Tautomerization in a Single Molecule by the Surrounding Polymer: 2,7,12,17-Tetraphenylporphycene. *J. Phys. Chem. Lett.* **2013**, *4*, 3967–3971.
- (196) Piwoński, H.; Stupperich, C.; Hartschuh, A.; Sepioł, J.; Meixner, A.; Waluk, J. Imaging of Tautomerism in a Single Molecule. *J. Am. Chem. Soc.* **2005**, *127*, 5302–5303.
- (197) Gawinkowski, S.; Pszona, M.; Gorski, A.; Niedziółka-Jönsson, J.; Kamińska, I.; Nogala, W.; Waluk, J. Single Molecule Raman Spectra of Porphycene Isotopologues. *Nanoscale* **2016**, *8*, 3337–3349.
- (198) Kumagai, T.; Hanke, F.; Gawinkowski, S.; Sharp, J.; Kotsis, K.; Waluk, J.; Persson, M.; Grill, L. Controlling Intramolecular Hydrogen Transfer in a Porphycene Molecule with Single Atoms or Molecules Located Nearby. *Nat. Chem.* **2014**, *6*, 41–46.
- (199) Böckmann, H.; Liu, S.; Mielke, J.; Gawinkowski, S.; Waluk, J.; Grill, L.; Wolf, M.; Kumagai, T. Direct Observation of Photoinduced Tautomerization in Single Molecules at a Metal Surface. *Nano Lett.* **2016**, *16*, 1034–1041.

- (200) Ladenthin, J. N.; Frederiksen, T.; Persson, M.; Sharp, J. C.; Gawinkowski, S.; Waluk, J.; Kumagai, T. Force-Induced Tautomerization in a Single Molecule. *Nat. Chem.* **2016**, *8*, 935–940.
- (201) Mangel, S.; Skripnik, M.; Polyudov, K.; Dette, C.; Wollandt, T.; Punke, P.; Li, D.; Urcuyo, R.; Pauly, F.; Jung, S. J.; et al. Electric-Field Control of Single-Molecule Tautomerization. *Phys. Chem. Chem. Phys.* **2020**, *22*, 6370–6375.
- (202) Chizhik, A. M.; Jäger, R.; Chizhik, A. I.; Bär, S.; MacK, H. G.; Sackrow, M.; Stanciu, C.; Lyubimtsev, A.; Hanack, M.; Meixner, A. J. Optical Imaging of Excited-State Tautomerization in Single Molecules. *Phys. Chem. Chem. Phys.* **2011**, *13*, 1722–1733.
- (203) Quabis, S.; Dorn, R.; Eberler, M.; Glöckl, O.; Leuchs, G. Focusing Light to a Tighter Spot. *Opt. Commun.* **2000**, *179* (1), 1–7.
- (204) Khoptyar, D.; Gutbrod, R.; Chizhik, A.; Enderlein, J.; Schleifenbaum, F.; Steiner, M.; Meixner, A. J. Tight Focusing of Laser Beams in a $\lambda/2$ -Microcavity. *Opt. Express* **2008**, *16*, 9907.
- (205) Radziszewski, J. G.; Waluk, J.; Michl, J. FT Visible Absorption Spectroscopy of Porphine in Noble Gas Matrices. *J. Mol. Spectrosc.* **1990**, *140*, 373–389.
- (206) Doppagne, B.; Neuman, T.; Soria-Martinez, R.; López, L. E. P.; Bulou, H.; Romeo, M.; Berciaud, S.; Scheurer, F.; Aizpurua, J.; Schull, G. Single-Molecule Tautomerization Tracking through Space- and Time-Resolved Fluorescence Spectroscopy. *Nat. Nanotechnol.* **2020**, *15*, 207–211.